

## ***Master Thesis***

Masterarbeit zur Erlangung des akademischen Grades einer Diplom- Ingenieurin der  
Studienrichtung Chemical and Pharmaceutical Engineering an der Technischen Universität Graz

# **Absorption Effects in Clean Room Decontamination via Hydrogen Peroxide**

Untersuchung der Wasserstoffperoxid Absorption  
in ausgewählten Polymeren

Silvia Marianne Larisegger, BSc

Advisors:

Dipl.-Ing. Dr.techn. Stefan Radl

Institute for Process and Particle Engineering, University of Technology, Graz

Dipl.-Ing. Dr.-Ing. Daniele Suzzi

Research Center Pharmaceutical Engineering GmbH, Graz

Univ.-Prof. Dipl.-Ing. Dr.techn. Johannes G. Khinast

Institute for Process and Particle Engineering, University of Technology, Graz

Graz, January 2011

## ***Statutory Declaration***

I declare that I have authored this thesis independently, that I have not used other than the declared sources / resources, and that I have explicitly marked all material which has been quoted either literally or by content from the used sources.

---

Place, Date

---

Signature

## ***Eidesstattliche Erklärung***

Ich erkläre an Eides statt, dass ich die vorliegende Arbeit selbstständig verfasst, andere als die angegebenen Quellen/Hilfsmittel nicht benutzt, und die den benutzten Quellen wörtlich und inhaltlich entnommene Stellen als solche kenntlich gemacht habe.

---

Ort, Datum

---

Unterschrift

## ***Abstract***

Since a few years, DHP (Decontamination by Hydrogen Peroxide) is the common technology for clean room decontamination in pharmaceutical industry. Here, the absorption and desorption effects of hydrogen peroxide in and from polymers play a decisive role. Especially, it is known from industry that furniture of plastics can absorb a high amount of hydrogen peroxide leading to a long aeration time during the decontamination process. Due to the limited know-how about this process, predictions of absorption and desorption effects of hydrogen peroxide are partially or rather not possible at all.

Hence, the aim of this work was to examine these effects under mathematical considerations and experimental investigations. Furthermore, computational fluid dynamics (CFD) was used to achieve more information about desorption from polymer in a test chamber.

The measurements of still unknown properties of hydrogen peroxide in different polymers (polyvinylchloride (PVC), polypropylene (PP), low-density polyethylene (LDPE)) and in glass were performed using a novel experimental setup. To compare the absorption behaviour of these different polymers the diffusion coefficient and saturation concentration of hydrogen peroxide were determined. The results of the experiments showed that the diffusion coefficient lowered from LDPE to PP to PVC. In contrast, the saturation concentration of hydrogen peroxide increased highly from LDPE to PP to PVC. The absorption and desorption experiment of hydrogen peroxide verified that no absorption of hydrogen peroxide in glass occurred. Moreover, the ability of NIR to quantify adsorbed hydrogen peroxide on polymer surfaces was assessed.

According to our CFD analysis, the flow profile in a test chamber was examined with four different mesh refinements using two different programs, i.e. OpenFoam and AVL Fire. All mesh refinements as well as both CFD programs represented the same flow characteristics in the chamber. Therefore, the coarse mesh with the lowest simulation time, thus lowest computational cost, appeared satisfactory for an industrial application of the method. Moreover, the desorption process of hydrogen peroxide from a polymer was implemented in the open source package OpenFoam. The code was successfully tested for all four grid refinements.\*

---

\* Note that parts of the master thesis were used for the compilation of a paper.

## *Kurzfassung*

In Bezug auf Reinraumtechnik in der pharmazeutischen Industrie ist die Dekontamination mittels Wasserstoffperoxid die Methode der Wahl. In dieser Technologie spielen Absorption und Desorption von Wasserstoffperoxid in Polymeren eine wichtige Rolle. Folglich ist aus der Industrie bekannt, dass Einrichtungsgegenstände aus Kunststoffen in Reinräumen große Mengen an Wasserstoffperoxid aufnehmen können, wodurch sich eine lange Belüftungszeit im Dekontaminationsprozess ergibt. Aufgrund von mangelndem Know-How können diese Absorptions- und Desorptionseffekte von Wasserstoffperoxid schwer bis gar nicht vorhergesagt werden.

Das Ziel dieser Arbeit bestand darin, diese Effekte sowohl mathematisch als auch experimentell zu untersuchen. Weiters wurde die Desorption von einem Polymer in einer Testkammer mittels CFD (Computational Fluid Dynamics) dargestellt.

Um die Eigenschaften von Wasserstoffperoxid in Kunststoffen (Polyvinylchlorid (PVC), Polypropylen (PP), Low-Density Polyethylen (LDPE)) und Glas zu untersuchen, wurde eine eigens entwickelte Versuchsdurchführung verwendet. Um die Absorptionscharakteristika der oben genannten Polymere zu vergleichen, wurden die Diffusionskoeffizienten und die Sättigungskonzentrationen von Wasserstoffperoxid in diesen Materialien bestimmt. Hierbei erreichte Wasserstoffperoxid in LDPE den höchsten Diffusionskoeffizienten, gefolgt von PP und PVC. Die größte Sättigungskonzentration zeigte PVC vor PP und LDPE. In Glas konnte keine Absorption von Wasserstoffperoxid festgestellt werden. Weiters wurden Experimente mit NIR als mögliche Messmethode zur Quantifizierung von adsorbiertem Wasserstoffperoxid an der Oberfläche von Polymeren durchgeführt.

Bezüglich CFD wurde das gesamte Geschwindigkeitsprofil in der Testkammer mit vier verschiedenen Gitterfeinheiten und zwei Programmen, OpenFoam und AVL Fire, bestimmt. Sowohl alle verwendeten Gitterfeinheiten als auch beide CFD-Programme zeigten gleiche Ergebnisse. Für industrielle Belange, kurze Rechenzeit und geringe Kosten, kann bereits das grösste Netz verwendet werden. Weiters wurde ein Code in OpenFoam zur Berechnung der Desorption von Wasserstoffperoxid implementiert. Dieser Code wurde erfolgreich für alle vier Gitterfeinheiten getestet.\*

---

\* Teile der Diplomarbeit wurden für die Zusammenstellung eines Papers verwendet.

## *Acknowledgements*

First of all I want to thank Univ.-Prof. Dipl.-Ing. Dr.techn. Johannes G. Khinast who gave me the opportunity to write this master thesis on the Institute of Process and Particle Engineering.

Especially, I thank Dipl.-Ing. Dr. techn. Stefan Radl for his support often leading to widespread discussions. I have learned a lot and I am sure that he prepared me perfectly for further work. Despite regress of “consciousness”, I can argue that I have reached the third step (I know the problem and can solve it) of the „4 phases of learning“ relating to an increase of my knowledge with his aid.

Furthermore, thanks go to Dipl.-Ing. Dr.-Ing. Daniele Suzzi for his supervision concerning the master thesis, especially the simulation part of my work.

Moreover, I want to thank *Ortner Reinraumtechnik GmbH* as well as the *RCPE GmbH* for the financial support and for providing laboratory infrastructure.

I want to thank Li, Johann Grubbauer (IPPT), Hannes Hofer, Gudrun Hörl and Michael Gruber (all *RCPE GmbH*) for their support during the absorption/desorption measurements, as well as Johann Moor performing the NIR measurements.

Moreover, thanks to my colleagues from the “satellite office” and from the Institute of Process and Particle Engineering. Special thanks go to Sabrina and Heidi for their support in any situations and Piet for his encouragement regarding “Leaching in Pharmaceutical Industry”.

Of course I'd like to thank my brother and my parents who were my support not only for the master thesis but also in many situations of my life. Finally, I want to thank all my friends, especially Martina and Manuel, who play an important role in my life besides my family.

# Table of Contents

<b>1. Introduction</b> .....	<b>1</b>
1.1. Motivation .....	1
1.2. Goals.....	2
1.3. Thesis Outline.....	3
<b>2. Background</b> .....	<b>4</b>
2.1. The Relevance of Leaching in the Pharmaceutical Industry .....	4
2.2. Hydrogen Peroxide Decontamination Technology .....	7
<b>3. Mathematical Models</b> .....	<b>11</b>
3.1. Basic Thermodynamic Models for Binary Mixtures .....	11
3.2. Absorption and Desorption in Solids .....	13
3.2.1. Implementation of an Absorption Model for the System H <sub>2</sub> O <sub>2</sub> in Polymers .....	13
3.2.2. Calculation of the Diffusion Coefficient and Saturation Concentration in Polymers .....	25
3.3. Mass Transfer from the Polymer into the Fluid Phase .....	26
3.3.1. Short Contact Times .....	31
3.3.2. Long Contact Times .....	31
3.3.3. Concentration Profile in the Polymer .....	32
3.4. Numerical Model.....	33
3.4.1. Continuity Equation.....	33
3.4.2. Momentum Conservation Equation .....	33
3.4.3. Species Transport Equation .....	36
<b>4. Simulation Setup</b> .....	<b>37</b>
4.1. Test Chamber .....	37
4.2. Simulation Settings .....	38
<b>5. Experimental Method</b> .....	<b>41</b>
5.1. Absorption and Desorption in Polymers.....	41
5.1.1. Experimental Setup.....	41
5.1.2. Absorption Procedure .....	42
5.1.3. Measurement Procedure for the 30 % (w/w) H <sub>2</sub> O <sub>2</sub> Solution .....	43
5.1.4. Desorption Procedure .....	44
5.1.5. Amplex® Red Hydrogen/ Peroxidase Assay Kit.....	44
5.1.6. Materials and Experimental Conditions .....	46
5.2. Fast Detection of H <sub>2</sub> O <sub>2</sub> in Polymers using NIR .....	47
<b>6. Results</b> .....	<b>49</b>
6.1. Experiments.....	49
6.1.1. Differences between Stripes and Flakes .....	49
6.1.2. Polypropylen (PP).....	50
6.1.3. Low-Density Polyethylene (LDPE), Polyvinylchloride (PVC) and Glass .....	52
6.1.4. Detection of H <sub>2</sub> O <sub>2</sub> in Polymers using NIR .....	54
6.2. Simulations .....	56
6.2.1. Flow Profile in the Test Chamber.....	56

6.2.2.	Mass Transport in Test Chamber.....	62
6.2.3.	Grid Convergence Study .....	69
<b>7.</b>	<b><i>Discussion</i></b> .....	<b>72</b>
<b>8.</b>	<b><i>References</i></b> .....	<b>76</b>
<b>9.</b>	<b><i>Appendix</i></b> .....	<b>79</b>
<b>9.1.</b>	<b>Calculation of the Activity Coefficients of H<sub>2</sub>O<sub>2</sub> and H<sub>2</sub>O for a 30 and 70 % (w/w) Aqueous H<sub>2</sub>O<sub>2</sub> Solution at 298.15 K .....</b>	<b>79</b>
<b>9.2.</b>	<b>Calibration Curve for 30 % (w/w) Aqueous H<sub>2</sub>O<sub>2</sub> Solutions .....</b>	<b>81</b>
<b>9.3.</b>	<b>Prediction Model fitting Experimental Data .....</b>	<b>82</b>
9.3.1.	Stripes .....	82
9.3.2.	Flakes.....	86
<b>9.4.</b>	<b>Experimental Results.....</b>	<b>88</b>
9.4.1.	Low-Density Polyethylene (LDPE).....	88
9.4.2.	Polyvinylchloride (PVC) .....	89
9.4.3.	Glass (Microscope Slides) .....	90
<b>9.5.</b>	<b>Code for “adAbFoam” Solver .....</b>	<b>92</b>
9.5.1.	adAbFoam .....	92
9.5.2.	createFields.....	94
9.5.3.	FluxWriter .....	96
9.5.4.	startFluxLogger .....	99
9.5.5.	YEqn.....	99

# List of Figures

Figure 2-1 - Clarus® C (Bioquell) [17] and VHP® 1000ED (STERIS) [18].	7
Figure 2-2 - Phases of a decontamination cycle [4].	8
Figure 3-1 - Schematic sketch of the diffusion in a volume element [24].	13
Figure 3-2 - Diffusion concentration profile of H <sub>2</sub> O <sub>2</sub> in PET, D= 3.23E-12 cm <sup>2</sup> s <sup>-1</sup> at 298.15 K (left); Diffusion concentration profile of H <sub>2</sub> O <sub>2</sub> in LDPE, D= 1.57E-07 cm <sup>2</sup> s <sup>-1</sup> at 298.15 K (right).	17
Figure 3-3 - Schematic sketch of the concentration profile in a infinite and semi-infinite plane polymer sheet.	18
Figure 3-4 - Concentration distributions at various Fourier numbers in a plane polymer sheet (left); Concentration distributions at various Fourier numbers in a polymer sphere (right).	20
Figure 3-5 - Average normalized concentrations against Fourier numbers for a plane sheet and a sphere.	21
Figure 3-6 - Concentration of H <sub>2</sub> O <sub>2</sub> for a 30 % (w/w) aqueous H <sub>2</sub> O <sub>2</sub> solution in a semi-infinite and infinite LDPE; D= 1.57E-07 cm <sup>2</sup> s <sup>-1</sup> , C <sub>1</sub> =2.51E-04 kmol m <sup>-3</sup> .	23
Figure 3-7 - Concentration of H <sub>2</sub> O <sub>2</sub> for a 30 % (w/w) aqueous H <sub>2</sub> O <sub>2</sub> solution in a semi-infinite and infinite PP (homo and random); D= 3.91E-09 cm <sup>2</sup> s <sup>-1</sup> , C <sub>1</sub> = 2.92E-04 kmol m <sup>-3</sup> .	24
Figure 3-8 - Schematic sketch of the concentration profiles occurring during the desorption process from a polymer.	26
Figure 3-9 - Velocity boundary layer and concentration boundary layer [30].	28
Figure 4-1 - Different grid refinements of the test chamber.	37
Figure 4-2 - Sketch of the test chamber.	38
Figure 4-3 - All Simulations using OpenFoam.	39
Figure 4-4 - All Simulations using AVL Fire.	40
Figure 5-1 - Sketch of the experimental setup 1 for absorption and desorption experiments involving polymer flakes.	41
Figure 5-2 - Experimental setup 2 for absorption and desorption experiments involving polymer stripes.	42
Figure 5-3 - Weight percentage of the H <sub>2</sub> O <sub>2</sub> solution during the absorption procedure (H <sub>2</sub> O <sub>2</sub> and polypropylene at 303.15 K).	44
Figure 5-4 - Oxidation of Amplex® Red reagent to resorufin [37].	45
Figure 5-5 - Absorption and concentration of H <sub>2</sub> O <sub>2</sub> for different dilutions of the last sample (LDPE, second run).	46
Figure 6-1 - Arithmetic mean of amount of H <sub>2</sub> O <sub>2</sub> and standard deviation for all dilutions (1:4, 1:8, 1:16; experiments involving PP stripes and flakes).	49
Figure 6-2 - Desorbed amount of H <sub>2</sub> O <sub>2</sub> from polypropylene at 298.15 K, 303.15 K and 308.15 K.	51
Figure 6-3 - Desorbed amount of H <sub>2</sub> O <sub>2</sub> from low-density polyethylene at 308.15 K (second run).	53
Figure 6-4 - Desorbed amount of H <sub>2</sub> O <sub>2</sub> from polyvinylchloride at 308.15 K (second run).	53
Figure 6-5 - Score plot of an untreated (blue 0.000) and a saturated PVC foil (red 30.00), directly after saturation.	55
Figure 6-6 - Score plot of two saturated PVC foils (blue 1.000 and red 2.000, cleaned) and an untreated PVC foil (green 3.000).	55
Figure 6-7 - Vector fields of U [m/s] in the test chamber (normal mesh) using AVL Fire.	56
Figure 6-8 - Vector fields of U [m/s] in the test chamber (normal mesh) using OpenFoam.	57
Figure 6-9 - Velocity data sampled along the Inlet line of different mesh sizes using OpenFoam (RANS).	58
Figure 6-10 - Velocity data sampled along the Inlet line of different mesh sizes using AVL Fire (RANS).	58
Figure 6-11 - Velocity data sampled along the Outlet line of different mesh sizes using OpenFoam (RANS).	59
Figure 6-12 - Velocity data sampled along the Outlet line of different mesh sizes using AVL Fire (RANS).	60
Figure 6-13 - Velocity and kinetic energy distributions with different turbulence intensities (cut through Inlet using OpenFoam, RANS).	61
Figure 6-14 - U <sub>z</sub> of different turbulence intensities (I) sampled along the Inlet and the Outlet line using OpenFoam (RANS).	62
Figure 6-15 - Mean concentration of H <sub>2</sub> O <sub>2</sub> with frozen velocity field using OpenFoam (normal mesh).	63
Figure 6-16 - Concentration profile at the Outlet with LES using OpenFoam (coarse mesh).	64
Figure 6-17 - Species Transport (Y [kmol m <sup>-3</sup> /kmol m <sup>-3</sup> ]) in the test chamber (normal mesh, LES, OpenFoam, half side of test chamber with Outlet).	66
Figure 6-18 - Mass fraction of H <sub>2</sub> O [-/-] sampled along the Inlet line of different mesh sizes at 30 s (AVL Fire).	67
Figure 6-19 - Distribution of the mass fraction of H <sub>2</sub> O at different time steps (cut through the Inlet, normal mesh, AVL Fire).	68

<i>Figure 6-20 - Results for grid convergence study of finefine, fine and normal meshes (left) as well as fine, normal and coarse meshes (right).</i>	71
<i>Figure 7-1 - Comparison of the diffusion coefficient of H<sub>2</sub>O<sub>2</sub> in different materials at 308.15 K.</i>	73
<i>Figure 7-2 - Comparison of the saturation concentration of H<sub>2</sub>O<sub>2</sub> in different materials at 308.15 K.</i>	73
<i>Figure 9-1 - Calibration curve for 30 % (w/w) aqueous H<sub>2</sub>O<sub>2</sub> solution (absorption at 340 nm).</i>	81
<i>Figure 9-2 - Fit of the desorbed amount of H<sub>2</sub>O<sub>2</sub> from PP stripes in H<sub>2</sub>O with EDTA [50 mg/L] (1:4 dilution, 298.15 K, second run).</i>	82
<i>Figure 9-3 - Fit of the desorbed amount of H<sub>2</sub>O<sub>2</sub> from PP stripes in H<sub>2</sub>O with EDTA [50 mg/L] (1:8 dilution, 298.15 K, second run).</i>	82
<i>Figure 9-4 - Fit of the desorbed amount of H<sub>2</sub>O<sub>2</sub> from PP stripes in H<sub>2</sub>O with EDTA [50 mg/L] (1:16 dilution, 298.15 K, second run).</i>	83
<i>Figure 9-5 - Fit of the desorbed amount of H<sub>2</sub>O<sub>2</sub> from PP stripes in H<sub>2</sub>O with EDTA [50 mg/L] (1:10 dilution, 303.15 K, third run).</i>	83
<i>Figure 9-6 - Fit of the desorbed amount of H<sub>2</sub>O<sub>2</sub> from PP stripes in H<sub>2</sub>O with EDTA [50 mg/L] (1:20 dilution, 308.15 K, fourth run).</i>	84
<i>Figure 9-7 - Fit of the desorbed amount of H<sub>2</sub>O<sub>2</sub> from LDPE stripes in H<sub>2</sub>O with EDTA [50 mg/L] (1:100 dilution, 308.15 K, first run).</i>	84
<i>Figure 9-8 - Fit of the desorbed amount of H<sub>2</sub>O<sub>2</sub> from LDPE stripes in H<sub>2</sub>O with EDTA [50 mg/L] (1:20 dilution, 308.15 K, second run).</i>	85
<i>Figure 9-9 - Fit of the desorbed amount of H<sub>2</sub>O<sub>2</sub> from PVC stripes in H<sub>2</sub>O with EDTA [50 mg/L] (1:600 dilution, 308.15 K, first run).</i>	85
<i>Figure 9-10 - Fit of the desorbed amount of H<sub>2</sub>O<sub>2</sub> from PVC stripes in H<sub>2</sub>O with EDTA [50 mg/L] (1:50 dilution, 308.15 K, second run).</i>	86
<i>Figure 9-11 - Fit of the desorbed amount of H<sub>2</sub>O<sub>2</sub> from PP flakes in H<sub>2</sub>O with EDTA [50 mg/L] (1:4 dilution, 303.15 K, first run).</i>	86
<i>Figure 9-12 - Fit of the desorbed amount of H<sub>2</sub>O<sub>2</sub> from PP flakes in H<sub>2</sub>O with EDTA [50 mg/L] (1:8 dilution, 303.15 K, first run).</i>	87
<i>Figure 9-13 - Fit of the desorbed amount of H<sub>2</sub>O<sub>2</sub> from PP flakes in H<sub>2</sub>O with EDTA [50 mg/L] (1:16 dilution, 303.15 K, first run).</i>	87
<i>Figure 9-14 - Desorbed amount of H<sub>2</sub>O<sub>2</sub> from low-density polyethylene at 308.15 K.</i>	89
<i>Figure 9-15 - Desorbed amount of H<sub>2</sub>O<sub>2</sub> from polyvinylchloride at 308.15 K.</i>	90
<i>Figure 9-16 - Desorbed amount of H<sub>2</sub>O<sub>2</sub> from glass at 308.15 K (the first measured H<sub>2</sub>O<sub>2</sub> concentration was not subtracted, leading to a set off of the concentration curve due to small amounts of adsorbed H<sub>2</sub>O<sub>2</sub>).</i>	91

## List of Tables

Table 2-1 - Hydrogen peroxide compatible materials [16].....	10
Table 3-1 - Fugacity of $H_2O_2$ on the gas phase and liquid phase.....	13
Table 3-2 - Calculation of diffusion coefficients of $H_2O_2$ in different polymers; $M_i= 34.02$ g/mol, $T = 298.15$ K.....	15
Table 3-3 - Comparison of diffusion coefficients of $CH_4$ and $H_2O_2$ in PE and PET at different temperatures.....	16
Table 3-4 - Concentration of $H_2O$ [ $kmol\ m^{-3}$ ] in different polymers at equilibrium state [1]. .....	22
Table 3-5 - Saturation concentrations of $H_2O$ and $H_2O_2$ for a 30 % (w/w) and 70 % (w/w) aqueous $H_2O_2$ solution in different polymers at 298.15K.....	22
Table 3-6 - Partition coefficient [ $kmol\ m^{-3}$ ]/[ $kmol\ m^{-3}$ ] of different $H_2O$ /polymer systems.....	22
Table 3-7 - Results for the mass transfer coefficient of three different velocities ( $L= 0.2$ m, $Sc= 0.79$ , $D_{i,liq}= 1.92E-05\ m^2\ s^{-1}$ ).....	29
Table 3-8 - Constants for the turbulence model.....	35
Table 4-1 - Bonds for the four different patches.....	38
Table 4-2 - $k$ and $\epsilon$ for different turbulent intensities.....	40
Table 5-1 - Experimental conditions for absorption and desorption experiments involving different polymers.....	47
Table 6-1 - Results for the diffusion coefficient and saturation concentration of $H_2O_2$ from PP stripes and flakes in dist. $H_2O_2$ with EDTA [50 mg/L] at 303.15 K.....	50
Table 6-2 - Results for the diffusion coefficient and saturation concentration of $H_2O_2$ in PP at different temperatures.....	52
Table 6-3 - Results for the diffusion coefficient and the saturation concentration of $H_2O_2$ in LDPE, PVC and glass at 308.15 K.....	52
Table 6-4 - Results for species transport of all simulation cases using OpenFoam (code: adAbFoam).....	65
Table 6-5 - Parameter for the grid convergence study of finefine, fine and normal mesh.....	70
Table 6-6 - Parameter for the grid convergence study of fine, normal and coarse mesh.....	71
Table 9-1 - Constants for the calculation of the Redlich-Kister Parameters at 298.15 K.....	79
Table 9-2 - Redlich-Kister Parameters at 298.15 K.....	79
Table 9-3 - Activity coefficient of $H_2O$ and $H_2O_2$ for a 30 % (w/w) aqueous $H_2O_2$ solution at 298.15 K.....	80
Table 9-4 - Activity coefficient of $H_2O$ and $H_2O_2$ for a 70 % (w/w) aqueous $H_2O_2$ solution at 298.15 K.....	80
Table 9-5- Results for the diffusion coefficient of $H_2O_2$ in LDPE at 308.15 K.....	88
Table 9-6 - Results for the saturation concentration of $H_2O_2$ in LDPE at 308.15 K.....	88
Table 9-7 - Results for the diffusion coefficient of $H_2O_2$ in PVC at 308.15 K.....	90
Table 9-8 - Results for the saturation concentration of $H_2O_2$ in PVC at 308.15 K.....	90

## Abbreviations

AAMI	Association for the Advancement of Medical Instrumentation
Al	Aluminium
API	Active pharmaceutical ingredient
As	Arsenic
CFD	Computational Fluid Dynamics
Cr	Chrome
DEHP	Bis(2-ethylhexyl)phthalate
DHP	Decontamination by Hydrogen Peroxide
DMSO	Dimethyl sulfoxide
DNS	Discrete Numerical Simulation
EDTA	Ethylenediaminetetraacetic acid
EMEA	European Medicines Agency
EPDM	Ethylene-propylene-diene rubber
FDA	Food and Drug Administration
FFKM	Kalrez <sup>®</sup> Perfluoroelastomer
FKM	Fluoroelastomer
Ga	Gallium
GC-FLORY	Group-contribution Flory
GCI	Grid convergence index
H <sub>2</sub> O	Water
H <sub>2</sub> O <sub>2</sub>	Hydrogen peroxide
HDPE	High-density polyethylene
HIPS	High impact polystyrene
HPL	High pressure laminate
HRP	Horseradish peroxidase
In	Indium
IR	Infrared
LDPE	Low-density polyethylene
LES	Large Eddy Simulation
MD	Molecular Dynamics

MVDA	Multivariate Data Analysis
NASA	National Aeronautics and Space Administration
Ni	Nickel
NIR	Near-infrared
OSHA	The Occupational Safety and Health Administration
PA (6,6)	Polyamide
PC	Polycarbonate
PC	Principle Component
PCA	Principle Component Analysis
PE	Polyethylene
PEN	Polyethylene naphthalate
PET	Polyethylene terephthalate
PFA	Perfluoroalkoxy
POM	Polyoxymethylene
PP	Polypropylene
PS	Polystyrene
PTFE	Polytetrafluoroethylene
pt-Si	Platinum-cured silicon
PVC	Polyvinylchloride
PVDF	Polyvinylidene fluoride
QSAR	Quantitative structure-activity relationship
RANS	Reynolds-Averaged Navier-Stokes
Ti	Titan
TIC	Temperature Indicator Controller
UNIFAC	Universal Quasichemical Functional Group Activity Coefficients
UV	Ultraviolet
VHP <sup>®</sup>	Vaporized Hydrogen Peroxide
VIS	Visible

## Latin Letters

$a$	Radius of a polymer sphere [m]
$A$	Area [ $m^2$ ]
$A_p$	Upper-bond conductance [-]
$A_{\text{polymer}}$	Area of the polymer [ $m^2$ ]
$B_n$	Redlich-Kister parameter [ $\text{cal mol}^{-1}$ ]
$c$	Dimensionless concentration [-]
$c_i$	Concentration of species in the air [ $\text{kmol m}^{-3}$ ]
$c_{\text{H}_2\text{O}_2, \text{I}}$	Concentration of hydrogen peroxide at the interface [ $\text{kmol m}^{-3}$ ]
$c_{\text{H}_2\text{O}_2, \text{PatchMean}}$	Mean concentration of hydrogen peroxide over the outlet [-]
$c_{\text{H}_2\text{O}_2, \text{ref}}$	Reference concentration of hydrogen peroxide [ $\text{kmol m}^{-3}$ ]
$c_{\text{H}_2\text{O}_2, \infty}$	Concentration of hydrogen peroxide at great distance [ $\text{kmol m}^{-3}$ ]
$C$	Concentration of species in the polymer at $x$ and $t$ [ $\text{kmol m}^{-3}$ ]
$C_{i, \text{liq}}$	Concentration of a solute in the liquid phase [ $\text{kmol m}^{-3}$ ]
$C_{i, \text{s}}$	Concentration of a solute in the solid phase [ $\text{kmol m}^{-3}$ ]
$C_n$	Constants for the turbulence model [-]
$C_s$	Constant surface concentration of species on the polymer at $x=0$ [ $\text{kmol m}^{-3}$ ]
$C_x$	Concentration of species in polymer at location $x$ [ $\text{kmol m}^{-3}$ ]
$C_{\text{H}_2\text{O}_2}^{\text{sat}}$	Saturation concentration of hydrogen peroxide in the polymer [ $\text{kmol m}^{-3}$ ]
$C_{\text{H}_2\text{O} / \text{Polymer}}^{\text{sat}}$	Saturation concentration of water in the polymer [ $\text{kmol m}^{-3}$ ]
$C_i^{\text{sat}}$	Saturation concentration of species in the polymer [ $\text{kmol m}^{-3}$ ]
$\bar{C}$	Average normalized concentration [ $\text{kmol m}^{-3}$ ]
$\bar{C}_{\text{H}_2\text{O}_2}$	Average normalized concentration of hydrogen peroxide in the polymer [ $\text{kmol m}^{-3}$ ]
$C_0$	Concentration of species in the polymer at $t=0$ [ $\text{kmol m}^{-3}$ ]
$C_1$	Saturation concentration of species in the polymer [ $\text{kmol m}^{-3}$ ]
$C_0, C_1, C_2, C_3$	Constants for the Redlich-Kister Parameters [-]
$D$	Diffusion coefficient [ $m^2 s^{-1}$ ]

D	Turbulent diffusion coefficient [-]
$D_{i,\text{liquid}}$	Diffusion coefficient of a species in a liquid phase [ $\text{m}^2 \text{s}^{-1}$ ]
$D_{i,\text{polymer}}$	Diffusion coefficient of a species in a polymer phase [ $\text{m}^2 \text{s}^{-1}$ ]
$D_{i,\text{solid}}$	Diffusion coefficient of a species in a solid phase [ $\text{m}^2 \text{s}^{-1}$ ]
$D_p^*$	Upper diffusion coefficient [ $\text{m}^2 \text{s}^{-1}$ ]
$f_{h=0}$	Richardson extrapolation [-]
$f_i$	Fugacity of species i [Pa]
$f_i$	Scalar solution of the refinement level i [-]
$F_s$	Factor of safety [-]
Fo	Fourier number [-]
g	Gravitational acceleration [ $\text{m s}^{-2}$ ]
h	Grid length [-]
I	Turbulent intensity [%]
J	Diffusion flux [ $\text{kmol m}^{-2} \text{s}^{-1}$ ]
k	Turbulent kinetic energy [ $\text{k}^2 \text{m}^{-2}$ ]
K	Partition coefficient [-]
$K_i$	Partition coefficient of water in the polymer [-]
l	Characteristic length [m]
$l_c$	Characteristic length of the polymer [m]
L	Length scale [m]
$M_{G,12}$	Molecular weight of $\text{H}_2\text{O}_2$ and air [ $\text{kg kmol}^{-1}$ ]
$M_i$	Relative molecular weight of species [-]
$n_i$	Amount of substance i [kmol]
$N_{\text{Chamber}}$	Amount of $\text{H}_2\text{O}_2$ in the chamber [kmol]
$N_{\text{in}}$	Input of the migrant per time [ $\text{kmol s}^{-1}$ ]
$N_{\text{out}}$	Output of the migrant per time [ $\text{kmol s}^{-1}$ ]
$\dot{N}$	Mass flow rate [ $\text{mol s}^{-1}$ ]
$\dot{N}_{\text{out}}$	Mass flow of $\text{H}_2\text{O}_2$ from the outlet [ $\text{kmol s}^{-1}$ ]
p	Pressure [Pa]
p	Order of accuracy [-]
$p_i$	Vapor pressure for species i in a liquid mixture [Pa]

$p_i^s$	Vapor pressure of pure species $i$ [Pa]
$r$	Spatial coordinate of a sphere [m]
$r$	Grid refinement ratio [-]
$r_{p,i}$	Mass transfer resistance of species $i$ in phase $p$ [ $s\ m^{-1}$ ]
$R$	Gas constant [ $J\ kmol^{-1}\ K^{-1}$ ]
$Re$	Reynolds number [-]
$Sc$	Schmidt number [-]
$Sc_t$	Turbulent Schmidt number [-]
$Sh$	Sherwood number in liquid phase [-]
$Sh_{polymer}$	Sherwood number in polymer phase [-]
$t$	Time [s]
$T$	Temperature [K]
$u_\infty$	Flow rate [ $m\ s^{-1}$ ]
$v$	Atomic diffusion volume [-]
$\mathbf{v}$	Velocity vector [ $m\ s^{-1}$ ]
$V_{Liquid}$	Liquid volume [L]
$V_{Polymer}$	Polymer volume [ $m^3$ ]
$\dot{V}_{out}$	Volume flow of the outlet [ $m^3\ s^{-1}$ ]
$x$	Spatial coordinate (normal to the surface of a thin sheet) [m]
$x_i$	Molar fraction of species $i$ in the liquid phase [-]
$y_i$	Molar fraction of species $i$ in the gas phase [-]

## Greek Letters

$\beta$	Mass transfer coefficient in the liquid phase [ $m\ s^{-1}$ ]
$\beta_g$	Mass transfer coefficient in the gas phase [ $m\ s^{-1}$ ]
$\beta_{polymer}$	Mass transfer coefficient in the polymer [ $m\ s^{-1}$ ]
$\gamma_i$	Activity coefficient [-]
$\delta$	Unit tensor [-]
$\varepsilon$	Dissipation energy [ $m^2\ s^{-3}$ ]
$\eta$	Dimensionless coordinate [-]

$\Theta$	Dimensionless concentration [-]
$\mu_t$	Turbulence viscosity [Pa·s]
$\nu_{liq}$	Kinematic viscosity [ $m^2 s^{-1}$ ]
$\nu_t$	Turbulent viscosity [ $m^2 s^{-1}$ ]
$\rho$	Density [ $kg m^{-3}$ ]
$\sigma$	Standard deviation [-]
$\sigma_n$	Constants for the turbulence model [-]
$\tau$	Stress tensor [ $N m^{-2}$ ]
$\Phi$	Volumetric flow rate [ $m^3 s^{-1}$ ]
$\phi_i$	Fugacity coefficient [-]

## 1. Introduction

### **1.1. Motivation**

In the manufacturing process for pharmaceutical industry decontamination plays an important role. Especially during the production of parenteral solutions, e.g. injections and infusions, the highest requirements for sterility have to be ensured. In order to guarantee these conditions, the production zones in relevant laboratories, filling lines, clean rooms and isolators, etc. have to be sterilized. Besides ethylene oxide, formaldehyde and peracetic acid, hydrogen peroxide is one of the most common agents for gaseous decontamination processes [1]. Because of the effectiveness against spores, bacteria and viruses, as well as the nontoxic end products (i.e., water and oxygen) after catalytic breakdown, hydrogen peroxide offers many advantages compared to the other sterilants [2, 3].

For DHP (Decontamination by Hydrogen Peroxide) hydrogen peroxide generators from STERIS and BIOQUELL are commercially available. The decontamination process of hydrogen peroxide is similar for both generators. After a preconditioning phase, an aqueous hydrogen peroxide solution (approximately 30 % (w/w)) is evaporated until reaching the desired amount of hydrogen peroxide in the gas phase. In the subsequent decontamination phase a stable concentration of hydrogen peroxide in the chamber is established for a predefined period of time. During this period, condensation may or may not take place, depending on the type of generator used. Finally, the room is purged with air until reaching the OSHA safety level of nowadays 0.5 ppm (this phase is typically called aeration) [4, 5].

Every phase in the decontamination cycle has to be adapted individually to the room conditions. It is well known that different materials of the equipment in a pharmaceutical room, e.g. filters, floors, PVC-tubing, etc. absorb a certain amount of hydrogen peroxide. During aeration this absorbed amount of hydrogen peroxide is desorbed, leading to considerable aeration times up to several hours or even days. This delay can cause bottlenecks in the production, e.g., for aseptically filled products in isolators. In the worst

case entire rooms have to be decommissioned because of aeration for several days. Also, condensation can cause negative effects on surfaces (e.g., blistering of coatings), or may lead to a local depletion of hydrogen peroxide in the gas phase. In addition, evaporation of the condensate may lead to unwanted peaks in hydrogen peroxide levels during aeration, or increase aeration time as well [5, 6].

In order to test the compatibility of various materials with hydrogen peroxide, research has been done by the pharmaceutical industry, as well as by the National Aeronautics and Space Administration (NASA) [6, 7]. In both cases, materials of interest (e.g. floors, coatings for walls, metal samples, plastics, lubricants and adhesives) were exposed to gaseous or liquid hydrogen peroxide. This can be done by soaking the material directly into an aqueous hydrogen peroxide solution, or by treating the material in a test chamber for several times with hydrogen peroxide vapor. To quantify the materials' compatibility, the change of its appearance, tensile and hardness tests are typically used. The compatibility can also be classified using four different grades (i.e., changeless, moderate changeless, marginal applicable, inapplicable) related to the apparent resistance of the materials to hydrogen peroxide. For example, the investigations by *Claassen* [6] showed that certain materials (e.g., natural rubber, HPL-plates, coated sheet metal, etc.) started to blister in contact with hydrogen peroxide. Most of the polymers (e.g., PVC, Vinyl, POM, PTFE, silicon) and stainless steel indicated a sufficient resistance to hydrogen peroxide.

To the best of our knowledge, no quantitative information about absorption effects of hydrogen peroxide in different materials can be found in literature. Reasons for this are (i) the unavailable knowledge of the physical properties that dictate the absorption of hydrogen peroxide in different materials (i.e., diffusion coefficients and saturation concentrations), as well as (ii) the lack of quantitative experimental studies addressing hydrogen peroxide absorption (or desorption).

### **1.2. Goals**

The aim of this study is to systematically analyze the absorption effects of hydrogen peroxide in clean room materials. For this purpose, experimental analysis as well as Computational Fluid Dynamics (CFD) had been used.

To study absorption effects, an experimental setup has been developed during this work with the intention of quantifying small amounts of desorbed hydrogen peroxide from different materials. Specifically, the goal was to measure the saturation concentration and the diffusion coefficient of hydrogen peroxide in several polymers, i.e. polypropylene (PP), low-density polyethylene (LDPE), polyvinylchloride (PVC), and in glass.

The fluid flow and the species transport of hydrogen peroxide in a test chamber have been analyzed by means of numerical simulation as well. Here, the open source package “OpenFOAM” and the commercially available program “AVL Fire” were used and tested using four different mesh refinements. The results obtained from both programs were compared to each other. Furthermore, a grid convergence study was carried out to determine the discretization error related to the numerical method.

### **1.3. Thesis Outline**

The thesis gives a short introduction (see Chapter 2) about leaching in pharmaceutical industry and hydrogen peroxide decontamination technology first. Chapter 3 deals with mathematical models for the description of basic thermodynamics, absorption/desorption, mass transfer and flow mechanics. These background theories lead to important information concerning further experimental work, as well as the simulation part. The precise settings for the simulation are mentioned in Chapter 4. The experimental method, i.e. absorption/desorption procedure, materials and experimental conditions are presented in Chapter 5. The results of the performed experiments, i.e. diffusion coefficients and saturation concentration of the polymers and glass, and the simulation, i.e. flow profile, mass transport and grid convergence study, are discussed in Chapter 6. An extensive discussion of the investigations follows in Chapter 7.

## 2. Background

### **2.1. *The Relevance of Leaching in the Pharmaceutical Industry***

It is hard to imagine life without plastic materials. Especially, in the pharmaceutical industry plastic materials like PP, PFA, PTFE, PVDF, EPDM, FKM, FFKM or pt-Si [8] are the choice for packaging systems, transfer tubing, manufacturing systems, aids, devices and containers [9]. These materials consist of base and compounding materials like antioxidants, accelerators, curing agents, activators, fillers, plasticizers and pigments. These organic or non-organic chemical compounds can be leached into the dosage form [10]. As a consequence, it is important that the interactions between the plastic material and the pharmaceutical product are well known, so that no change occurs in the quality of packaging component or dosage form. For example, changes in pH, stability, color and clarity, as well as formation of particles may finally alter the effectiveness of the product [9, 11].

*Treleano et al.* [12] did not only deal with leaching of polymer additives, but also with the sorption of ingredients of the drug formulation into plastic bags and tubes composed of different polymers and plasticizers. Only 60 % of the initial API concentration appeared to be delivered through a PVC tube with DEHP as plasticizers to a patient in the first few minutes. This result showed that particular attention must be paid to the leaching behaviour of polymer additives, as well as the sorption, which leads to reduced drug delivery to the patient.

*Smith* [10] defined four types of closure-drug interactions: "**Adsorption** occurs when a drug is concentrated at the surface of a closure or a vial. **Absorption** occurs when a drug material is dispersed in the closure matrix. **Permeation** is the transmission of a drug ingredient through a closure into the atmosphere or transmission of an outside material into the container. **Leaching** is the process by which closure ingredients are extracted into the drug product."

A variety of definitions for extractables and leachables are present in literature as well. A definition given by *Jenke* [9] reads as follows:

**“Extractables:** *Substances that can be extracted from plastic materials/systems using extraction solvents and/or extraction conditions that are expected to be more aggressive than the conditions of contact between the material/system and a finishing drug product.*

**Leachables:** *Substances that are present in the finishing drug product because of its interaction with a plastic material or system during its intended use.”*

Another definition is given by *Ball et al.* [13]:

**“Extractables,** *as defined by the U.S. Food and Drug Administration (FDA), are compounds that can be extracted from elastomeric components, plastic components, or coatings of the container and closure system when in the presence of an appropriate solvent.*

**Leachables** *are compounds that leach from elastomeric or plastic components or coatings of the container and closure system as a result of direct contact with the drug product formulation. Extractables are therefore potential leachables, and patients could be exposed to leachables.”*

A lot of proteins tend to adsorb onto polymer/elastomer surfaces. Solvents, acids and bases affect the polymer/elastomer surfaces leading to extraction of plastic compound materials. Common leachables from plastics are metal ions, antioxidants, plasticizers, lubricants, curing agents and accelerators [10].

Therefore, different authorities, i.e. EMEA, FDA, AAMI, claim compatibility assessments leading to extractables/leachables and migration studies. Here, the priority is given on safety and toxicology. The methodologies for extractables/leachables studies differentiate across the world and are not clarified in detail in the regulations. In general, these studies are separated into two steps. First, an extraction study of the plastic material using a simulating solvent and/or drug product is performed. This leads to the identification and the quantification of potential extractables and leachables by analytical measurements (calorimetry, atomic absorption, pH change, turbidity measurements, chromatography [10]). The second step comprises a detailed toxicological risk assessment of these chemical compounds [9].

These chemical analyses are time consuming, therefore lead to high costs during the course of drug development studies (stability studies). Because of this, the product/device interaction has been modelled over the last 15 years, with techniques based on the linear correlation of polymer/solution interaction constants with solvent/water partition coefficients [11].

Furthermore, the mass transport of chemical compounds in polymers/elastomers depends on two main parameters, namely the partition coefficient and the diffusion coefficient [14].

The work of *Trealano et al.* [12] showed that different plasticizers used in PVC tubes modify the diffusion coefficient and the saturation concentration. Furthermore, swelling of the polymer matrix due to the compounds of the drug formulation led to an increased sorption of active ingredient into the administration sets.

The partition coefficient is the ratio of a molecule between two phases under equilibrium conditions. Besides experimentally investigation, thermodynamic models (UNIFAC, GC-FLORY, ELBRO-FV, regular solution theory) and quantitative structure activity relationship (QSAR) have been presented to define the partition coefficient. The diffusion coefficient is a temperature-dependent specific value for a given pair of species. Here, two main models, namely “microscopic” and “atomistic”, are available. The microscopic model relates experimental results, i.e. dependence of diffusion coefficients on temperature, nature of small molecules and its concentration in the polymer, with microscopic parameters, i.e. structure and energy parameters of the diffusing molecule and/or polymer/elastomer. The atomistic models are resolved with computer methods known as Molecular Dynamics (MD) simulations. These techniques deal with elementary physico-chemical data, i.e. chemical structure, electrostatic forces, Van-der-Waals forces. Here, the polymer matrix is generated and Newton's equation of motions for each atom of the molecules in the polymer matrix, or group of them, are solved [14].

Software packages working with mathematical algorithm and material constants are for example offered by FABES. MIGRATEST® LITE and MIGRATEST® EXP simulate the migration of a molecule inside a polymer layer. The diffusion coefficient is estimated by diffusion equations based on molecular weight and temperature. Furthermore, MIGRAPIPE offers an opportunity to simulate diffusion multilayer [15]. In addition, several molecular dynamics simulation software packages exist, i.e. NAMD, GROMACS or AMBER. The work of *Müller et al.* [1] showed that the discussion of leaching also bothers the sector of decontamination technology. They examined the migration of paracetic acid as well as hydrogen peroxide into PVC, polyolefin and polyolefin-polyester bags during their surface decontamination. The results represent that the permeation of hydrogen peroxide is lower than for paracetic acid for all types of polymer bags. Hence, they

recommended hydrogen peroxide as a disinfection medium in connection with polyolefin bags for intravenous solutions.

## **2.2. *Hydrogen Peroxide Decontamination Technology***

To guarantee personal security, as well as to protect packaging, isolators have been used in pharmaceutical industry since 1970. This technology was particularly implemented in semiautomatic filling systems for sterile pharmaceutical products. The cleaning of the system was carried out manually without reproducibility. The sterility inside the isolator, i.e. PVC covering, was achieved by aeration using peracetic acid and formaldehyde. As a disadvantage, this technique led to malodour and chemical residues. At that time different sterilisation methods were tested, i.e. spraying of paracetic acid or hydrogen peroxide, evaporation of paracetic acid, formaldehyde or hydrogen peroxide, paracetic acid/ hydrogen peroxide mixtures, pure saturated steam, saturated steam in combination with hydrogen peroxide, use of ozone and chlorine dioxide. Out of these methods, hydrogen peroxide became widely accepted and the first filling system using hydrogen peroxide-technology was brought on line in 1992 [16].

Till this day two generators for the Decontamination by Hydrogen Peroxyde (DHP) are commercially available. It is important to differentiate between these two generators, as their principles of operation are basically different. The VHP<sup>®</sup> 1000ED generator from STERIS uses a “dry” operation method, while the Clarus<sup>®</sup> C from Bioquell operates with a “wet” method (see Figure 2-1).



**Figure 2-1 - Clarus<sup>®</sup> C (Bioquell) [17] and VHP<sup>®</sup> 1000ED (STERIS) [18].**

In general, both generators operate the decontamination cycle in four phases, namely conditioning (1), ramping (2), decontamination (3) and aeration (4) [19]. The decontamination effect achieved during these different decontamination phases is illustrated in Figure 2-2.

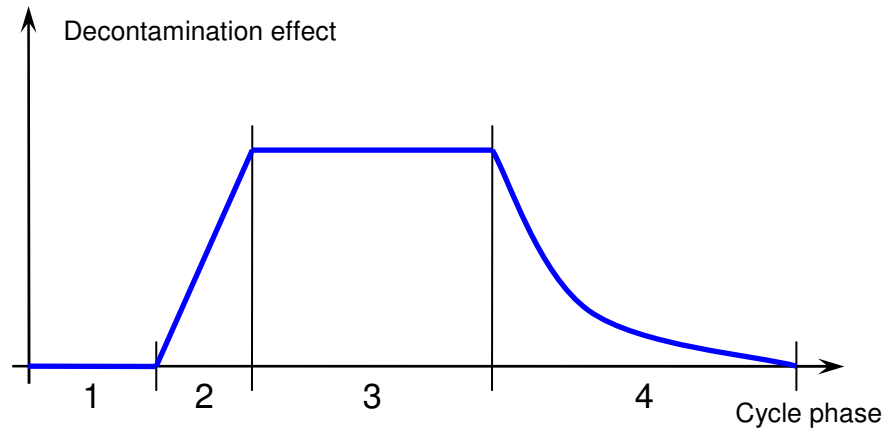


**Figure 2-2 - Phases of a decontamination cycle [4].**

The conditioning phase sets the required temperature and humidity to the desired level. The ramping phase loads hydrogen peroxide into the isolator until the desired concentration is reached. The decontamination phase maintains a stable concentration of hydrogen peroxide until all organisms are inactivated. In the aeration phase, hydrogen peroxide is removed from the isolator until reaching the OSHA level of 0.5 ppm. A catalyst accelerated the process by the conversion of hydrogen peroxide into oxygen and hydrogen [19]. This is the most time-consuming phase in the decontamination cycle. In fact, this is dependent on air flow rate, hydrogen peroxide loading, the size and surface area of the isolator, as well as the absorption behaviour of the materials used inside the isolator [16].

The “dry” method (VHP<sup>®</sup> 1000ED; STERIS) claims that no condensation of hydrogen peroxide occurs. This is achieved by dehumidification of the circulating air and the limitation of the evaporating hydrogen peroxide. Advantages of the “dry” method are a better control of the decontamination cycle without condensation and short decontamination cycles, because no evaporation of a hydrogen peroxide liquid film on surfaces is needed. A disadvantage of this method is the high energy requirement to

remove the water vapour. Also an unintentional condensation can occur due to unwanted cold areas in the decontamination room [6].

On the contrary the “wet” method (Clarus<sup>®</sup> C, Bioquell) aims to create a condensate of hydrogen peroxide. This is called microcondensation, which often occurs invisibly. The microcondensation should be responsible for the inactivation of the bacteria. The desired conditions are reached by oversaturation of the air with hydrogen peroxide and water vapour [19]. The advantages of the “wet” method are the low energy requirement and the low hydrogen peroxide amount during the process. The disadvantage is the poor control of the system because of the invisible microcondensation.

The effectiveness of the hydrogen peroxide decontamination cycle is verified by commercially available Biological Indicators (BIs). These BIs, i.e.  $\geq 1.0 \times 10^6$  spores of *Bacillus stearothermophilus* on a Cr-Ni-steel carrier, are sealed in a hydrogen peroxide permeable packaging (Tyvek) [20]. These carriers are usually placed on the “worst case” airflow locations in the isolators. The “worst case” locations are determined by smoke studies and/or numerical simulations based, i.e., on Computational Fluid Dynamics (CFD) [19]. After the decontamination cycle a  $10^6$  spore reduction must be obtained.

The time of each decontamination cycle phase, the relative humidity, the temperature, the amount and tracking rate of hydrogen peroxide in the isolator, as well as the concentration of hydrogen peroxide in the environment have to be controlled and documented. Alerts and emergency programs leading to a stoppage of the process have to be implemented, if the decontamination procedure achieves the predefined warning limit. Moreover, the DHP leads to a limitation of materials used in the isolators [16]. Table 2-1 presents the hydrogen peroxide compatible materials.

In conjunction with hydrogen peroxide many metals act as catalysts leading to a break-up of hydrogen peroxide in oxygen and hydrogen. It is also known that polymers and elastomers, i.e. PVC, silicone rubber and EPDM, tend to absorb hydrogen peroxide during the decontamination cycle. The desorption of hydrogen peroxide can then be favoured by heating and curbing the system. Thus, steam sterilization of polymers and elastomers outside the isolator and the subsequent sterile transfer into the isolator are commonly preferred [16].

All the considerations above show the importance of the investigation of the absorption behaviour of hydrogen peroxide in different polymers using characteristic material data,

i.e. diffusion coefficient and saturation concentration. In general, polymers and elastomers should be minimized to decrease the aeration time during the decontamination process. Furthermore, particular attention should be paid to the design of the isolator. Smooth and cleanable surfaces, low surface area, few interior equipment and no “worst case” airflow locations must be preferred.

**Table 2-1 - Hydrogen peroxide compatible materials [16].**

<i>metal</i>	Cr-Ni-steel, anodized Al, Hastelloy C, Ti
<i>anorganic non-metallic material</i>	Ceramic, glass, quartz, non-porous enamel
<i>polymer</i>	PTFE, PVDF, PP, PC and (PE, PVC)*
<i>elastomer</i>	Viton and (silicone rubber, EPDM)*
<i>cloves</i>	Chlorosulfonyl polyethylene

\* restrictable material

### 3. Mathematical Models

#### **3.1. Basic Thermodynamic Models for Binary Mixtures**

Whether a mixture of hydrogen peroxide, water vapour and air can condense is determined by the phase equilibrium. Thus, at the interface the fugacity of hydrogen peroxide in the liquid and the gas phase must be equal.

Since the chemical potentials of a species are directly proportional to its fugacity, the relative thermodynamic potential of two mixtures, i.e. H<sub>2</sub>O<sub>2</sub> in the gas and liquid phase, can be judged based on their fugacity.

To calculate the fugacity of H<sub>2</sub>O<sub>2</sub> in the gas phase, the dew point composition of the H<sub>2</sub>O<sub>2</sub>-laden air was read out of the h-x diagram for moist hydrogen peroxide-laden air mentioned by *Radl et al.* [5] at 25°C.

The fugacity of H<sub>2</sub>O<sub>2</sub> in the gas phase is [21]:

$$f_i^g = y_i \cdot \varphi_i \cdot p \quad (1)$$

where  $f_i^g(y_i, p, T)$ ,  $y_i$ ,  $\varphi_i(y_i, T)$  and  $p$  refer to the fugacity of H<sub>2</sub>O<sub>2</sub> in the gas phase [Pa], the molar fraction of H<sub>2</sub>O<sub>2</sub> in the gas phase, the fugacity coefficient and total pressure, which is assumed to be 10<sup>5</sup> [Pa].

For an ideal gas the fugacity coefficient is equal to 1. As a result Eqn. (1) can be described by Dalton's law:

$$f_i^g = p_i = y_i \cdot p \quad (2)$$

where  $p_i$  denotes the partial pressure [Pa].

The concentration of H<sub>2</sub>O<sub>2</sub> in the air [kmol/m<sup>3</sup>] is described by the ideal gas law:

$$c_i = \frac{n_i}{V} = \frac{p_i}{R \cdot T} \quad (3)$$

where  $c_i$ ,  $n_i$ ,  $V$ ,  $p_i$ ,  $R$  and  $T$  refer to the concentration, the amount of substance  $i$ , the volume, the partial pressure of  $H_2O_2$ , the gas constant and the temperature.

Here, the concentration of  $H_2O_2$  in a hydrogen peroxide-laden air at the dew point at 25°C equates to  $7.15E-05$  kmol/m<sup>3</sup>.

The fugacity of  $H_2O_2$  in aqueous solution is:

$$f_i^l = x_i \cdot \gamma_i \cdot p_i^s \quad (4)$$

where  $f_i^l(x_i, T)$ ,  $x_i$ ,  $\gamma_i(x_i, T)$ ,  $p_i^s(T)$  refer to the fugacity of the liquid phase, the molar fraction of  $H_2O_2$  in the liquid phase, the activity coefficient and the vapor pressure of  $H_2O_2$ .

The activity coefficients for  $H_2O_2$  (see Eqn. (5)) and  $H_2O$  (see Eqn. (6)) were calculated by using the four- parametric activity coefficient model mentioned by *Radl et al.* [5].

$$\ln(\gamma_{H_2O_2}) = \frac{x_{H_2O}^2}{R \cdot T} \cdot \left[ \begin{aligned} &B_0(T) + B_1(T) \cdot (3 - 4 \cdot x_{H_2O}) + B_2(T) \cdot (1 - 2 \cdot x_{H_2O}) \cdot (5 - 6 \cdot x_{H_2O}) \\ &+ B_3(T) \cdot (1 - 2 \cdot x_{H_2O})^2 \cdot (7 - 8 \cdot x_{H_2O}) \end{aligned} \right] \quad (5)$$

$$\ln(\gamma_{H_2O}) = \frac{(1 - x_{H_2O})^2}{R \cdot T} \cdot \left[ \begin{aligned} &B_0(T) + B_1(T) \cdot (1 - 4 \cdot x_{H_2O}) + B_2(T) \cdot (1 - 2 \cdot x_{H_2O}) \cdot (1 - 6 \cdot x_{H_2O}) \\ &+ B_3(T) \cdot (1 - 2 \cdot x_{H_2O})^2 \cdot (1 - 8 \cdot x_{H_2O}) \end{aligned} \right] \quad (6)$$

Here,  $R$ ,  $B_n$ ,  $x_i$  and  $\gamma_i$  refer to the molar gas constant, the Redlich-Kister parameters, the molar fraction of  $H_2O_2$  or  $H_2O$  and the activity coefficient of  $H_2O_2$  and  $H_2O$ . Detailed information about the calculation of the activity coefficients of  $H_2O_2$  and  $H_2O$  for a 30 and 70 % (w/w) aqueous  $H_2O_2$  solution at 25°C are mentioned in Appendix 9.1.

The vapor pressure of  $H_2O_2$  was calculated by using a seven-parameter equation presented by *Manatt and Manatt* [22].

$$\log_{10} p_i^s = 24.8436 - 3511.54/T - 4.61453 \log_{10} T - 3.60245 \cdot 10^{-3} T - 7.73423 \cdot 10^{-6} T^2 + 1.78355 \cdot 10^{-8} T^3 - 2.27008 \cdot 10^{-13} T^4 \quad (7)$$

where  $p_i^s$  denotes the vapour pressure of  $H_2O_2$  [mmHg]. The vapor pressure of  $H_2O_2$  corresponds to 303 Pa (i.e., 2.274 mmHg).

In the case of comparing gaseous and liquid H<sub>2</sub>O<sub>2</sub> at 25°C, the results are summarized in Table 3-1.

**Table 3-1 - Fugacity of H<sub>2</sub>O<sub>2</sub> on the gas phase and liquid phase.**

$f_{H_2O_2}^g$ [Pa]	$f_{H_2O_2}^l$ [Pa]
177	32.7

Hence, the reactivity of H<sub>2</sub>O<sub>2</sub> in the gas phase is approximately five times higher than in the liquid phase.

### 3.2. Absorption and Desorption in Solids

#### 3.2.1. Implementation of an Absorption Model for the System H<sub>2</sub>O<sub>2</sub> in Polymers

For the implementation of an absorption model for H<sub>2</sub>O<sub>2</sub> in polymers, Fick's Second Law is used. This equation describes the diffusion of a migrant between two phases, i.e. the diffusion of H<sub>2</sub>O<sub>2</sub> between an aqueous solution of H<sub>2</sub>O<sub>2</sub> and the polymer.

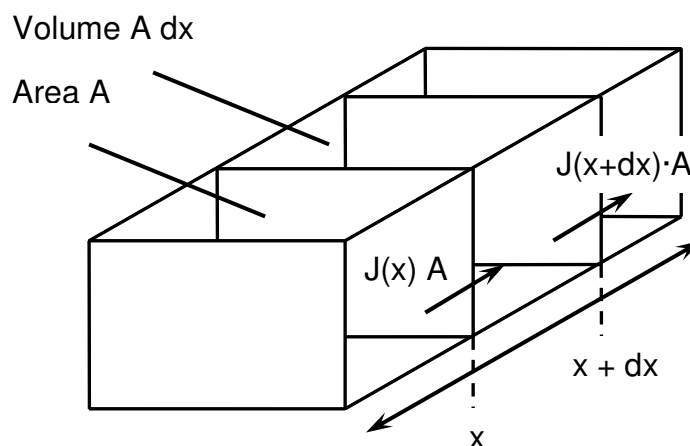


**Figure 3-1 - Schematic sketch of the diffusion in a volume element [24].**

The mass balance of a defined volume element (see Figure 3-1) can be illustrated as follows [23]:

*Input = Output + Accumulation + Reaction*

For our purposes we assume that diffusion occurs only in x-direction and the reaction term is not taken into account. This leads to a simplification and, after rearrangement, the mass balance can be written as follows:

*Accumulation = Input - Output*

The accumulation term specifies the time-dependent change of concentration, whereas input and output of the migrant per time can be described with the diffusion flux  $J$  multiplied with the area  $A$  and divided by the element volume [24]:

$$\frac{\partial C}{\partial t} = \frac{N_{in} - N_{out}}{A \cdot dx} = \frac{J(x) \cdot A - [J(x+dx) \cdot A]}{A \cdot dx} = \frac{J(x) - \left[ J(x) + \left( \frac{\partial J}{\partial x} \right) dx \right]}{dx} = - \left( \frac{\partial J}{\partial x} \right) \quad (8)$$

Finally, by introducing Fick's First Law for the term  $J$ , Equation (8) is equal to Fick's Second Law:

$$\frac{\partial C}{\partial t} = D \frac{\partial^2 C}{\partial x^2} \quad (9)$$

Here,  $D$  is the diffusion coefficient of  $H_2O_2$  in the polymer matrix [ $m^2/s$ ]. This value is specific for a given pair of species. Furthermore the diffusivity depends on temperature.

Due to the fact that few literature values on diffusion coefficients of  $H_2O_2$  in polymers are available, the diffusion coefficient needs to be estimated for this system with a refined equation for polyolefins and other polymers (*Begley et al.* [25]).

In our work the upper diffusion coefficients for different polymers were calculated with equation (10) and (11).

$$D_p^* = 10^4 \exp \left[ A_p - 0.1351M_i^{2/3} + 0.003M_i - \frac{10454}{T} \right] \quad (10)$$

$$A_p = A'_p - \frac{\tau}{T} \quad (11)$$

$D_p^*$  [ $\text{cm}^2/\text{s}$ ] is the upper diffusion coefficient and  $A_p$  is the upper-bond conductance, which depends on characteristic values for each polymer obtainable by experimental data.

Note that these equations are used for calculating the diffusion coefficient in the food and packaging industry. To make sure that the migrant from packaging in food is below the critical level, the calculation is carried out with a diffusion coefficient, which is comparatively higher than the real one.

Equations (10) and (11) were solved for  $\text{H}_2\text{O}_2$  and following polymers: LDPE/LLDPE, HDPE, PP (homo and random), PP (rubber), PS, HIPS, PET, PEN and PA (6,6) at  $25^\circ\text{C}$ . The results are illustrated in Table 3-2.

Here, the diffusion coefficients are spread between  $10^{-7}$  and  $10^{-12}$   $\text{cm}^2/\text{s}$ .

**Table 3-2 - Calculation of diffusion coefficients of  $\text{H}_2\text{O}_2$  in different polymers;  $M_i= 34.02$  g/mol,  $T = 298.15$  K.**

<i>Polymer</i>	$A'_p$	$\tau$	$T$ [K]	$A_p$	$D_p^*$ [ $\text{cm}^2 \text{s}^{-1}$ ]
LDPE/LLDPE	11.5	0	298.15	11.50	1.57E-07
HDPE	14.5	1577	298.15	9.21	1.59E-08
PP (homo and random)	13.1	1577	298.15	7.81	3.92E-09
PP (rubber)	11.5	0	298.15	11.50	1.57E-07
PS	0.0	0	298.15	0.00	1.59E-12
HIPS	1.0	0	298.15	1.00	4.31E-12
PET	6.0	1577	298.15	0.71	3.23E-12
PEN	5.0	1577	298.15	-0.29	1.19E-12
PA (6,6)	2.0	0	298.15	2.00	1.17E-11

The diffusion coefficients calculated from experiments for CH<sub>4</sub> in PE and PET were found in literature (*Piringer et al.* [14]). To compare the diffusion coefficients of H<sub>2</sub>O<sub>2</sub> in these polymers the diffusion coefficients were calculated with equations (10) and (11) for the same temperatures. The results are illustrated in Table 3-3.

**Table 3-3 - Comparison of diffusion coefficients of CH<sub>4</sub> and H<sub>2</sub>O<sub>2</sub> in PE and PET at different temperatures.**

	$M_i$	$D_p [cm^2 s^{-1}]$ PE at 298 K	$D_p [cm^2 s^{-1}]$ PET at 340 K
<i>Experimental values of CH<sub>4</sub></i>	16.04	5.40E-07	9.20E-09
<i>Calculated values of H<sub>2</sub>O<sub>2</sub></i>	34.02	1.57E-07 (LDPE) 1.59E-08 (HDPE)	4.82E-10

Equation (10) takes into account the molecular weight and the temperature. This means on the one hand that migrants with higher molecular weight have a lower diffusion coefficient, and on the other hand, that higher temperature leads to higher diffusion coefficients. The range of the calculated diffusion coefficients of H<sub>2</sub>O<sub>2</sub> in PE and PET seems to be an appropriate estimation compared to the experimental diffusion coefficients of CH<sub>4</sub>. Both diffusion coefficients of H<sub>2</sub>O<sub>2</sub> are lower because of its higher molecular weight.

To calculate the penetration of H<sub>2</sub>O<sub>2</sub> during the decontamination cycle, the partial differential equation of Fick's Second Law (9) has to be solved.

The solution for a semi-infinite material is described by following equation (*Bird et al.* [26]):

$$\frac{C_x - C_0}{C_s - C_0} = \frac{C_x}{C_s} = 1 - \operatorname{erf} \frac{x}{\sqrt{4Dt}} \quad (12)$$

Here, x and t refer to the diffusion thickness [cm] and time [s].

C<sub>0</sub> describes the concentration of H<sub>2</sub>O<sub>2</sub> of the polymer at 0 ≤ x ≤ ∞ at t = 0, which is the concentration in the polymer at the beginning of the H<sub>2</sub>O<sub>2</sub> decontamination. In this case

$C_0$  is zero.  $C_s$  describes the constant surface concentration of  $H_2O_2$  on the polymer at  $x=0$ .  $C_x$  describes the concentration of  $H_2O_2$  in the polymer at  $x$  at time  $t$ .

As an example for high diffusion and low diffusion of  $H_2O_2$  the penetration of  $H_2O_2$  in PET and LDPE was estimated by plotting  $C_x/C_s$  against  $x$  at different times (10 min, 1 h, 5h, 10h) (see Figure 3-2).

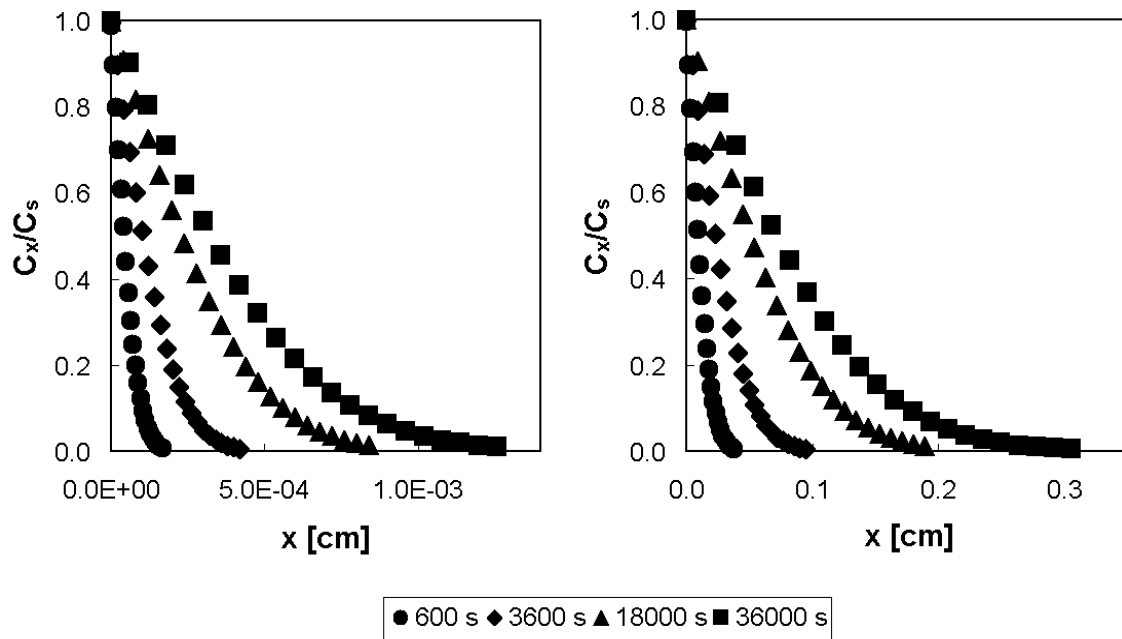


**Figure 3-2 - Diffusion concentration profile of  $H_2O_2$  in PET,  $D= 3.23E-12 \text{ cm}^2 \text{ s}^{-1}$  at 298.15 K (left); Diffusion concentration profile of  $H_2O_2$  in LDPE,  $D= 1.57E-07 \text{ cm}^2 \text{ s}^{-1}$  at 298.15 K (right).**

The diffusion coefficient of  $H_2O_2$  in LDPE is 50000 times higher than in PET. This is the reason why  $H_2O_2$  migrates 300 times deeper into LDPE than into PET. After 10 hours of decontamination cycle the penetration thickness of  $H_2O_2$  in LDPE is 0.3 cm, while 1.3E-03 cm in PET. Because of that enormous differences in the diffusion coefficients, it is obvious that the  $H_2O_2$  desorption time varies for each polymer. For instance, using PET instead of LDPE leads to much lower aeration times after the decontamination cycle.

Moreover, a plane sheet, a sphere or a cylinder show different concentration profiles of  $H_2O_2$ . Therefore, each geometry has to be taken into account for solving Fick's second law.

A schematic sketch of the concentration profiles during an absorption process of hydrogen peroxide in a infinite and semi-infinite plane polymer sheet is shown in Figure 3-3.

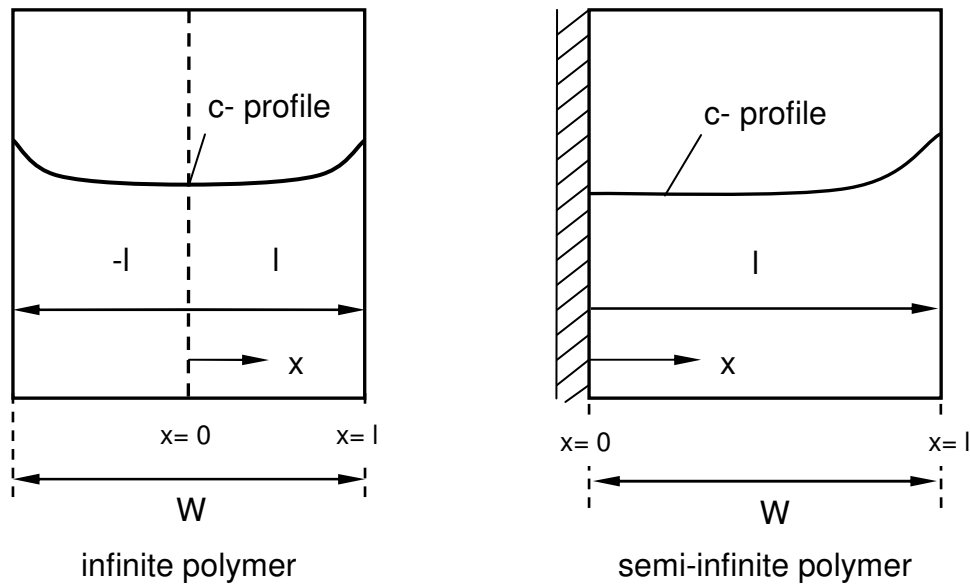


**Figure 3-3 - Schematic sketch of the concentration profile in a finite and semi-infinite plane polymer sheet.**

The concentration profile in the finite polymer is symmetrical, which means that  $\text{H}_2\text{O}_2$  diffuses from both  $x$ -directions into the polymer. Because of this, the width of the polymer is divided into halves. The concentration profile is calculated from  $x=0$ , i.e. the centre of the polymer, to  $x=\pm l$ , i.e. the surface.

The concentration profile in the semi-infinite polymer, i.e. a one side-isolated polymer, is calculated over the total width. This means that  $x=0$  represents the isolated surface and  $x=l$  describes the surface absorbing  $\text{H}_2\text{O}_2$ .

The concentration profile of a plane sheet is shown in Eqn. (14) (Bird *et al.* [26]).

$$\frac{C - C_0}{C_1 - C_0} = 1 - 2 \cdot \sum_{n=0}^{\infty} \frac{(-1)^n}{\left(n + \frac{1}{2}\right) \cdot \pi} \exp\left[-\left(n + \frac{1}{2}\right)^2 \pi^2 Dt / l^2\right] \cos\left(\left(n + \frac{1}{2}\right) \frac{\pi x}{l}\right) \quad (14)$$

$C_1$  and  $C$  refer to the concentration of  $\text{H}_2\text{O}_2$  on the surface, i.e. the saturation concentration of the polymer, and the concentration of  $\text{H}_2\text{O}_2$  at location  $x$  and time  $t$ .

Equation (14) includes the following three important dimensionless variables:

$$\text{Dimensionless concentration} \quad \Theta = \frac{C - C_0}{C_1 - C_0} \quad (15)$$

$$\text{Dimensionless coordinate} \quad \eta = \frac{x}{l} \quad (16)$$

$$\text{Dimensionless time} \quad \tau = Fo = \frac{D \cdot t}{l^2} \quad (17)$$

The dimensionless time is also called the Fourier number. This number describes the ratio of mass transfer to mass storage.

In contrast, the concentration profile in a sphere is described by following equation (Crank [27]):

$$\frac{C - C_0}{C_1 - C_0} = 1 + \frac{2 \cdot a}{\pi \cdot r} \sum_{n=1}^{\infty} \frac{(-1)^n}{n} \cdot \sin \frac{n \cdot \pi \cdot r}{a} \cdot \exp(-D \cdot n^2 \cdot \pi^2 \cdot t / a^2) \quad (18)$$

Here,  $r = \pm a$  describes the surface and  $r = 0$  describes the centre of the polymer sphere. By replacing  $x$  with  $r$  and  $l$  with  $a$ , the solution of Fick's Second Law for a sphere comprises the three dimensionless variables as well.

The concentration profiles for a plane polymer sheet and a polymer sphere (see Eqn. (14) and (18)) can be drawn in terms of the dimensionless parameters  $\eta$  (see Eqn. (16)) and the  $Fo$  (see Eqn. (17)), as illustrated in Figure 3-4.

According to Figure 3-4, the concentration of  $H_2O_2$  in the polymer increases by increasing the Fourier number. In other words, a high concentration of  $H_2O_2$  in the polymer can be reached with high diffusion coefficients and/or absorption times of  $H_2O_2$  in the polymer.

Compared to the concentration profile in a sheet, the saturation concentration in a sphere is reached far earlier. This means that the absorption time of  $H_2O_2$  in a polymer sphere is lower compared to a polymer sheet. The reason for this difference is the larger surface of the sphere.

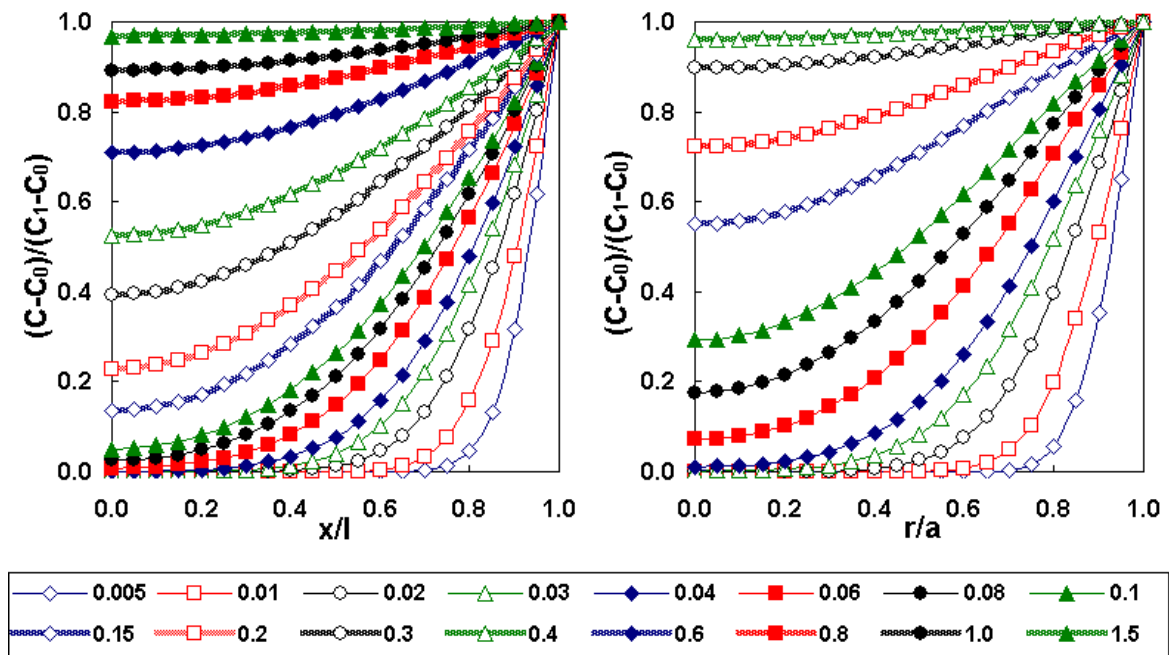


Figure 3-4 - Concentration distributions at various Fourier numbers in a plane polymer sheet (left); Concentration distributions at various Fourier numbers in a polymer sphere (right).

The average normalized concentration represents the average locally normalized concentration over the total transferred area (see Eqn. (19)) and can be calculated by integration of Eqn. (14) for a plane sheet or Eqn. (18) for a sphere. For a sphere the integration is carried out by use of the numerical Simpson’s rule.

$$\frac{\bar{C}}{C_1} = \int_{\eta=0}^{\eta=1} \frac{C}{C_1} d\eta \quad (19)$$

The average normalized concentrations for a plane sheet and a sphere for different Fourier numbers are shown in Figure 3-5. A 99 % saturation is reached in a plane sheet with a Fourier number of 1.8, whereas a sphere already reaches this condition with a Fourier number of 0.5. This means, that a polymer sphere is saturated 3.6 times faster than a polymer sheet.

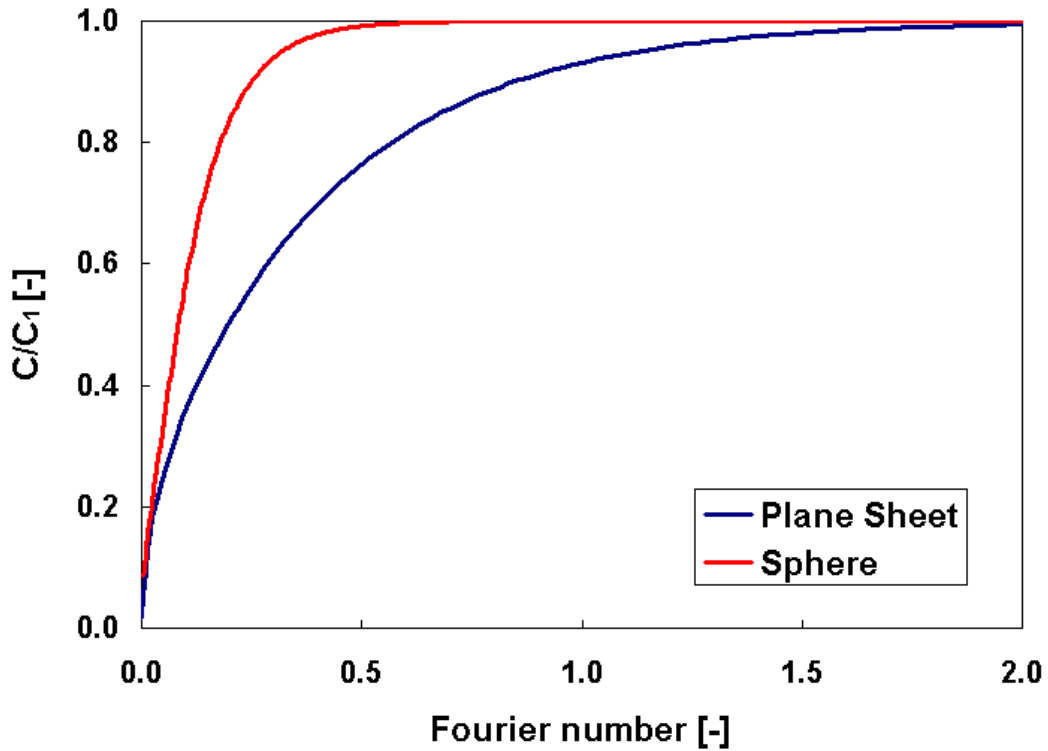


Figure 3-5 - Average normalized concentrations against Fourier numbers for a plane sheet and a sphere.

As Eqn. (19) illustrates,  $C_1$ , i.e. the saturation concentration of  $H_2O_2$  in polymers, has to be defined.

Because there is no data available, the solubility data for  $H_2O$  (at 25°C and 100 % relative humidity) in PVC, LDPE and PP found in literature (*Mueller et al.* [1]) were used to calculate a comparable saturation concentration for  $H_2O_2$ . Therefore, Eqn. (20) was solved for a 30 and 70 % (w/w) aqueous  $H_2O_2$  solution.

$$C_i^{sat} = x_i \cdot \gamma_i \cdot C_{H_2O/Polymer}^{sat} \quad (20)$$

$C_i^{sat}$  and  $C_{H_2O/Polymer}^{sat}$  refer to the saturation concentration of  $H_2O_2$  or  $H_2O$  for a 30 and 70 % (w/w) aqueous  $H_2O_2$  solution and the saturation concentration of  $H_2O$  in PVC, LDPE and PP (shown in Table 3-4). Here, the densities for each polymer refer to the Polymer Data Handbook [28]. The molar fractions and activity coefficients for a 30 and 70 % (w/w) aqueous  $H_2O_2$  solutions are mentioned in Appendix 9.1.

**Table 3-4 - Concentration of H<sub>2</sub>O [kmol m<sup>-3</sup>] in different polymers at equilibrium state [1].**

<i>Polymer</i> [0.1 kg]	<i>m</i> <sub>H<sub>2</sub>O</sub> [kg]	<i>N</i> <sub>H<sub>2</sub>O</sub> [kmol]	<i>ρ</i> <sub>Polymer</sub> [kg m <sup>-3</sup> ]	<i>V</i> <sub>Polymer</sub> [m <sup>3</sup> ]	<i>C</i> <sub>H<sub>2</sub>O/Polymer</sub> <sup>sat</sup> [kmol m <sup>-3</sup> ]
PVC	1.50E-03	8.33E-05	1352	7.40E-05	1.13E+00
LDPE	6.20E-06	3.44E-07	855	1.17E-04	2.95E-03
PP	7.10E-06	3.94E-07	868	1.15E-04	3.42E-03

The saturation concentrations of H<sub>2</sub>O and H<sub>2</sub>O<sub>2</sub> for a 30 and a 70 % (w/w) aqueous H<sub>2</sub>O<sub>2</sub> solution in PVC, LDPE and PP are illustrated in Table 3-5.

**Table 3-5 - Saturation concentrations of H<sub>2</sub>O and H<sub>2</sub>O<sub>2</sub> for a 30 % (w/w) and 70 % (w/w) aqueous H<sub>2</sub>O<sub>2</sub> solution in different polymers at 298.15K.**

<i>Polymer</i>	70 % (w/w) H <sub>2</sub> O <i>C</i> <sub>H<sub>2</sub>O</sub> <sup>sat</sup> [kmol m <sup>-3</sup> ]	30 % (w/w) H <sub>2</sub> O <sub>2</sub> <i>C</i> <sub>H<sub>2</sub>O<sub>2</sub></sub> <sup>sat</sup> [kmol m <sup>-3</sup> ]	30 % (w/w) H <sub>2</sub> O <i>C</i> <sub>H<sub>2</sub>O</sub> <sup>sat</sup> [kmol m <sup>-3</sup> ]	70 % (w/w) H <sub>2</sub> O <sub>2</sub> <i>C</i> <sub>H<sub>2</sub>O<sub>2</sub></sub> <sup>sat</sup> [kmol m <sup>-3</sup> ]
PVC	8.69E-01	9.63E-02	3.46E-01	5.15E-01
LDPE	2.27E-03	2.51E-04	9.04E-04	1.34E-03
PP	2.63E-03	2.92E-04	1.05E-03	1.56E-03

Based on these first calculations, PVC shows an approximately 350 times higher saturation concentration of H<sub>2</sub>O<sub>2</sub> than LDPE and PP. On the other hand, both LDPE and PP show no notable difference concerning the saturation concentration. The 70 % (w/w) aqueous H<sub>2</sub>O<sub>2</sub> solution reaches a five times higher saturation concentration of H<sub>2</sub>O<sub>2</sub> in the polymer compared to the 30 % (w/w) aqueous H<sub>2</sub>O<sub>2</sub>.

Furthermore, the partition coefficient K, i.e. the ratio of the concentration of H<sub>2</sub>O between the polymer phase and the liquid phase under equilibrium conditions, can be calculated. Therefore, the saturation concentration of H<sub>2</sub>O in different polymers (see Table 3-4) is divided by the concentration of pure water, i.e. 55.56 kmol/m<sup>3</sup>.

The results for the partition coefficients of H<sub>2</sub>O in different polymers at 25°C are illustrated in Table 3-6.

**Table 3-6 - Partition coefficient [kmol m<sup>-3</sup>]/[kmol m<sup>-3</sup>] of different H<sub>2</sub>O/polymer systems.**

<i>K</i>	H <sub>2</sub> O/PVC	H <sub>2</sub> O/LDPE	H <sub>2</sub> O/PP
<i>C</i> <sub>H<sub>2</sub>O/Polymer</sub> [kmol m <sup>-3</sup> ]/ <i>C</i> <sub>H<sub>2</sub>O/Water</sub> [kmol m <sup>-3</sup> ]	2.03E-02	5.30E-05	6.16E-05

Hence, it is possible to calculate the average concentration of  $H_2O_2$  [kmol/m] in LDPE and PP (homo and random) using Eqn. (21) for a 30 % (w/w) aqueous  $H_2O_2$  solution.

$$\bar{C}_{H_2O_2} = \frac{\bar{C}}{C_1} \cdot C_1 \quad (21)$$

The concentration of  $H_2O_2$  was determined for a infinite and semi-infinite polymer sheet with two different dimensions [ $L \times W \times H$  [ $m^3$ ];  $0.3 \times 0.001 \times 0.2$  [ $m^3$ ];  $0.3 \times 0.01 \times 0.2$  [ $m^3$ ]] and for three different absorption times (10 min, 1 h, 5h, 10h). The diffusion coefficients for LDPE and PP (homo and random) were taken from Table 3-2, whereas the results for the saturation concentration of  $H_2O_2$  in LDPE and PP, i.e.  $C_1$ , were taken from Table 3-5. The concentration profiles of  $H_2O_2$  in LDPE and PP (homo and random) for a 30 % (w/w) aqueous  $H_2O_2$  solution are presented in Figure 3-6 and Figure 3-7.

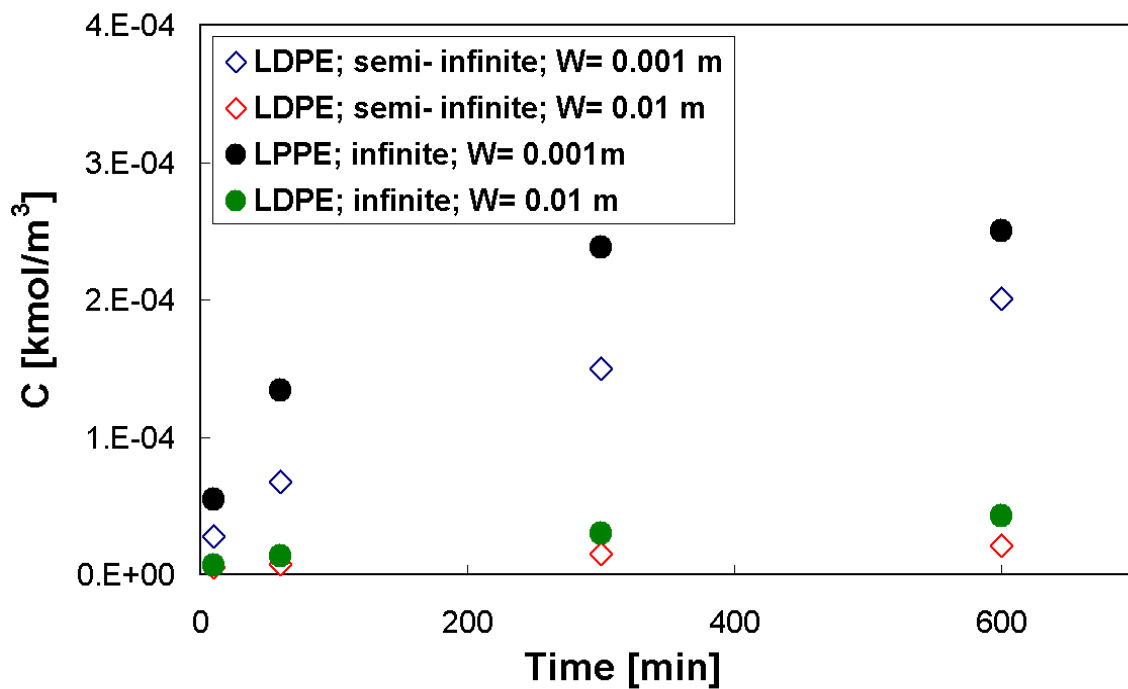


Figure 3-6 - Concentration of  $H_2O_2$  for a 30 % (w/w) aqueous  $H_2O_2$  solution in a semi-infinite and infinite LDPE;  $D= 1.57E-07 \text{ cm}^2 \text{ s}^{-1}$ ,  $C_1=2.51E-04 \text{ kmol m}^{-3}$ .

Figure 3-6 illustrates that an infinite LDPE polymer with a width of 0.001 m reaches the saturation concentration after 10 hours. For the semi-infinite polymer of the same width 80 % of the saturation concentration can be achieved. There is no big difference of the

concentration profile between an infinite and a semi-infinite polymer with a width of 0.01 m. Both will not reach the calculated saturation concentration by far.

Because of the equal diffusion coefficient and minor differences in the saturation concentration, similar results are expected for the concentration profile of H<sub>2</sub>O<sub>2</sub> in PP rubber.

Compared to the diffusion of H<sub>2</sub>O<sub>2</sub> in LDPE, the lower diffusion coefficient of 3.91E-09 cm<sup>2</sup>/s has a large influence on the concentration profile. The semi-infinite as well as the infinite PP sheets, whatever width is used, will never reach the saturation concentration after 10 hours. In this case a thinner polymer sheet should be used to achieve the saturation condition.

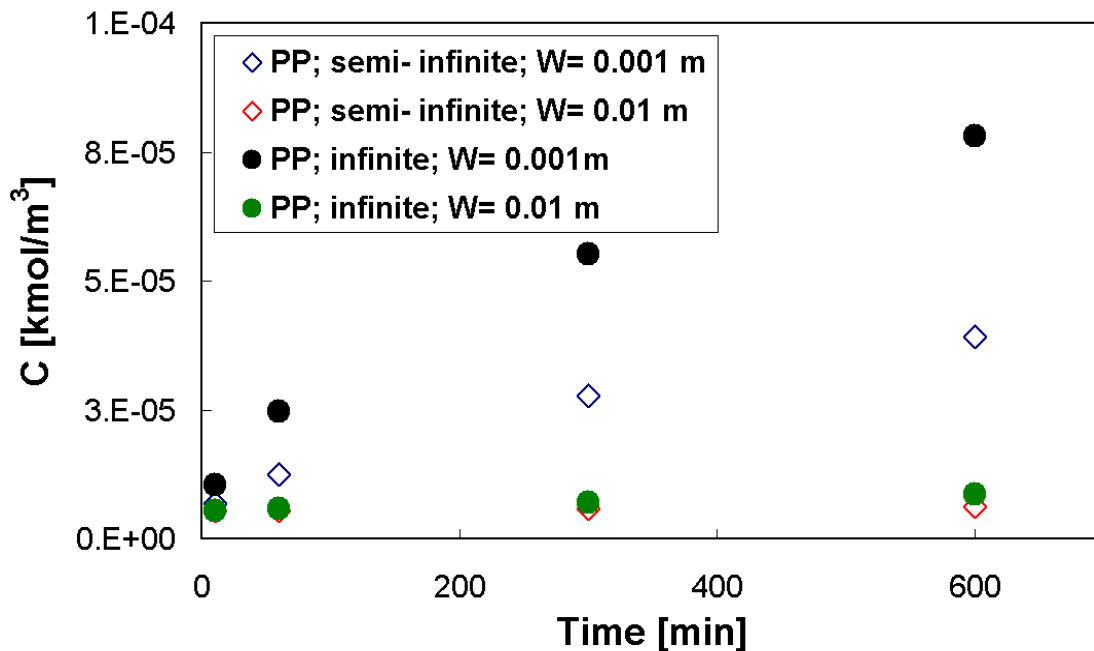


Figure 3-7 - Concentration of H<sub>2</sub>O<sub>2</sub> for a 30 % (w/w) aqueous H<sub>2</sub>O<sub>2</sub> solution in a semi-infinite and infinite PP (homo and random); D= 3.91E-09 cm<sup>2</sup> s<sup>-1</sup>, C<sub>1</sub>= 2.92E-04 kmol m<sup>-3</sup>.

In summary, the best geometry for analyzing absorption and desorption effects would be a sphere. Because of better handling, plane polymer sheets are nevertheless used in our work, even accepting longer saturation times. In order to at least reduce the experimental effort, polymer foils with a width under 0.001 m are selected for our measurements.

A LDPE polymer sheet with a volume of 6.E-5 m<sup>3</sup> comprises approximately 15 μmol of H<sub>2</sub>O<sub>2</sub> after reaching the saturation concentration. Due to this fact, a measurement

method which is sensitive for  $\mu\text{mol}$  range should be investigated. In this case the Amplex® Red Hydrogen/ Peroxidase Assay Kit from Invitrogen is used.

### 3.2.2. Calculation of the Diffusion Coefficient and Saturation Concentration in Polymers

For the experimental determination of the saturation concentration and the diffusion coefficient of  $\text{H}_2\text{O}_2$  in the polymer, Eqn. (23) was used.

$$\frac{\bar{C}_{\text{H}_2\text{O}_2}}{C_{\text{H}_2\text{O}_2}^{\text{sat}}} = 1 - \left( 2 \cdot \sum_{n=0}^{\infty} \frac{(-1)^n}{\left( \left( n + \frac{1}{2} \right) \cdot \pi \right)^2} \exp \left[ - \left( n + \frac{1}{2} \right)^2 \pi^2 D t / l^2 \right] \sin \left( \left( n + \frac{1}{2} \right) \pi \right) \right) \quad (23)$$

The diffusion coefficient and the saturation concentration were fit such that squared differences of  $\bar{C}_{\text{H}_2\text{O}_2}$  in Eq. (23) with the experimental data were minimal. Taking into account the volume of the liquid used for desorption the averaged desorbed amount of  $\text{H}_2\text{O}_2$  (see Eqn. (24)) in  $\mu\text{M}$  can be calculated. This was done using the “Solver” function in MS Excel. Often it was necessary to manually adjust the diffusion coefficient during this calculation procedure. The correlations between the experimental curves and the prediction model of polymers are illustrated in the figures mentioned in Appendix 9.3.

$$\bar{C}_{\text{H}_2\text{O}_2} = \frac{V_{\text{Polymer}}}{V_{\text{Liquid}}} \cdot C_{\text{H}_2\text{O}_2}^{\text{sat}} \cdot \frac{\bar{C}_{\text{H}_2\text{O}_2}}{C_{\text{H}_2\text{O}_2}^{\text{sat}}} \cdot 10^9 \quad (24)$$

The standard deviation  $\sigma$  of the arithmetic mean of the concentration was calculated using Eqn. (25).

$$\sigma = \sqrt{\frac{\sum (x - \bar{x})^2}{(n-1)}} \quad (25)$$

### 3.3. Mass Transfer from the Polymer into the Fluid Phase

A schematic sketch of the concentration profiles during a desorption process of hydrogen peroxide from a polymer is shown in Figure 3-8.

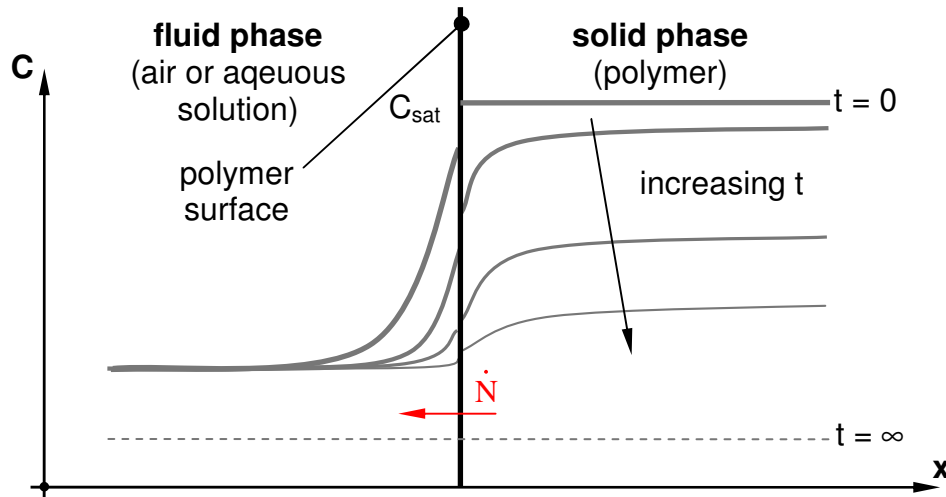


Figure 3-8 - Schematic sketch of the concentration profiles occurring during the desorption process from a polymer.

Initially, the polymer is assumed to be saturated with a defined concentration of  $\text{H}_2\text{O}_2$ , while the concentration of  $\text{H}_2\text{O}_2$  in the liquid phase (e.g., air) is zero. The system wants to compensate the occurring concentration difference by mass transport of  $\text{H}_2\text{O}_2$  from the polymer phase to the liquid phase. During this process,  $\text{H}_2\text{O}_2$  is in equilibrium between the liquid phase and the polymer phase only at the boundary.

This equilibrium is defined by the partition coefficient  $K$  as shown in Eqn. (26).

$$K = \frac{C_{i,s}}{C_{i,liq}} \quad (26)$$

Here “i” denotes the diffusing species (e.g., hydrogen peroxide), “s” denotes the solid and “liq” denotes the liquid phase. The partition coefficient is the ratio of the concentration of a solute between two phases under equilibrium conditions, which is assumed to be

present at the polymer surface. It is a function of the solute as well as of the properties of the two phases in contact, i.e., the liquid phase and the polymer.

In the current work it is assumed that a quasi steady-state concentration profile within the fluid boundary layer is present. This is justified by the comparably high diffusion coefficient in the liquid phase compared to the solid. Diffusion of H<sub>2</sub>O<sub>2</sub> in the solid phase, however, is non-steady-state and can be described by Fick's Second Law, see Eqn. (27).

$$\frac{\partial C_{i,solid}}{\partial t} = D_{i,solid} \frac{\partial^2 C_{i,solid}}{\partial x^2} \quad (27)$$

The diffusion in the polymer phase depends on the Fourier number (see Eqn. (28)). This dimensionless number describes the mass transfer. It is the ratio of mass transfer by diffusion to mass storage.

$$Fo = \frac{D_{i,solid} \cdot t}{L^2} \quad (28)$$

Here,  $D_{i,solid}$ ,  $t$  and  $L$  refer to the diffusion coefficient of a species in the solid phase, time and the characteristic length of the solid phase.

To describe the characteristics of the mass transfer of H<sub>2</sub>O<sub>2</sub> in the liquid phase, the mass transfer coefficient  $\beta$  [m/s] was calculated. Air with three different flow rates (0.1, 5 and 10 m/s) over a plane sheet with  $L = 0.2$  m, i.e., the length of the polymer, has been considered for this purpose (see Figure 3-9). The kinematic viscosity  $\nu_{liq}$  of air at a temperature of 20°C has been assumed to be 1.513E-05 m<sup>2</sup>/s [27].

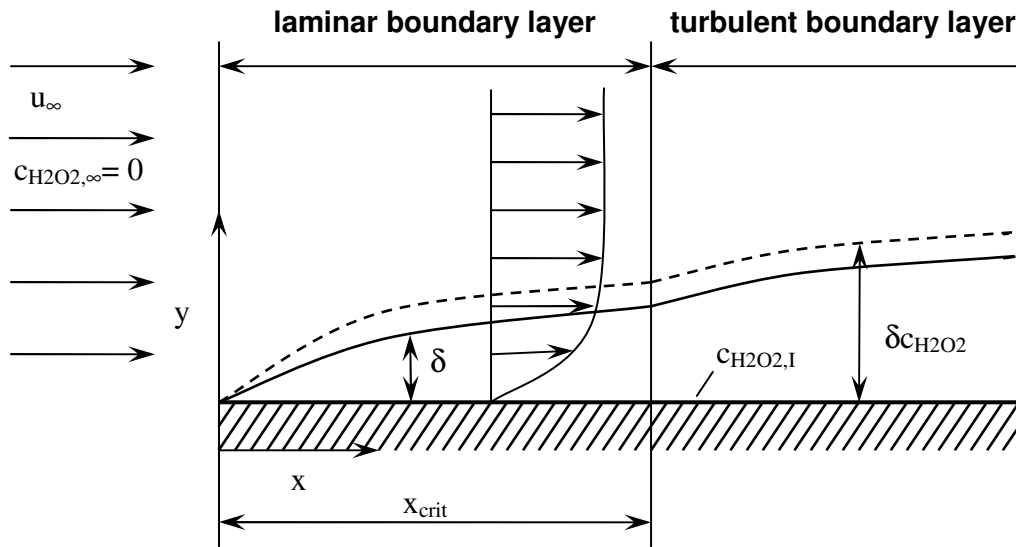


Figure 3-9 - Velocity boundary layer and concentration boundary layer [30].

The Reynolds number has been defined as:

$$\text{Re} = \frac{u_\infty \cdot L}{\nu_{\text{liq}}} \quad (29)$$

For  $10 \leq \text{Re} \leq 10^7$  and  $0.7 \leq \text{Sc} \leq 70.000$ , the mean Sherwood number (i.e., the Sherwood number averaged over the length  $L$ ) for the flow over a flat plate can be estimated using the Krischer and Kast correlation [30].

$$\text{Sh} = \sqrt{\text{Sh}_{\text{lam}}^2 + \text{Sh}_{\text{turb}}^2} \quad (30)$$

$\text{Sh}_{\text{lam}}$  is calculated using the Pohlhausen correlation (Eqn. (31)), while  $\text{Sh}_{\text{turb}}$  is estimated using the Petukhov and Popov correlation, see Eqn. (32).

$$\text{Sh}_{\text{lam}} = 0.664 \cdot \sqrt{\text{Re}} \cdot \text{Sc}^{1/3} \quad (31)$$

$$\text{Sh}_{\text{turb}} = \frac{0.037 \cdot \text{Re}^{0.8} \cdot \text{Sc}}{1 + 2.443 \cdot \text{Re}^{-0.1} \cdot (\text{Sc}^{2/3} - 1)} \quad (32)$$

For the calculation of the diffusion coefficient of H<sub>2</sub>O<sub>2</sub> in air, the correlation of Fuller/Schettler/Giddings was used. (see Eqn. (33)).

$$D_{i,liquid} = \frac{1.43 \cdot 10^{-7} \cdot T^{1.75}}{p \cdot M_{G,12}^{0.5} \cdot \left[ \left( \sum v \right)_1^{1/3} + \left( \sum v \right)_2^{1/3} \right]^2} \quad (33)$$

Where p, T, v and M<sub>G,12</sub> refer to the pressure, i.e. 1 bar, temperature, atomic diffusion volume and the molecular weight, which was calculated using Eqn. (34)

$$M_{G,12} = \frac{2}{\frac{1}{M_{G,1}} + \frac{1}{M_{G,2}}} \quad (34)$$

Where M<sub>G,1</sub> and M<sub>G,2</sub> is the molecular weight of H<sub>2</sub>O<sub>2</sub> and air.

The Sherwood number is multiplied by the diffusion coefficient and divided by the characteristic length to calculate the mass transfer coefficient. The results for the calculation of the mass transfer coefficient for the flow over a flat plate are shown in Table 3-7.

**Table 3-7 - Results for the mass transfer coefficient of three different velocities (L= 0.2 m, Sc= 0.79, D<sub>i,liq</sub>= 1.92E-05 m<sup>2</sup> s<sup>-1</sup>).**

$u_{\infty} [m s^{-1}]$	$Re$	$Sh$	$\beta [m s^{-1}]$
0.1	1322	25	2.39E-03
5	66094	285	2.73E-02
10	132188	467	4.47E-02

As the Reynolds number increases convective transport of H<sub>2</sub>O<sub>2</sub> is accelerated and more H<sub>2</sub>O<sub>2</sub> is transported into the surrounding liquid.

If the concentration on the polymer surface is known, the mass flow  $\dot{N}$  [mol/s] from the polymer into the gas phase can be determined from Eqn. (35):

$$\dot{N} = \beta \cdot A \cdot (c_{H_2O_2,I} - c_{H_2O_2,\infty}) \quad (35)$$

where  $c_{H_2O_2,I}$  and  $c_{H_2O_2,\infty}$  denote the concentration of  $H_2O_2$  at the interface and the concentration of  $H_2O_2$  at great distance.

However, the interface concentration depends on the concentration profile in the polymer, which is analyzed as follows.

To gain more information about  $H_2O_2$  transport in the polymer, the cases of short and long contact time between a disperse phase (polymer sheet) and a continuous phase (liquid phase) have been studied.

The mass transport resistance in the polymer relating to the disperse phase (i.e., the polymer) is defined by Eqn. (36).

$$r_{disperse\ phase,\ polymer} = \frac{1}{\beta_{polymer}} = \frac{l_c}{Sh_{polymer} D_{i,\ polymer}} \quad (36)$$

where  $\beta_{polymer}$ ,  $Sh_{polymer}$  and  $D_{i,\ polymer}$  refer to the mass transfer coefficient in the polymer, the Sherwood number in the polymer phase and the diffusion coefficient of  $H_2O_2$  in LDPE. The latter is equal to  $1.6E-11\ m^2/s$ . Here,  $l_c$  describes the characteristic length of the polymer sheet. If the mass transport occurs from both sides of the polymer sheet, half of the sheet thickness is used for the characteristic length.

The mass transport resistance in the liquid phase relating to the disperse phase is defined by Eqn. (37) [30].

$$r_{disperse\ phase,\ liquid} = \frac{K_i}{\beta} = \frac{K_i L}{Sh D_{i,\ liquid}} \quad (37)$$

Here,  $K_i$  describes the partition coefficient of water in the polymer; (e.g.,  $5E-05$  for LDPE). This value should act as an approximation for the partition coefficient of  $H_2O_2$  in the polymer. The values for the diffusion coefficient of  $H_2O_2$  in air, the mass transfer coefficient in gas and the Sherwood number are taken from Table 3-7 for the case of a velocity of  $5\ m/s$ .

### 3.3.1. Short Contact Times

For short contact times the concentration change occurs only near the interface. The mass transfer coefficient for the fluid phase and the polymer phase can be calculated using the penetration theory:

$$\beta = 2\sqrt{\frac{D_{i, liquid}}{\pi\Delta t}} \quad (38)$$

$$\beta_{polymer} = 2\sqrt{\frac{D_{i, polymer}}{\pi\Delta t}} \quad (39)$$

where  $\Delta t$  denotes the time after the contact.

Predictions of the mean resistance in the continuous phase and disperse phase can be calculated by the ratio of  $r_{disperse\ phase, liquid}$  to  $r_{disperse\ phase, polymer}$  (see Eqn. (40)) for short contact time.

$$\frac{r_{disperse\ phase, liquid}}{r_{disperse\ phase, polymer}} = K\sqrt{\frac{D_{i, polymer}}{D_{i, liquid}}} \quad (40)$$

The ratio of  $r_{disperse\ phase, liquid}$  to  $r_{disperse\ phase, polymer}$  is 4.6E-08, i.e., the mean resistance is located in the polymer for short contact times.

### 3.3.2. Long Contact Times

For long contact times the mass transfer coefficients for the liquid phase can be defined as:

$$\beta = \frac{Sh D_{i, liquid}}{L} \quad (41)$$

while for the polymer Eqn. (39) is still valid, due to the comparably long scales of diffusion in the polymer (note, the characteristic time for diffusion in the polymer sheet is  $\tau_{\text{Diff}}=l_c^2/D_{i,\text{polymer}}$ , which is approximately 4 h for a 1 mm polymer sheet).

For this case the ratio of  $r_{\text{disperse phase, liquid}}$  to  $r_{\text{disperse phase, polymer}}$  is:

$$\frac{r_{\text{disperse phase, liquid}}}{r_{\text{disperse phase, polymer}}} = \frac{2 \cdot K \cdot L}{Sh} \sqrt{\frac{D_{i, \text{polymer}}}{D_{i, \text{liquid}}^2}} \sqrt{\frac{1}{\pi \cdot \Delta t}} \quad (42)$$

In this case, a ratio of  $r_{\text{disperse phase, liquid}}$  to  $r_{\text{disperse phase, polymer}}$  of 6.9E-11 is obtained for a contact time of 4 h. Hence, the mass transfer is controlled by the species transport in the polymer. Similar results are obtained for the combination of liquid and polymer.

### 3.3.3. Concentration Profile in the Polymer

The concentration profiles in the polymer depend on the Biot number for mass transfer (see Eqn. (43)). This dimensionless number describes the ratio of the inner mass transport resistance to the outer mass transport resistance.

$$Bi_m = \frac{\beta l_c}{K D_{i, \text{polymer}}} \quad (43)$$

For the problem under consideration, a Biot number of 1.7E10 is obtained. This means that there are extremely high gradients in the polymer and mass transfer is limited by the polymer phase only. The concentration at the interface is essentially zero because of the high mass transfer coefficient in the gas or liquid phase. The conclusion for the simulation is that diffusion in the polymer is much slower than the mass transfer from the interface to the fluid bulk. Thus, it is not necessary to couple diffusion in the polymer and fluid flow simulations. Instead, a constant mass transfer rate determined by the diffusion process in the polymer is sufficient to reconstruct the absorption and desorption process from polymers. Thus, the mass transfer rate is given by the time derivate of Eqn. (23), and local flow conditions do not impact the release of hydrogen peroxide from the polymer. The

only environmental variable that influences this process is the temperature via the temperature-dependent saturation concentration and diffusion coefficient.

### **3.4. Numerical Model**

Generally, by means of Computational Fluid Dynamics (CFD) the behaviour of a flowing continuous medium can be predicted by resolving the conservation equations for mass, momentum and, in case of thermal problems, enthalpy over a finite volume (FV) element [32]. In order to describe the desorption of hydrogen peroxide from the polymer, a species transport equation has to be integrated in the numerical solution as well.

#### **3.4.1. Continuity Equation**

The continuity equation states that the mass of a fluid is conserved. This fact is described for an unsteady, incompressible Newtonian fluid in Eqn. (44), where  $\rho$  and  $v$  represent the density and the velocity vector, respectively.

$$\frac{\partial \rho}{\partial t} = -\nabla(\rho v) \quad (44)$$

#### **3.4.2. Momentum Conservation Equation**

The velocity profile inside each cell of the numerical grid is calculated by means of the momentum conservation equation. Here the different terms describe the rate of change of momentum, the convective and diffusive flow, as well as the sources due to forces acting on the system, e.g. compressive force and gravity [31]. This momentum conservation equation can be written as follows:

$$\frac{\partial \rho v}{\partial t} = -\nabla(\rho v v) - \nabla \tau - \nabla p + \rho g \quad (45)$$

where  $p$ ,  $g$  and  $\tau$  refer to pressure, gravitational acceleration and stress tensor, respectively.

The stress tensor describes the turbulent fluid motion, which is directly calculated only for computational expensive methods like Discrete Numerical Simulation (DNS). For practical applications this term can be solved using simplifications and different model assumptions, e.g. RANS (Reynolds-Averaged Navier-Stokes) and LES (Large Eddy Simulation) methods.

In the RANS approach the unsteadiness of turbulence are averaged over time and only a mean flow is calculated [32]. To form a closure for these equations the realizable  $k$ - $\varepsilon$  model is used in this work. This model comprises two additional transport equations for the turbulent kinetic energy  $k$  and the dissipation energy  $\varepsilon$  in order to compute the Reynolds stress [31] (see Eqn. (46) and Eqn. (47)).

$$\frac{\partial \rho k}{\partial t} = -\nabla(\bar{v} \rho k) + \nabla\left(\frac{\mu_t}{\sigma_k} \nabla k\right) - \frac{\mu_t}{2} \left| \nabla \bar{v} + \nabla \bar{v}^T \right|^2 - \rho \varepsilon \quad (46)$$

$$\frac{\partial \rho \varepsilon}{\partial t} = -\nabla(\bar{v} \rho \varepsilon) + \nabla\left(\frac{\mu_t}{\sigma_\varepsilon} \nabla \varepsilon\right) - C_{\varepsilon 1} \frac{\varepsilon}{k} \frac{\mu_t}{2} \left| \nabla \bar{v} + \nabla \bar{v}^T \right|^2 - C_{\varepsilon 2} \rho \frac{\varepsilon^2}{k} \quad (47)$$

The turbulent viscosity  $\mu_t$  is defined as:

$$\mu_t = C_\mu \rho \frac{k^2}{\varepsilon} \quad (48)$$

where  $C_\mu$  is a constant, which is empirically accepted to be equal to 0.09. The values for the four constants  $\sigma_k$ ,  $\sigma_\varepsilon$ ,  $C_{\varepsilon 1}$  and  $C_{\varepsilon 2}$  are given in Table 3-8.

**Table 3-8 - Constants for the turbulence model.**

<i>Constant</i>	<i>Value [-]</i>
$\sigma_k$	1.00
$\sigma_\epsilon$	1.30
$C_{\epsilon 1}$	1.44
$C_{\epsilon 2}$	1.92

The Reynolds stresses can then be solved with the calculated turbulent viscosity using the Boussinesq relationship (see Eqn. (49)).

$$\tau_i = \mu_t [\nabla v + (\nabla v)^T] - \frac{2}{3} \rho k \delta \quad (49)$$

where  $\delta$  is the unit tensor called Kronecker symbol. Here, the turbulence is assumed to be isotropic, which means that the fluctuation components of the velocity are equal in the x, y, and z directions.

To solve the partial differential equations system, boundary conditions for k and  $\epsilon$  have to be set for the Inlet. These conditions are defined in Eqn. (50) and Eqn. (51).

$$k = \frac{3}{2} (I \cdot \bar{v})^2 \quad (50)$$

$$\epsilon = \frac{C_\mu^{0.75} k^{1.5}}{l} \quad (51)$$

The turbulent intensity I and the characteristic length l have to be estimated as well. For a fully developed flow in a duct or pipe, 5 % turbulent intensity and a characteristic length of the hydraulic diameter are normally used [33].

Furthermore, the velocity profiles need to be approximated in the near-wall region. This can be done by adopting a so-called wall function or by refining the mesh near the wall. In this work we used wall functions, which calculated the wall shear stress from the

assumption of a logarithmic velocity profile between the wall and the first computational node in the wall-normal direction.

In contrast to the RANS approach, Large Eddy Simulations (LES) approximates or models only the small scale fluctuations, while the Navier-Stokes equations are solved for large scale turbulent fluctuations. Which turbulent fluctuations are modelled or not, depends on different filters containing a defined length scale  $\Delta$  for the turbulent eddies. Operatively, only the eddies that are larger than  $\Delta$  are directly solved, while smaller eddies are approximated using the so-called subgrid-scale (SGS) models [32]. In this work, the Smagorinsky model is used as SGS-model.

### 3.4.3. Species Transport Equation

The species transport of  $H_2O_2$  can be written as follows:

$$\frac{\partial c}{\partial t} = -v\nabla c + \nabla(D\nabla c) \quad (52)$$

where  $c$  and  $D$  represent the dimensionless concentration and the turbulent diffusion coefficient, respectively [31].  $D$  is calculated by the use of the correlation of the Schmidt number (see Eqn. (53)).

$$D = \frac{v_t}{Sc_t} \quad (53)$$

Here,  $Sc_t$  denotes the turbulent Schmidt number. For our cases, this value is assumed to be 0.7 [5].

## 4. Simulation Setup

### 4.1. Test Chamber

A test chamber acted as a model for the CFD numerical simulation. This chamber has also been used for the experimental analysis of the adsorption behaviour of  $\text{H}_2\text{O}_2$  on different materials.

Four different mesh grid refinements of this chamber were generated by the commercial meshing program “Cubit”, using a grid refinement ratio  $r$  of 1.3 between subsequent meshes. Figure 4-1 presents the four different mesh sizes sorted from the coarsest to the finest one.

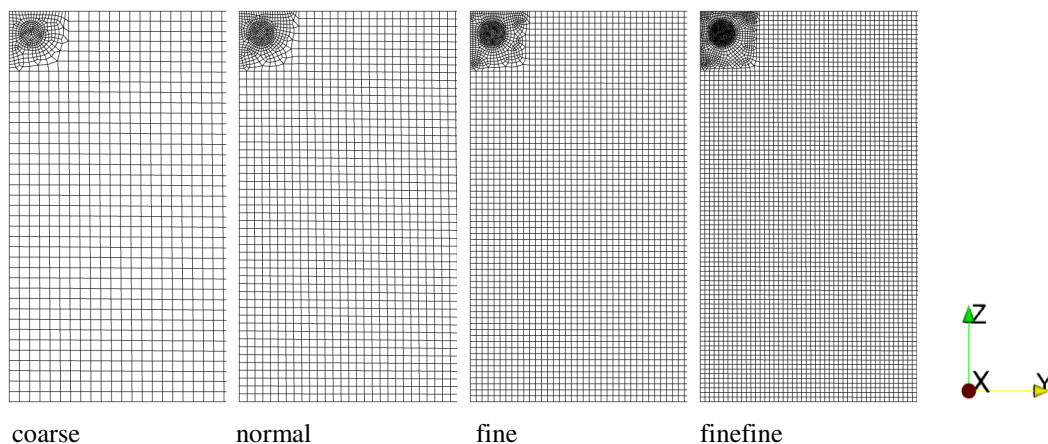


**Figure 4-1 - Different grid refinements of the test chamber.**

The dimensions of the chamber were  $0.496 \times 0.496 \times 0.496 \text{ m}^3$ . Four patches, i.e. boundary faces, were defined as follows: wall, inletOutlet1 (inlet), inletOutlet2 (outlet) and polymer (see Figure 4-2).

The exactly defined bonds of the four different patches are shown in Table 4-1. To solve the transport equation, boundary conditions and initial conditions have to be set for all four patches before starting the simulation.

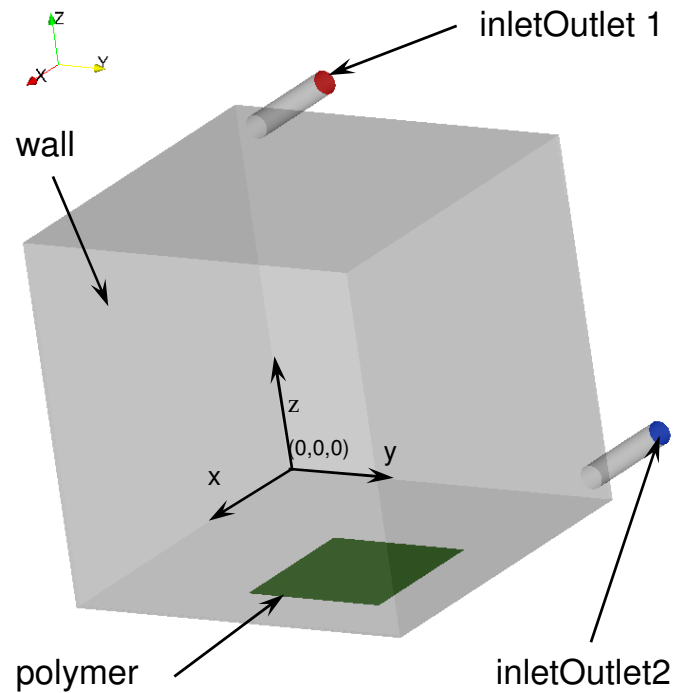


Figure 4-2 - Sketch of the test chamber.

Table 4-1 - Bonds for the four different patches.

<i>patches</i>	<i>X range [m]</i>	<i>Y range [m]</i>	<i>Z range [m]</i>
wall (grey)	-0.160 – 0.496	0.000 – 0.496	0.000 – 0.496
inletOutlet1 (red)	-0.160 – -0.160	0.012 – 0.044	0.452 – 0.484
inletOutlet2 (blue)	-0.160 – -0.160	0.452 – 0.484	0.012 – 0.044
polymer (green)	0.200 – 0.400	0.200 – 0.400	0.000 – 0.000

## 4.2. Simulation Settings

In this work, the flow profile and the species transport of  $H_2O_2$  were examined by the use of Computational Fluid Dynamics (CFD). Here, two different CFD programs, namely OpenFoam and AVL Fire, were tested.

In general, four different mesh resolutions (coarse, normal, fine, finefine) of a test chamber were used. Figure 4-3 illustrates all simulations using the program OpenFoam. In this case the flow profile was solved by the Reynolds-Averaged Navier-Stokes simulation (RANS). The desorption from polymer was then carried out by Large Eddy Simulation (LES). To compare the results for the species transport, one simulation using the frozen

velocity field of the normal mesh was realized. Finally, RANS was tested with three different turbulent kinetic energies and the normal mesh.

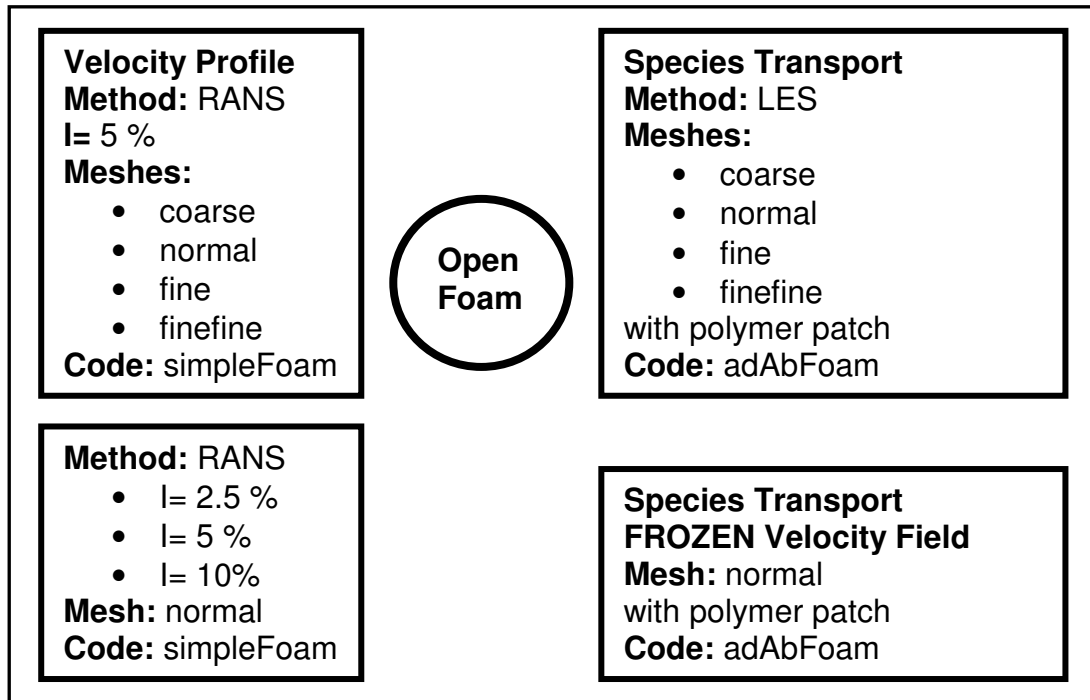
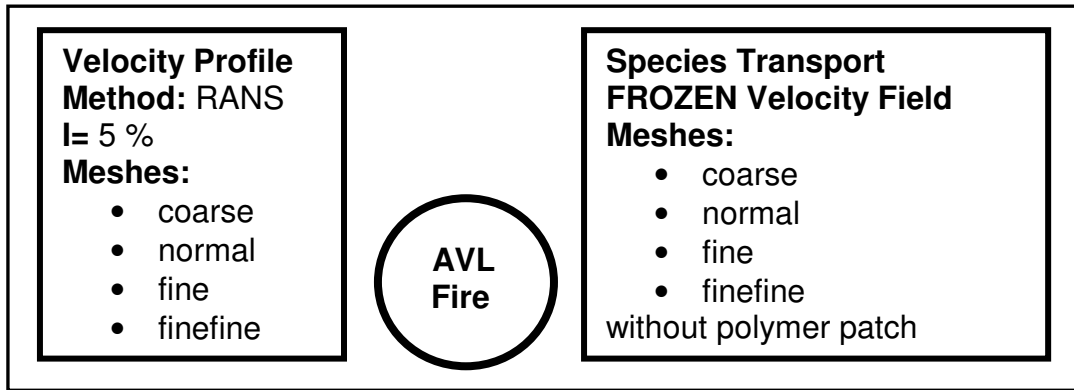


Figure 4-3 - All Simulations using OpenFoam.

To compare the results of the open source CFD package OpenFoam with AVL Fire, the flow profiles in all four meshes were computed with the RANS approach. Furthermore, the distribution of H<sub>2</sub>O<sub>2</sub> injected into the chamber was simulated with a steady-state solver using the previously calculated RANS velocity profiles for different mesh resolutions (see Figure 4-4).

For all simulations the velocity was set to 5 m/s at the Inlet. In OpenFoam the RANS was calculated with the “simpleFoam” algorithm using the realizable k-ε turbulence model. For all simulations with species transport a new algorithm “adAbFoam” (see Appendix 9.5) was developed in OpenFoam.



**Figure 4-4 - All Simulations using AVL Fire.**

For AVL Fire the  $k$ - $\epsilon$  turbulence model was used as well, leaving all other settings to the standard initialization. The exact values for turbulent kinetic energy and epsilon are presented in Table 4-2.

**Table 4-2 -  $k$  and  $\epsilon$  for different turbulent intensities.**

<i>turbulence intensity</i> $I$ [%]	<i>turbulent kinetic energy</i> $k$ [ $m^2 s^{-2}$ ]	<i>epsilon</i> $\epsilon$ [ $m^2 s^{-3}$ ]
2.5	0.023	0.018
5	0.093	0.147
10	0.375	1.179

## 5. Experimental Method

### 5.1. Absorption and Desorption in Polymers

#### 5.1.1. Experimental Setup

The absorption and desorption processes of  $\text{H}_2\text{O}_2$  in polymers were analyzed using two different experimental setups. In the first setup a polymer foil, with a defined area, was cut into flakes [2×2 cm]. In the second setup the foil was cut into equal stripes [~ 4 cm], which were attached to a simple stirrer. The thicknesses of the polymer foils were determined using a micrometer screw.

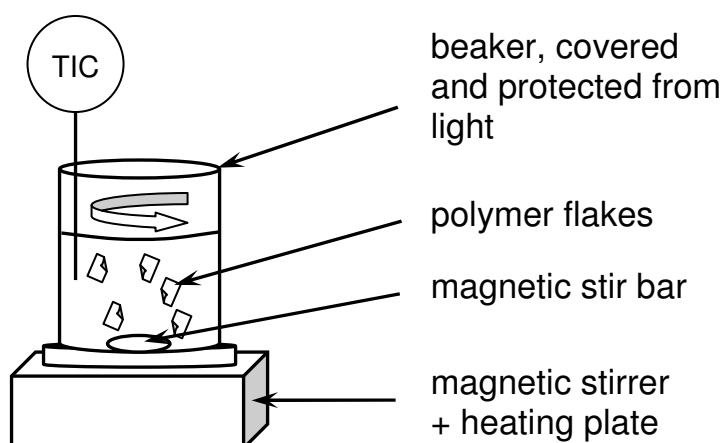


**Figure 5-1 - Sketch of the experimental setup 1 for absorption and desorption experiments involving polymer flakes.**

Figure 5-1 shows a sketch of the first experimental setup for  $\text{H}_2\text{O}_2$  absorption and desorption involving flakes. Therefore, a 600 ml beaker, protected from light with aluminium foil, was used. To guarantee a constant temperature and stirring rate, a magnetic stirrer with an integrated heating plate and temperature control was used. The beaker was covered in order to avoid decontamination of  $\text{H}_2\text{O}_2$  and to protect the content from light.

The second experimental setup (see Figure 5-2) consisted of a simple stirrer, onto which polymer stripes were attached. The stirrer was coupled to a stirrer drive assembly in a covered 600 ml beaker, protected from light with aluminium foil. A magnetic stirrer with an integrated heating plate and temperature control was used.

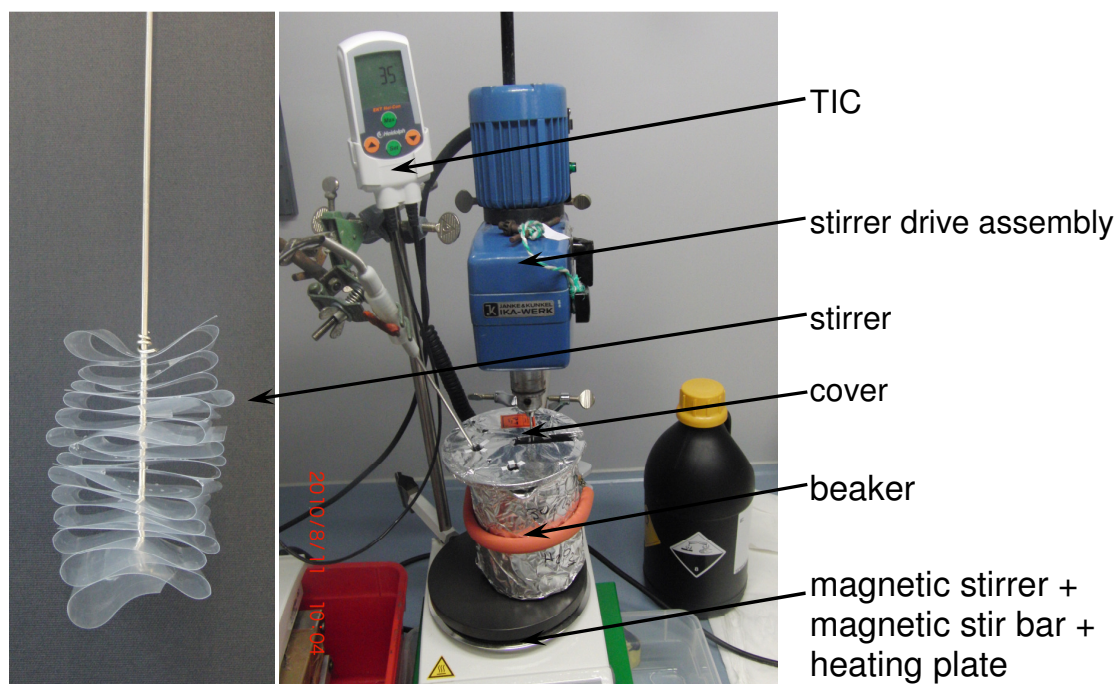


**Figure 5-2 - Experimental setup 2 for absorption and desorption experiments involving polymer stripes.**

### 5.1.2. Absorption Procedure

The foils were cleaned before starting the absorption procedure. Thus, the flakes were put into a beaker with deionized water and stirred for one minute. The solution with the polymer flakes was poured through a colander. The stripes were stirred in deionized water for 30 seconds. Both cleaning procedures were repeated three times.

The flakes and stripes were placed in a covered 600 ml beaker, protected from light with aluminium foil.  $2 \times 500$  ml of 30 % (w/w)  $\text{H}_2\text{O}_2$  were heated to a defined temperature (see Chapter 5.1.6), and the solution was slowly poured into each beaker and a sample of the 30 % (w/w)  $\text{H}_2\text{O}_2$  solution was taken to determine the initial  $\text{H}_2\text{O}_2$  concentration. To quantify a possible decomposition of  $\text{H}_2\text{O}_2$  during the experiment, the concentration of the 30 % (w/w)  $\text{H}_2\text{O}_2$  solution was monitored using a UV/VIS- Spectrophotometer (Perkin

Elmer, Lambda 35) after predefined time intervals. After the experiment the polymer foils were stored in a covered beaker, protected from light with aluminium foil.

### 5.1.3. Measurement Procedure for the 30 % (w/w) H<sub>2</sub>O<sub>2</sub> Solution

H<sub>2</sub>O<sub>2</sub> absorbs ultraviolet light in a range of 200 to 400 nm (see *Phibbs et al.* [34]). A calibration curve was made using a UV/VIS- Spectrophotometer (Perkin Elmer, Lambda 35) to determine the concentration of H<sub>2</sub>O<sub>2</sub> during the absorption procedure. A 30 % (w/w) H<sub>2</sub>O<sub>2</sub> solution was diluted with deionized water and EDTA (50 mg/L) to get 10 different concentrations (0.125 M, 0.25 M, 0.5M, 1.0 M, 1.85 M, 2.036 M, 2.24 M, 2.8 M, 3.2 M and 3.5 M). The additive EDTA stabilizes H<sub>2</sub>O<sub>2</sub> in deionized water by inhibiting its decomposition.

First, the absorption coefficients at different concentrations were measured at wavelengths of 310, 320, 330 and 340 nm. With a maximal absorption of 0.23 the calibration curve at 340 nm turned out to be appropriate in this molar range of dilutions. By repeating the calibration procedure six times, a linear calibration curve was generated at a wavelength of 340 nm (see Appendix, Chapter 9.2).

To obtain the correct concentration for the subsequent measurements, 200 µL of sample and 1400 µL of deionized water with EDTA [50 mg/L] were mixed. The samples were protected from light during handling. After 15 min the samples were analyzed by measuring the absorption at 340 nm. The concentration of each data point was calculated using linear regression (see Chapter 9.2).

Figure 5-3 shows the weight percentage profile over time of the 30 % (w/w) H<sub>2</sub>O<sub>2</sub> solution during the third absorption procedure of H<sub>2</sub>O<sub>2</sub> and polypropylene at 30°C. The weight percentage profiles during the absorption process with different polymers showed similar trends, i.e., no decomposition of H<sub>2</sub>O<sub>2</sub> occurred.

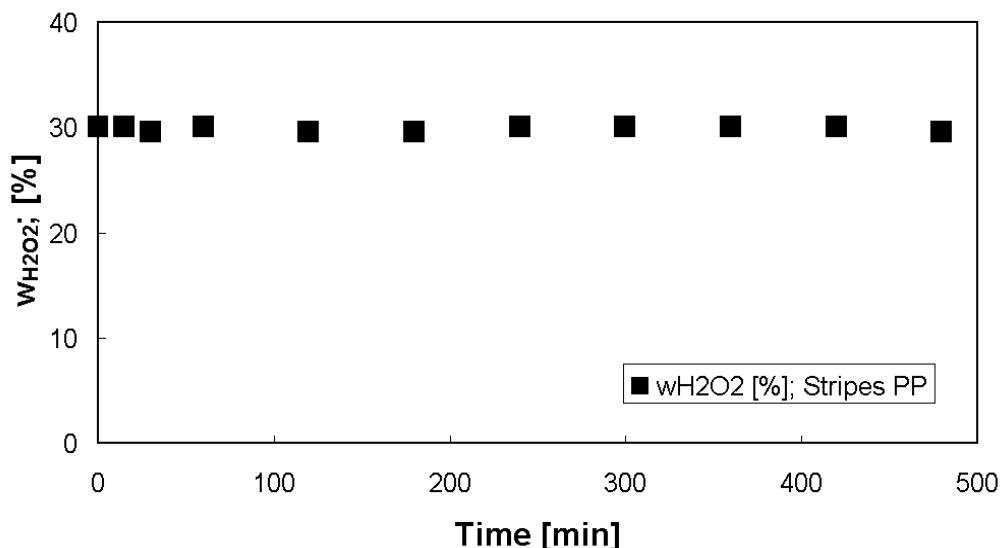


Figure 5-3 - Weight percentage of the H<sub>2</sub>O<sub>2</sub> solution during the absorption procedure (H<sub>2</sub>O<sub>2</sub> and polypropylene at 303.15 K).

#### 5.1.4. Desorption Procedure

Before the desorption procedure was done, the polymer surface was cleaned to remove adsorbed H<sub>2</sub>O<sub>2</sub>. This was done by performing the cleaning procedure described in 5.1.2 three times.

The flakes and stripes were again placed in a covered 600 mL beaker and protected from light with aluminium foil. After reaching the predefined temperature, 500 mL of deionized water with EDTA [50 mg/L] were poured into the beaker. A sample of 1 mL was taken and transferred into a 1.5 mL glass vial to define the initial concentration of H<sub>2</sub>O<sub>2</sub>. During desorption, samples of 1 mL were taken at defined time steps and stored in the fridge. These samples were analyzed using the Amplex® Red Hydrogen/ Peroxidase Assay Kit (Invitrogen [35]) to quantify the H<sub>2</sub>O<sub>2</sub> concentration.

#### 5.1.5. Amplex® Red Hydrogen/ Peroxidase Assay Kit

Amplex® Red reagent (10-acetyl-3,7-dihydroxyphenoxazine) reacts with hydrogen peroxide H<sub>2</sub>O<sub>2</sub> in the presence of horseradish peroxidase (HRP) in a stoichiometric ratio of 1:1 and forms the fluorescent resorufin (Zhou *et al.* [36]) the reaction equation is

illustrated in Figure 5-4 ). The absorption coefficient of resorufin was measured at 571 nm using a UV/VIS- Spectrophotometer (Perkin Elmer, Lambda 35).

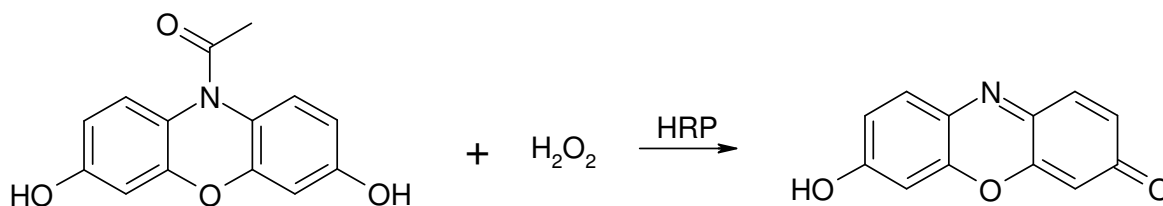


**Figure 5-4 - Oxidation of Amplex® Red reagent to resorufin [37].**

For the calibration curve a linear fit of the absorption coefficient over the H<sub>2</sub>O<sub>2</sub> concentration was generated at a wavelength of 571 nm. Thus, a calibration H<sub>2</sub>O<sub>2</sub> solution (~ 3 % (w/w)) was diluted with 1X reaction buffer (4 ml of 0.25 M sodium phosphate and 16 mL deionized water). Eight samples having different concentrations were prepared (0.50 μM, 1.00 μM, 1.25 μM, 2.00 μM, 2.50 μM, 4 μM, 5 μM, and 10 μM). For the blank 1X reaction buffer was used.

The Amplex® Red reagent was dissolved in 60 μL of DMSO (10 mM) and HRP was dissolved in 1.0 mL of 1X reaction buffer (10 U/mL). 50 μL of 10 mM Amplex® Red reagent stock solution, 100 μL of 10 U/mL HRP stock solution and 4.85 mL of 1X reaction buffer were mixed together to form a working solution.

For the determination of the calibration curve 50 μL of the working solution and 50 μL of the sample were added into a 1.5 mL plastic microtube. After 30 minutes of incubation time under light protection the absorption was measured at 571 nm at room temperature.

The samples from the desorption experiment were diluted with deionized water containing EDTA [50 mg/L]. To get the right dilution factor, the last sample drawn was analyzed with five different dilution factors. For incubation nine samples of 50 μL were grouped in one set to allow ten minutes handling time for each of these sets. Absorption was measured at 571 nm. The concentrations of the samples were then determined using the calibration curve.

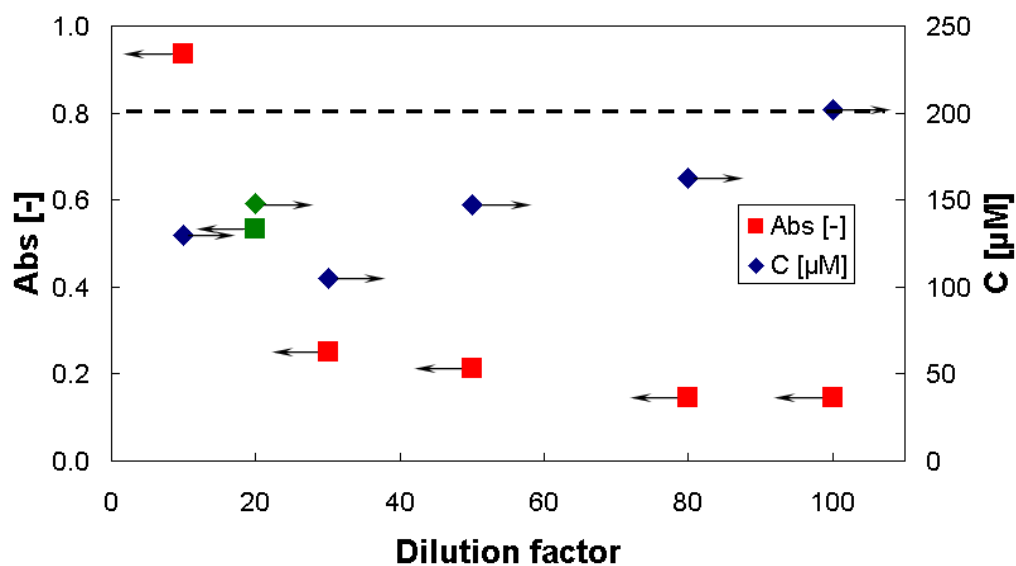


Figure 5-5 - Absorption and concentration of  $\text{H}_2\text{O}_2$  for different dilutions of the last sample (LDPE, second run).

Figure 5-5 shows the measured values of the absorption (red) and the calculated concentrations (blue) of  $\text{H}_2\text{O}_2$  of the desorption experiments involving LDPE samples (180 min).

Two important selection rules were utilized. On the one hand the dilution factor should be as low as possible to avoid errors due to dilution, and on the other hand the absorption should be in the linear range of the calibration curve. Thus, the maximal absorption value should be below 0.8. For this experiment a dilution factor of 1:20 was used in order to fulfill both criteria.

### 5.1.6. Materials and Experimental Conditions

In this work the absorption and desorption of  $\text{H}_2\text{O}_2$  in three different polymers, namely polypropylene (PP), low-density polyethylene (LDPE), polyvinylchloride (PVC) and in glass were studied. A summary of all experimental conditions is given in Table 5-1.

Two runs of absorption and desorption of  $\text{H}_2\text{O}_2$  from each material were experimentally investigated at 35°C. Absorption and desorption experiments of  $\text{H}_2\text{O}_2$  from polypropylene were also carried out at 25°C and 30°C to provide insight into the temperature dependency of the saturation concentration and the diffusion coefficient.

**Table 5-1 - Experimental conditions for absorption and desorption experiments involving different polymers.**

<i>Polymer</i>	<i>Run</i>	<i>Setup</i>	<i>A</i> [cm <sup>2</sup> ]	<i>Thickness</i> [mm]	<i>T</i> [K]	<i>V</i> <sub>30% H<sub>2</sub>O<sub>2</sub></sub> [mL]	<i>V</i> <sub>dist. H<sub>2</sub>O/EDTA</sub> [mL]
<b>PP</b>	1	Flakes	649.7	0.09	298.15	500	500
	2	Stripes	649.7	0.09	298.15	500	500
	3	Stripes	646.6	0.09	303.15	500	500
	4	Stripes	640.2	0.09	308.15	500	500
	5	Stripes	640.2	0.09	308.15	500	500
<b>LDPE</b>	1	Stripes	640.0	0.25	308.15	500	500
	2	Stripes	256.0	0.25	308.15	500	500
<b>PVC</b>	1	Stripes	640.0	0.20	308.15	500	500
	2	Stripes	128.0	0.20	308.15	500	500
<b>glass</b>	1	Stripes	59.3	1.00	308.15	600	600

Due to a lack of information about the saturation concentration of H<sub>2</sub>O<sub>2</sub> in these materials, an area of 640 cm<sup>2</sup> of each polymer was analyzed for the first run.

The area of the polymer in the second run was determined based on the optimal dilution factor, which was needed for the Amplex® Red Hydrogen/ Peroxidase Assay Kit (see Chapter 5.1.5).

## **5.2. Fast Detection of H<sub>2</sub>O<sub>2</sub> in Polymers using NIR**

To analyze the surface of the polymer, infrared spectra were recorded via a HELIOS camera system (EVK DI Kerschhaggl GmbH, Austria). This instrument has an integrated halogen lamp as IR source. The reflectance of IR light from the polymer's surface is measured using an InGaAs sensor chip, which is sensitive for infrared light. This sensor offers 240 spatial × 316 spectral pixels, which leads to 240 individual spectra (spatially arranged along a line) made up by 316 spectral intensities. The IR range is limited from 1050 to 1670 nm.

100 images of each 16 cm<sup>2</sup> PVC foil (for material data see Chapter 9.4.2) were taken by HELIOS. Out of these spectra 40 mean average spectra were calculated. The reflectance was transformed into a so called pseudo-absorbance using "The Unscrambler" (Camo,

Norway). These data were analyzed by Multivariate Data Analysis (MVDA) based on principle component analysis (PCA). PCA reduces the spectral data by the largest variance present in the data set [38]. Untreated PVC foils were compared with ones after the absorption in 30 % (w/w) H<sub>2</sub>O<sub>2</sub> solution. This procedure was repeated twice.

## 6. Results

### 6.1. Experiments

#### 6.1.1. Differences between Stripes and Flakes

First, the results of the experiment involving stripes and flakes were compared. Therefore polypropylen foils (transparent sheet; brand: Libroline; A4; quantity: 10) were used (experimental conditions are mentioned in Table 5-1).

Samples were analyzed after 0, 0.5, 5, 10, 15, 20, 30, 40, 60, 100, 150, 210, 300, 420 and 540 min, with three different dilutions (1:4; 1:8, 1:16).

The desorption curves of flakes and stripes are shown in Figure 6-1 (the samples after 60 and 100 min of the stripes were not analyzed, and were interpolated linearly).

The results for the diffusion coefficient and the saturation concentration for stripes and flakes are mentioned in Table 6-1.

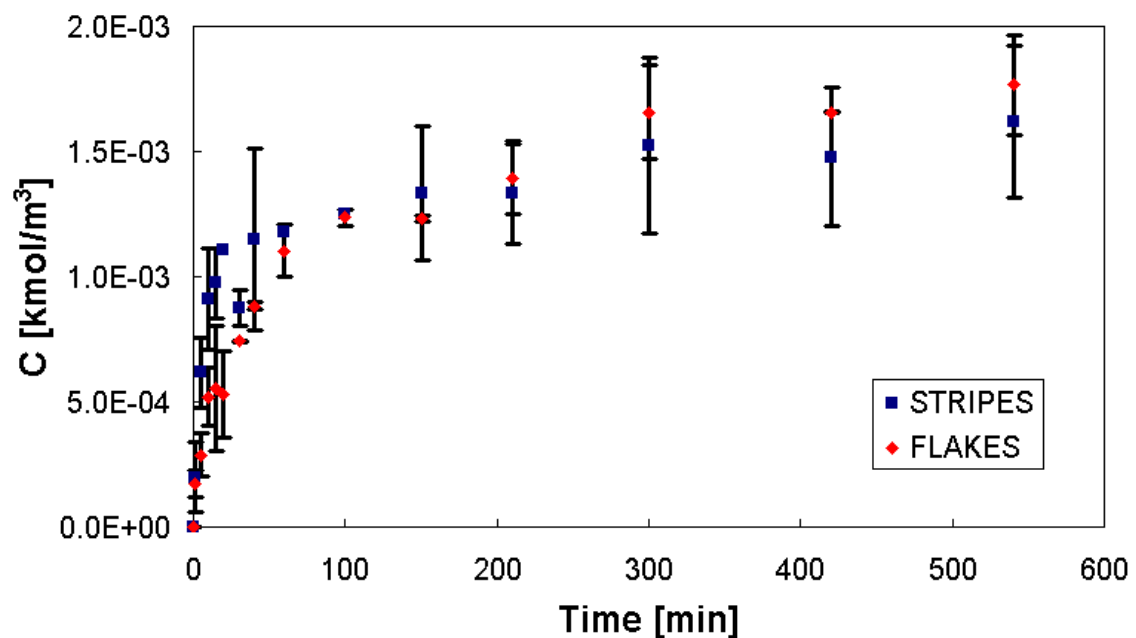


Figure 6-1 - Arithmetic mean of amount of  $\text{H}_2\text{O}_2$  and standard deviation for all dilutions (1:4, 1:8, 1:16; experiments involving PP stripes and flakes).

Although the experimental procedure with the enzyme kit was exactly the same for both cases, the stripes setup has an extremely high standard deviation compared to the flakes setup. To avoid errors due to sample dilution, a low dilution should be used. Thus, the results of the 1:16 dilution were not used for the subsequent analysis.

Compared to the flakes' average diffusion coefficient of  $1.92\text{E-}09 \text{ cm}^2/\text{s}$ , the steep increase of the desorbed amount of  $\text{H}_2\text{O}_2$  in the experiments involving stripes leads to a higher diffusion coefficient of  $6.05\text{E-}09 \text{ cm}^2/\text{s}$ . The reason for this could be the controlled motion of the stripes using a stirrer leading to a higher mass transfer in liquid. In contrast, the flakes tended to stick together, leading to reduced mass transfer. Because of these results the stripes setup was used for further experiments to guarantee identical experimental conditions during absorption and desorption, as well as no limitations due to mass transfer on the liquid side.

The mean saturation concentration of stripes ( $1.56\text{E-}03 \text{ kmol/m}^3$ ) differs only by a factor of 0.96 from the flakes ( $1.63\text{E-}03 \text{ kmol/m}^3$ ).

**Table 6-1 - Results for the diffusion coefficient and saturation concentration of  $\text{H}_2\text{O}_2$  from PP stripes and flakes in dist.  $\text{H}_2\text{O}_2$  with EDTA [50 mg/L] at 303.15 K.**

<i>PP</i>	$D_{Stripes}$ [ $\text{cm}^2 \text{ s}^{-1}$ ]	$D_{Flakes}$ [ $\text{cm}^2 \text{ s}^{-1}$ ]	$C_{\text{H}_2\text{O}_2;Stripes}^{sat}$ [ $\text{kmol m}^{-3}$ ]	$C_{\text{H}_2\text{O}_2;Flakes}^{sat}$ [ $\text{kmol m}^{-3}$ ]
Dilution 1:4	5.50E-09	1.89E-09	1.37E-03	1.59E-03
Dilution 1:8	6.60E-09	1.95E-09	1.75E-03	1.66E-03

### 6.1.2. Polypropylen (PP)

Transparent sheets (brand: Libroline; A4; quantity: 10) were used as an example for polypropylene. Experimental conditions are mentioned in Table 5-1.

The experiment was done five times. The first two experimental runs comprised the stripes and the flakes setup mentioned in 6.1.1 at 25°C. The third experiment was done using the stripes setup at 30°C. The fourth experiment was performed at 35°C, while the fifth experiment acted as a verification measurement for the saturation concentration at 35°C. The last two experiments were terminated after 300 min and, in addition to the other experiments, samples were also analysed at 1, 1.5, 2, 2.5, 3, 3.5, 4, 80, 120, 180,

240 and 270 min. The amounts of  $\text{H}_2\text{O}_2$  desorbed from PP at 25°C, 30°C and 35°C using the stripes setup are shown in Figure 6-2.

As expected, the experiments verified that the saturation concentration increases with rising temperature. The diffusion coefficient was also increasing in the case of the desorption measurement at 25°C and 35°C. However, the highest diffusion coefficient was achieved in the desorption experiment at 30°C. One reason for this could be that insufficient samples were taken at the beginning of the experiment at 30°C to describe the steep slope. Another reason could be a different texture of the polymer foil due to fabrication. Because of this inconsistency, the diffusion coefficient at 30°C was not taken into account in further work.

The repetition of the experiment at 35°C confirmed the saturation concentration measured in experiment no. 4, see the error bars in Figure 6-2.

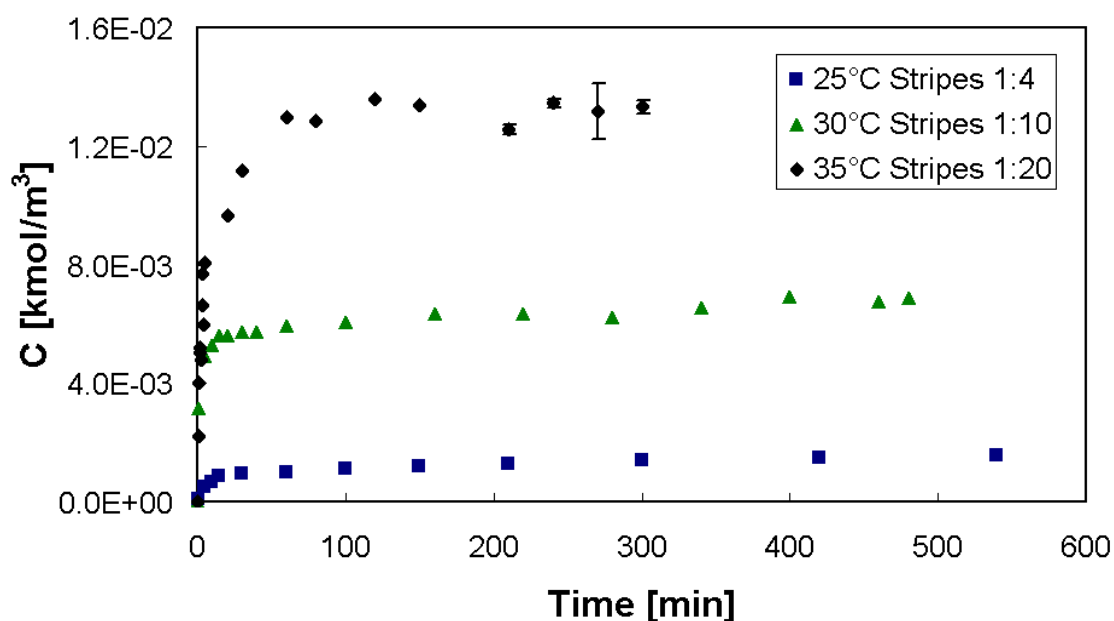


Figure 6-2 - Desorbed amount of  $\text{H}_2\text{O}_2$  from polypropylene at 298.15 K, 303.15 K and 308.15 K.

The diffusion coefficients and saturation concentrations at 25°C, 30°C and 35°C are detailed in Table 6-2.

**Table 6-2 - Results for the diffusion coefficient and saturation concentration of H<sub>2</sub>O<sub>2</sub> in PP at different temperatures.**

<i>Experiment</i>	<i>T</i> [K]	<i>D</i> [cm <sup>2</sup> s <sup>-1</sup> ]	<i>C</i> <sub>H<sub>2</sub>O<sub>2</sub></sub> <sup>sat</sup> [kmol m <sup>-3</sup> ]
1st run PP Stripes	298.15	5.50E-09	1.37E-03
2nd run PP Stripes	303.15	-	6.06E-03
3rd run PP Stripes	308.15	2.00E-08	1.27E-02

### 6.1.3. Low-Density Polyethylene (LDPE), Polyvinylchloride (PVC) and Glass

Furthermore, the absorption and desorption characteristics of H<sub>2</sub>O<sub>2</sub> in low-density polyethylene, polyvinylchloride and glass were determined (see Appendix 9.4.1, 9.4.2 and 9.4.3 for details).

Because of the too high dilution factors for the first run, the diffusion coefficients and saturation concentrations for LDPE and PP were taken from the calculations of the second run using the optimal dilution of the samples. Figure 6-3 and Figure 6-4 illustrated the desorbed amount of H<sub>2</sub>O<sub>2</sub> from LDPE and PP. The absorption and desorption experiment of H<sub>2</sub>O<sub>2</sub> from glass verified that no absorption of H<sub>2</sub>O<sub>2</sub> in glass occurred. The results of diffusion coefficients and saturation concentrations of LDPE, PP and glass are summarized in Table 6-3.

**Table 6-3 - Results for the diffusion coefficient and the saturation concentration of H<sub>2</sub>O<sub>2</sub> in LDPE, PVC and glass at 308.15 K.**

<i>Experiment</i>	<i>D</i> [cm <sup>2</sup> s <sup>-1</sup> ]	<i>C</i> <sub>H<sub>2</sub>O<sub>2</sub></sub> <sup>sat</sup> [kmol m <sup>-3</sup> ]
2nd run LDPE Stripes	4.90E-08	7.88E-03
2nd run PVC Stripes	1.10E-08	8.61E-02
1st run Glass	0.0	0.0

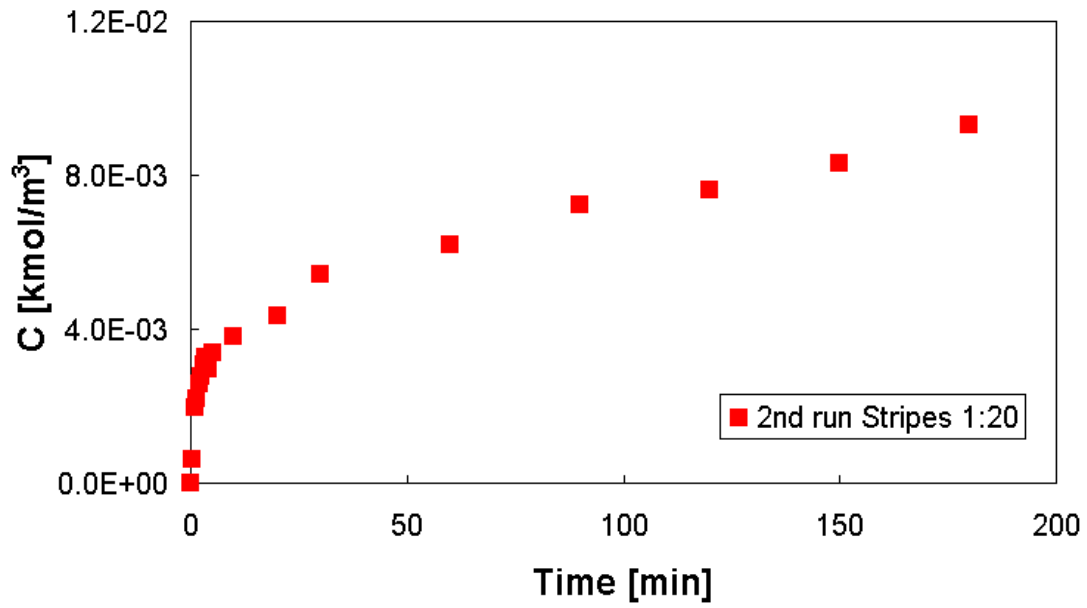


Figure 6-3 - Desorbed amount of H<sub>2</sub>O<sub>2</sub> from low-density polyethylene at 308.15 K (second run).

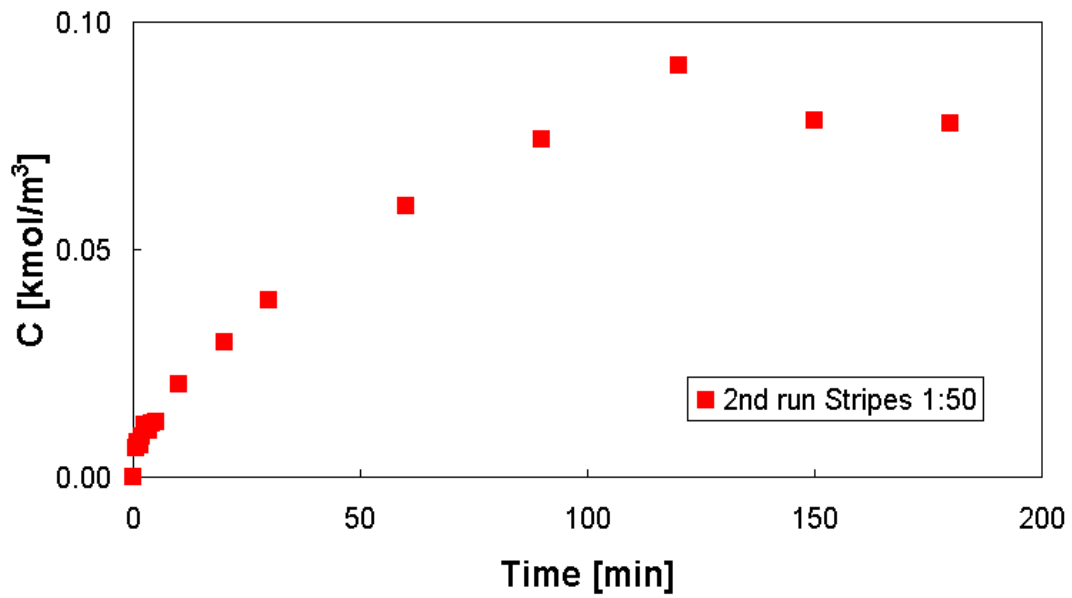


Figure 6-4 - Desorbed amount of H<sub>2</sub>O<sub>2</sub> from polyvinylchloride at 308.15 K (second run).

#### 6.1.4. Detection of H<sub>2</sub>O<sub>2</sub> in Polymers using NIR

The results of the surface imaging by a HELIOS camera system are quantified via score-plots. Therefore, 40 individual spectra per sample were projected onto the first selected principle components (PC1, PC2).

Figure 6-5 shows the results of comparing untreated PVC foils (blue 0.000) with saturated ones using 30 % (w/w) H<sub>2</sub>O<sub>2</sub> solution (red 30.00). The characteristic pattern of the plot divides both analyzed samples into separate groups. This effect verifies definitely that a qualitative difference between untreated and saturated PVC foil was detected by this NIR method.

The output of the second experiment is presented in Figure 6-6. Here, saturated PVC foil (blue 1.000 and red 2.000) and untreated PVC foil (green 3.000) were scanned again. In this case no difference between the three samples was detected by NIR. This circumstance is demonstrated by 40 group formations where each group consists of all three samples (i.e., red, blue and green dots) and therefore no separation occurs.

Thus, it was impossible to reproduce the shift in the spectra shown in Figure 6-5.

An explanation for this phenomenon could be the pre-treatment. The first samples illustrated in Figure 6-5 were analyzed directly after the experiment. Therefore no storage of samples was needed and desorption of H<sub>2</sub>O<sub>2</sub> from polymer can be excluded.

Another explanation is that the NIR method using the HELIOS camera system verified only the adsorbed H<sub>2</sub>O<sub>2</sub>.

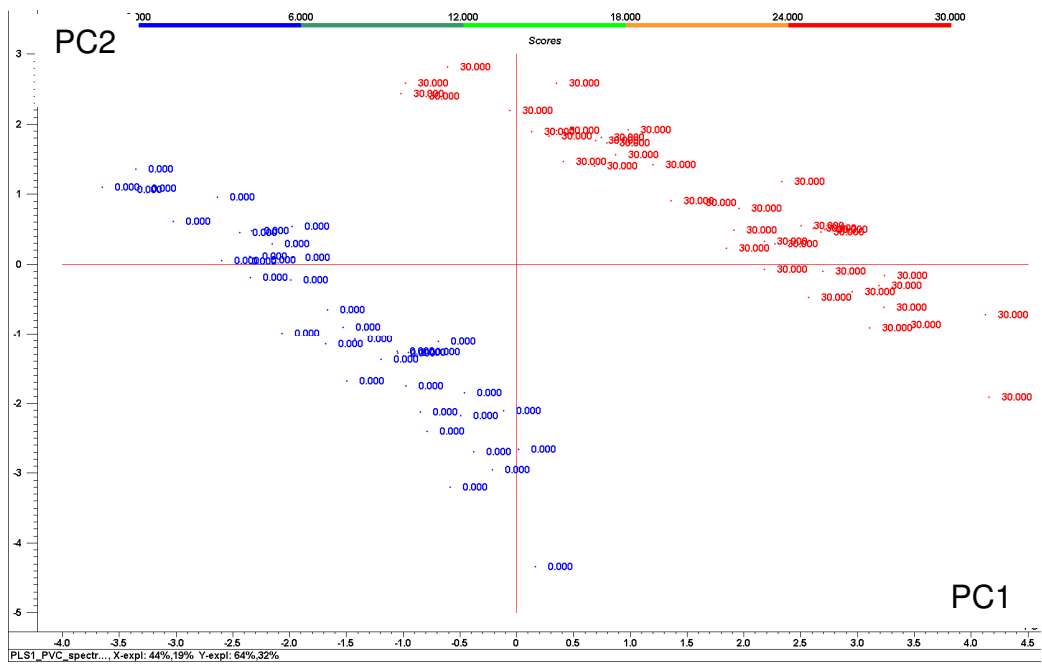


Figure 6-5 - Score plot of an untreated (blue 0.000) and a saturated PVC foil (red 30.00), directly after saturation.

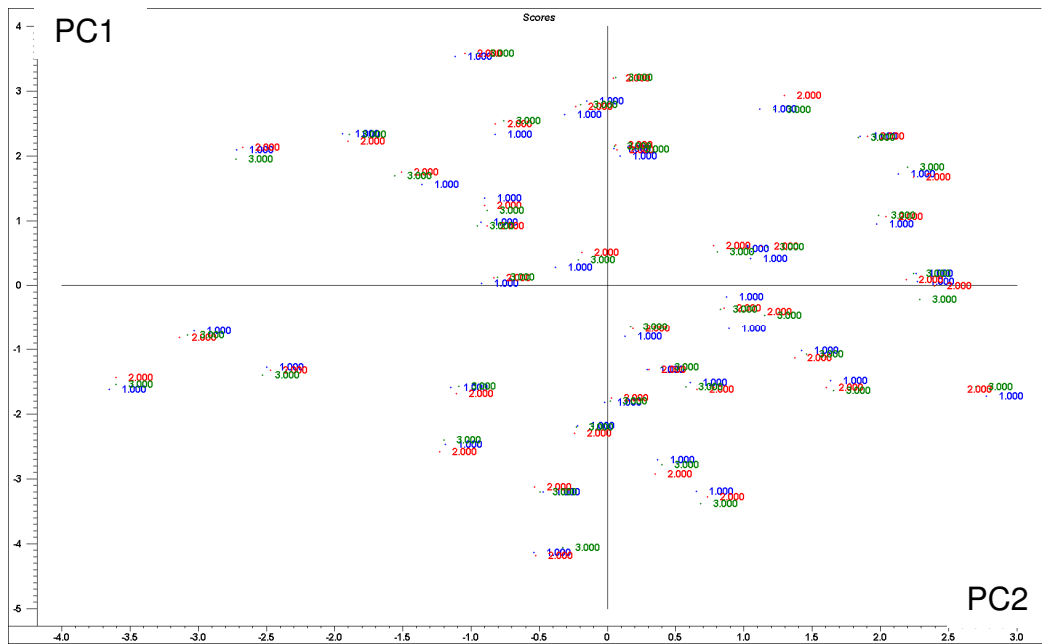


Figure 6-6 - Score plot of two saturated PVC foils (blue 1.000 and red 2.000, cleaned) and an untreated PVC foil (green 3.000).

## 6.2. Simulations

### 6.2.1. Flow Profile in the Test Chamber

The flow profile in the test chamber was calculated for the four mesh sizes with the settings described in Chapter 4. In these four simulations a gas flow of 5 m/s was injected horizontally through the inletOutlet1 (see Figure 4-2). The results of the flow profile in the test chamber for the normal mesh are illustrated in Figure 6-7 and in Figure 6-8, both using AVL Fire and accordingly OpenFoam. Due to the low velocity in the chamber, the chart presenting the velocity of both figures was normalized from 0 to 1.

Both simulation programs apparently present a similar profile. In order to compare the results of the flow profile of OpenFoam and AVL Fire the velocity was sampled along two lines in the chamber.

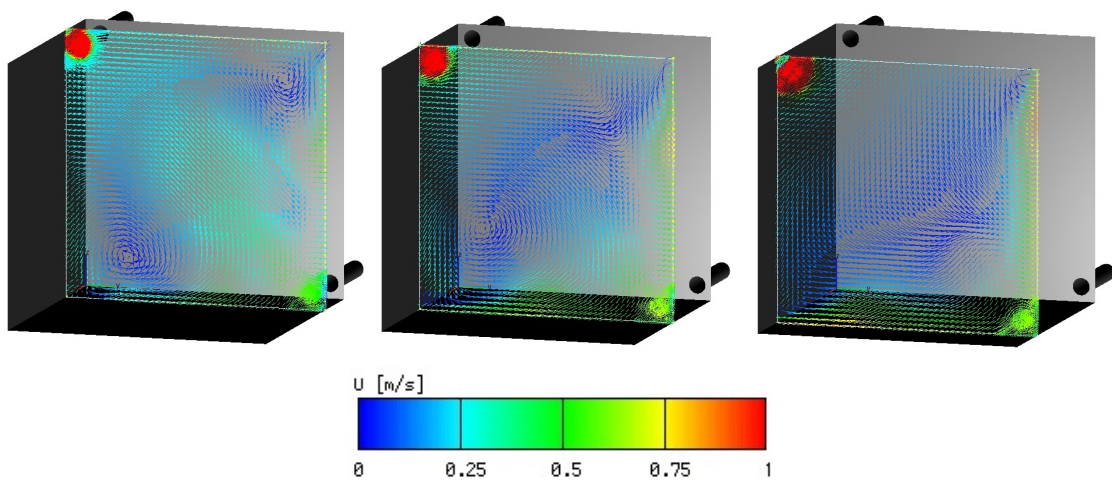
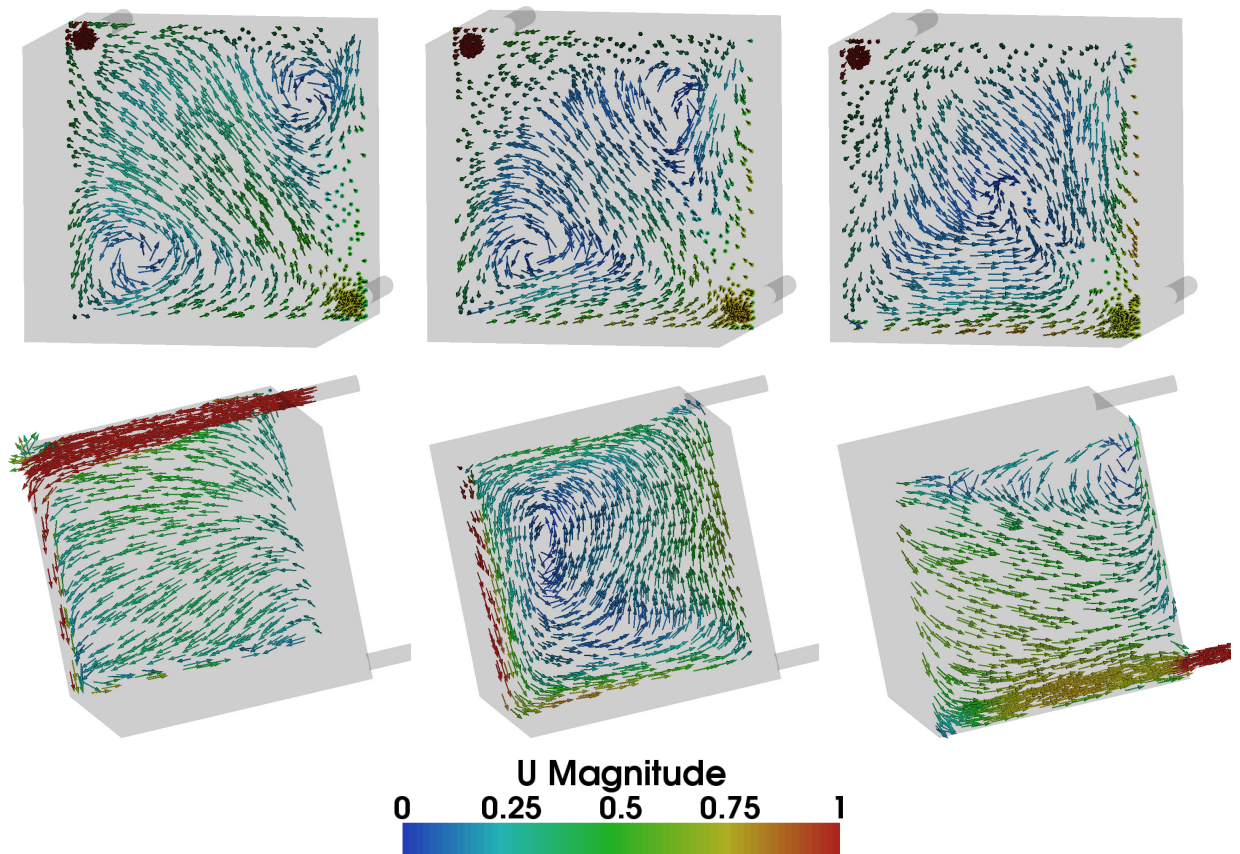


Figure 6-7 - Vector fields of  $U$  [m/s] in the test chamber (normal mesh) using AVL Fire.



**Figure 6-8 - Vector fields of U [m/s] in the test chamber (normal mesh) using OpenFoam.**

Because of the geometry of the chamber and the positions of the Inlet and Outlet pipes, two vortices at the bottom right and at the top left are formed. These two vortices begin to dissolve when going closer to the approached wall. With an inlet stream of 5 m/s the velocity in the chamber ranges from zero up to 0.75 m/s. The decreasing velocity can be explained by the higher volume of the chamber compared to the duct inlet. As with the Inlet diameter of 0.032 m a volumetric flow rate of  $4.02\text{E-}03 \text{ m}^3/\text{s}$  is reached. 30 s are needed to once purge the volume of the chamber.

Concerning the post-processing of the numerical data, the velocity [m/s] is sampled along the x line (-0.160 to 0.496 m) from the midpoint of the Inlet or the Outlet of the four different mesh sizes. On the one hand a statement of the accuracy of the different mesh sizes can be made and on the other hand the results of both programs can be compared.

The velocity data sampled along the Inlet line using the programs OpenFoam and AVL Fire are illustrated in Figure 6-9 and Figure 6-10, while the same results along the Outlet line are presented in Figure 6-11 and Figure 6-12.

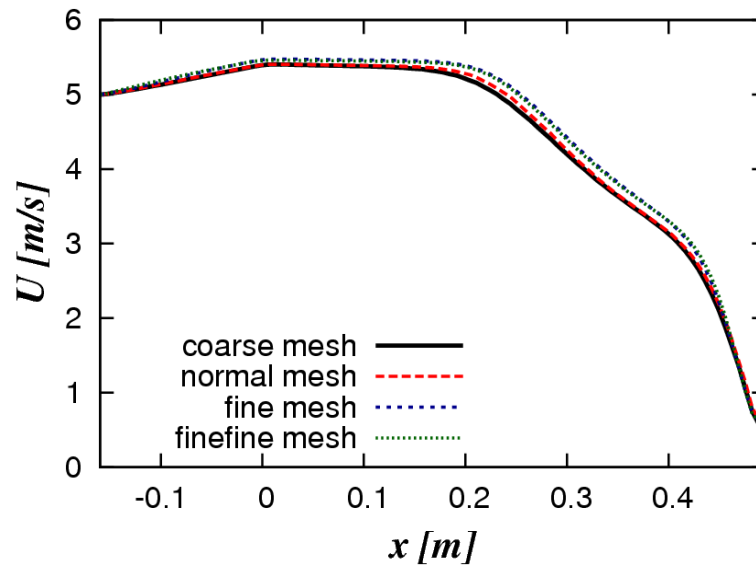


Figure 6-9 - Velocity data sampled along the Inlet line of different mesh sizes using OpenFoam (RANS).

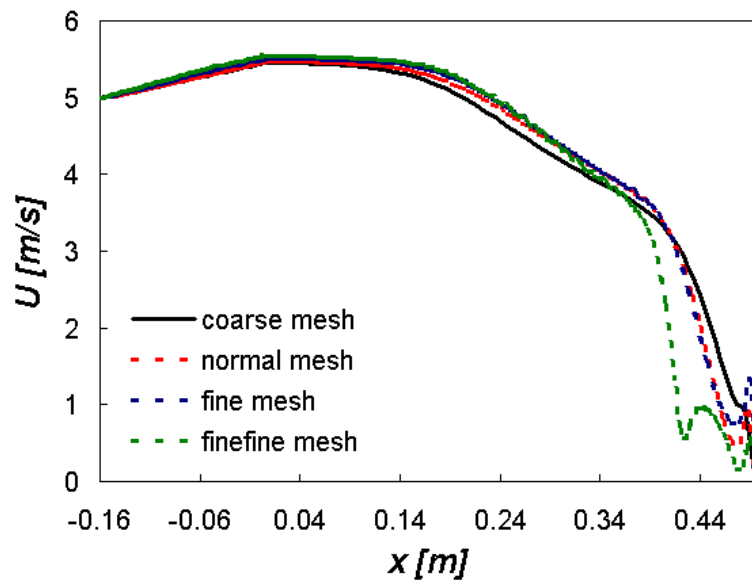


Figure 6-10 - Velocity data sampled along the Inlet line of different mesh sizes using AVL Fire (RANS).

Generally, the velocity along the Inlet line remains quite constant until a distance of 0.2 m, then starts to drop down until it is zero on the opposite wall. Because of the smaller cross section area of the Outlet, the velocity sampled along the Outlet line increases from approximately 1 m/s in the chamber to more than 6.5 m/s in the Outlet. These results absolutely confirm the expectations and were obtained from both simulation programs.

It is worth mentioning that the velocity profiles of the different mesh sizes, gained from OpenFoam, matched quite well. Instead, the results of the velocity profiles obtained from AVL Fire appeared quite affected by the mesh refinement. An explanation could be found in the different used residuals. The OpenFoam simulations were calculated with a value of  $10^{-4}$ , while residuals of  $10^{-3}$  were used for AVL Fire.

Due to the typical unsteadiness of a turbulent air flow, the discrepancies in Figure 6-10 can be thus explained by the instantaneous fluctuations of the impinging jet around the stagnation point on the chamber wall. Concerning the velocity profiles along the sampling lines, a steeper decay for the Outlet can be observed.

Moreover, the coarse mesh is sufficient for the calculation of the flow profile in the chamber. This advantage lowers the computational time and cost for the industrial application.

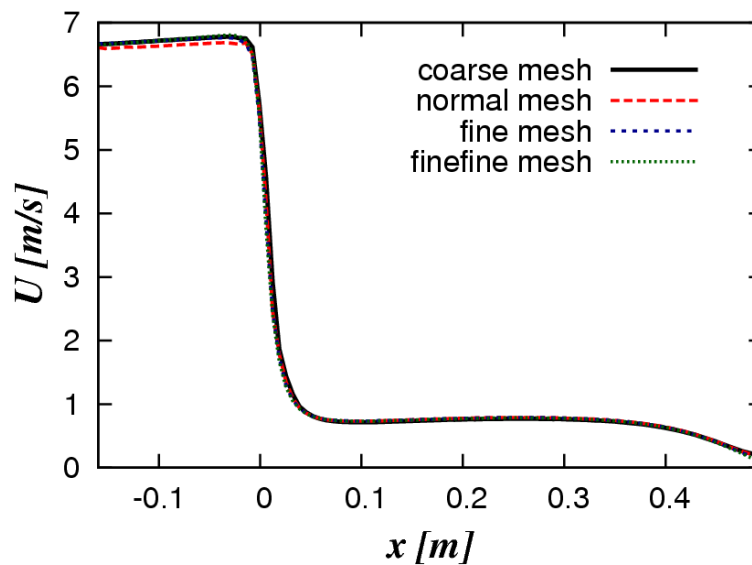


**Figure 6-11 - Velocity data sampled along the Outlet line of different mesh sizes using OpenFoam (RANS).**

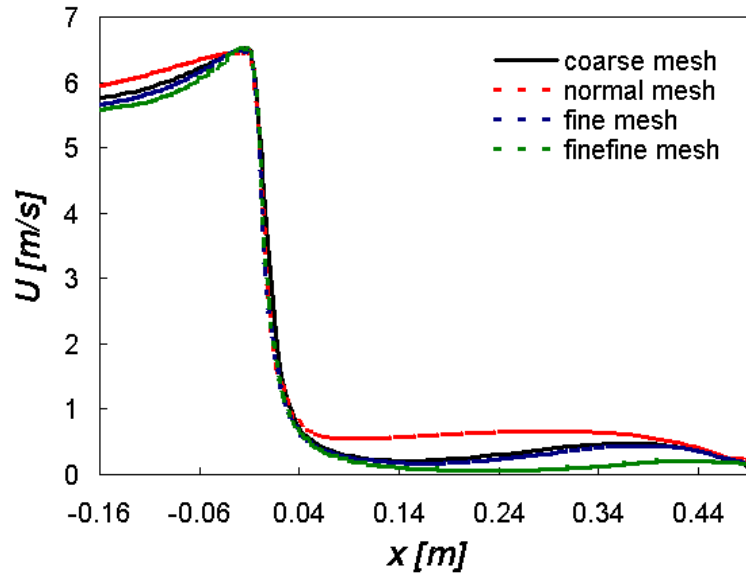


Figure 6-12 - Velocity data sampled along the Outlet line of different mesh sizes using AVL Fire (RANS).

The volumetric flow rate  $\Phi$  over the InletOutlet1 and InletOutlet2 faces can be calculated by multiplying the normal to a face with the velocity vector and integrating it over all the boundary faces.

$$\Phi = \vec{n} \cdot \vec{U} \quad (54)$$

The volumetric flow rates of the Inlet and the Outlet were both equal to  $4.01\text{E-}03 \text{ m}^3/\text{s}$ . This means that the equation of continuity was confirmed. Because of the non-perfect round shape of the patches a minor variation occurs compared to the calculated value of  $4.02\text{E-}03 \text{ m}^3/\text{s}$ .

Furthermore, a y-plane through the Inlet was cut to represent the velocity as well as the kinetic energy distributions of the three different kinetic intensities, i.e. 2.5 %, 5 % and 10 % (see Table 4-2). The results are illustrated in Figure 6-13.

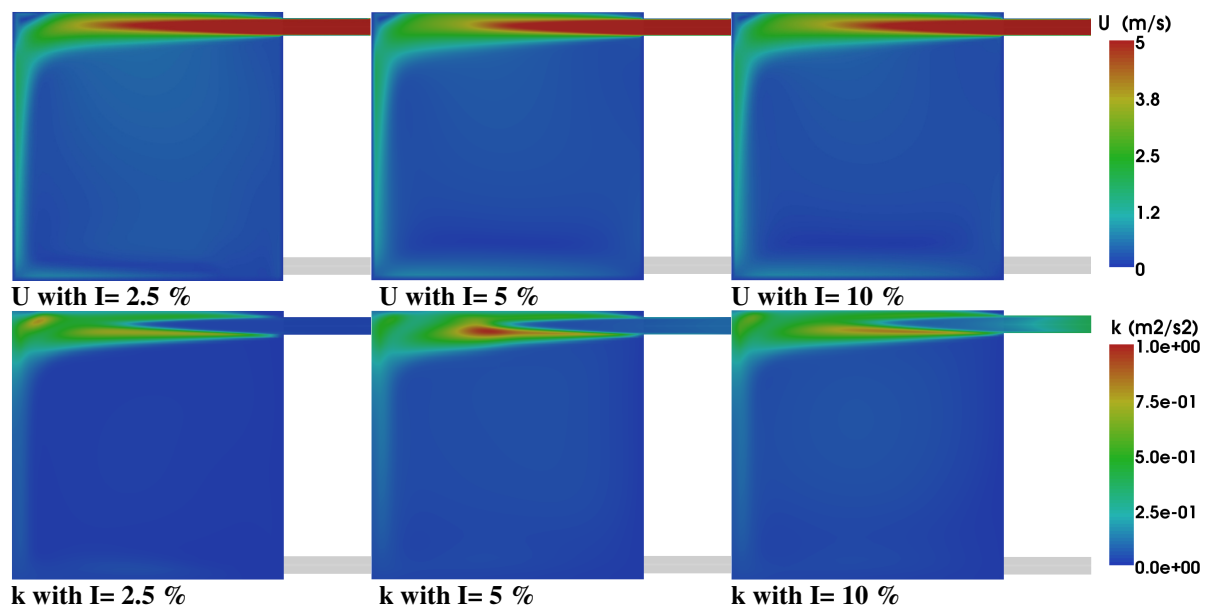


**Figure 6-13 - Velocity and kinetic energy distributions with different turbulence intensities (cut through Inlet using OpenFoam, RANS).**

The velocity distributions of the different turbulence intensities looked similar. The section with the highest velocities appeared as a red flame coming from the Inlet. In the case of 2.5 % the tip of the so-called flame reached the furthest into the chamber.

Moreover, the turbulent kinetic energy  $k$  describes the entity of the local velocity fluctuations, thus can be correlated to the intensity of the turbulent effects. Areas with higher turbulence were produced in the edge of the chamber as well as underneath the highest velocity plume. Surprisingly, in the case of 5 % turbulence intensity the highest kinetic energy could be reached. At turbulence intensities of 2.5 % and 10 % the kinetic energy differed marginally.

$U_z$  was sampled along the x-axis of the Inlet and the Outlet to precisely compare the results of varying turbulence intensities ( $I$ ). The z-velocity vectors along these both lines are illustrated in Figure 6-14. The different turbulence intensities had no mentionable impact on the velocity profiles. The higher the turbulence intensity the longer is the computational time for converging the system.

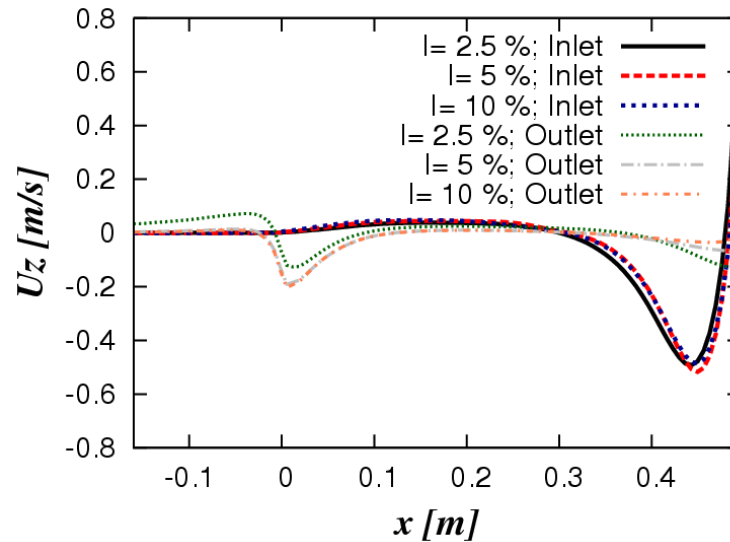


**Figure 6-14 -  $U_z$  of different turbulence intensities ( $I$ ) sampled along the Inlet and the Outlet line using OpenFoam (RANS).**

### 6.2.2. Mass Transport in Test Chamber

As a result of the simulations of species transport, the mass transfer coefficient in the gas phase was calculated. To achieve this, the simulation was run until a constant  $H_2O_2$  concentration in the chamber was reached, which consequently means that the gradient of  $H_2O_2$  in the chamber was equal to zero:

$$\frac{\partial N_{Chamber}}{\partial t} = 0 \quad (55)$$

One mass transport simulation using the normal mesh was performed by “freezing” the flow profiles, thus deactivating continuity and momentum equations, and calculating only the transport equation for scalar diffusion/convection. This assumption is reasonable as the  $H_2O_2$  gaseous species will minimally affect the air flow inside the chamber.

The flow profiles and the species transport of  $H_2O_2$  for all four grid refinements were also calculated using LES.

The mean concentration of  $H_2O_2$  over the Outlet ( $c_{H_2O_2, PatchMean}$ ) was obtained by the performed simulations (see Figure 6-15 and Figure 6-16). By multiplying this dimensionless concentration with the reference concentration ( $1 \text{ kmol/m}^3$ ) and the

volume flow of the Outlet ( $4.02\text{E-}03 \text{ m}^3/\text{s}$ ), the mass flow of  $\text{H}_2\text{O}_2$  from the Outlet can be achieved, see Eqn. (56)

$$\dot{N}_{out} = c_{\text{H}_2\text{O}_2,ref} \cdot c_{\text{H}_2\text{O}_2,PatchMean} \cdot \dot{V}_{out} \quad (56)$$

Because of the mass balance of the test chamber, the mass flow of  $\text{H}_2\text{O}_2$  from the polymer can be equalized with the mass flow of  $\text{H}_2\text{O}_2$  from the Outlet, namely:

$$\dot{N}_{Polymer} = \dot{N}_{out} \quad (57)$$

As a result the mass transfer coefficient of the gas phase can be calculated by transforming Eqn. (58). The surface of the polymer in the chamber is  $0.04 \text{ m}^2$  (see Table 4-1), while the concentration of  $\text{H}_2\text{O}_2$  in the bulk phase ( $c_{\text{H}_2\text{O}_2,\infty}$ ) is zero.

$$\dot{N}_{polymer} = \beta_g \cdot A_{Polymer} \cdot (c_{\text{H}_2\text{O}_2,ref} - c_{\text{H}_2\text{O}_2,\infty}) \quad (58)$$

Figure 6-15 shows the results of the simulation of the species transport in the test chamber (normal mesh) using the frozen velocity field.

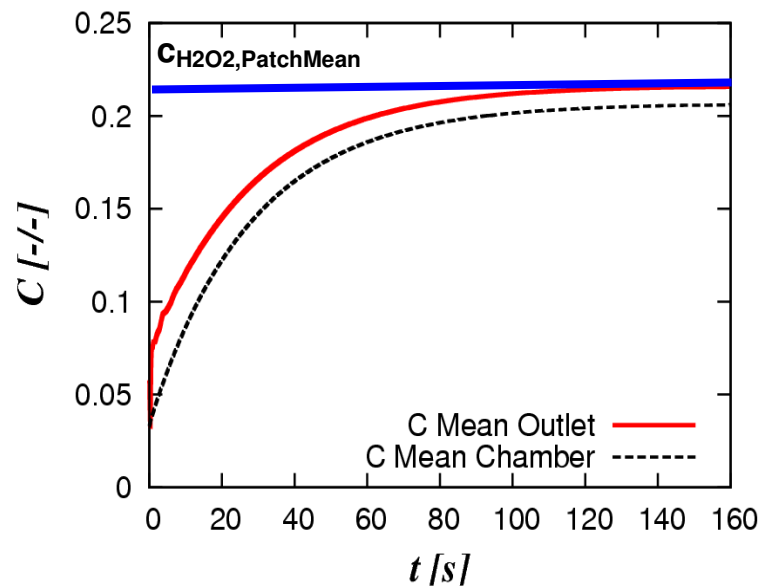


Figure 6-15 - Mean concentration of  $\text{H}_2\text{O}_2$  with frozen velocity field using OpenFoam (normal mesh).

The mean concentration of  $\text{H}_2\text{O}_2$  at the Outlet is described by the red line, while the mean  $\text{H}_2\text{O}_2$  concentration in the chamber is characterized by the dashed black line. The steady-state of the species transport in the chamber is reached after 120 s (see blue line). At this time the chamber is totally purged for the fourth time.

The mean concentration in the chamber is 95% of the mean concentration of  $\text{H}_2\text{O}_2$  at the Outlet. This result shows that more  $\text{H}_2\text{O}_2$  is purged out than inserted in the chamber.

The calculated mass transfer coefficient of  $\text{H}_2\text{O}_2$  in the gas phase from the simulation is  $2.17\text{E-}02$  m/s. Referred to  $2.73\text{E-}02$  m/s for  $\beta$ , calculated from the Sherwood correlation for a overflowed plane sheet, the value gained from the simulation seems to be in an appropriate range.

To obtain  $C_{\text{H}_2\text{O}_2, \text{PatchMean}}$  in the cases of the LES simulation with OpenFoam the concentration of  $\text{H}_2\text{O}_2$  at the Outlet had to be averaged over time starting from the point where the steady-state was reached. This procedure is shown in Figure 6-16. The results for the concentration achieved from the simulation are characterized by the blue line. This concentration was averaged over time in the steady-state region, which occurs after 100 s (see red line). In this case an averaged concentration of  $7.46\text{E-}02$  was obtained.

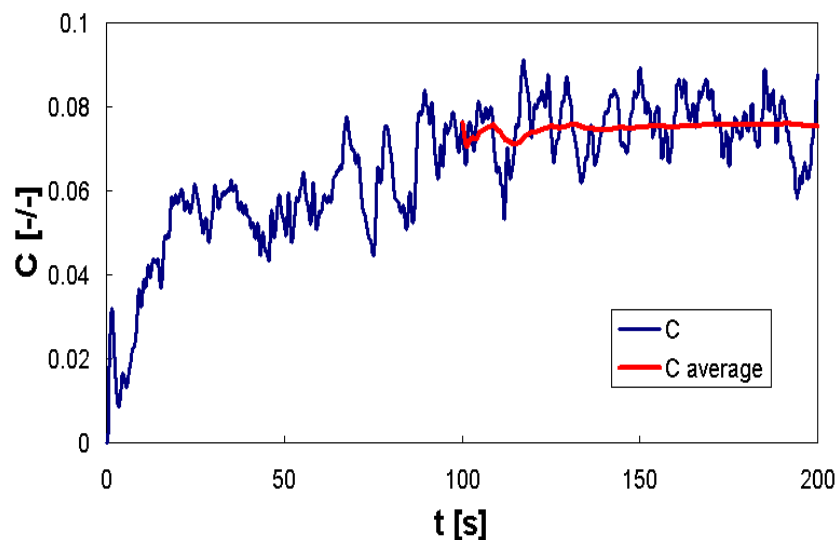


Figure 6-16 - Concentration profile at the Outlet with LES using OpenFoam (coarse mesh).

The final results of  $c_{H_2O_2, PatchMean}$ ,  $\dot{N}_{polymer}$  and  $\beta_g$  for all simulation cases are summarized in Table 6-4.

**Table 6-4 - Results for species transport of all simulation cases using OpenFoam (code: adAbFoam).**

<i>Simulation Case; mesh</i>	$c_{H_2O_2, PatchMean}$ [-/-]	$\dot{N}_{polymer}$ [kmol s <sup>-1</sup> ]	$\beta_g$ [m s <sup>-1</sup> ]
frozen velocity field; normal	2.16E-01	8.68E-04	2.17E-02
LES; coarse	9.45E-02	3.80E-04	9.50E-03
LES; normal	7.34E-02	2.95E-04	7.38E-03
LES; fine	6.73E-02	2.71E-04	6.77E-03
LES; finefine	6.23E-02	2.51E-04	6.26E-03

The mass transfer coefficient in the liquid phase of the normal mesh differs with a factor of 3 between the LES and the simulation with the frozen flow field. Compared to the results of the simulation with the frozen flow field it can be assumed that the results of LES, calculating the flow profile as well as the species transport, rather corresponded to reality. The reason for this is the fact that LES solves real fluctuations of the velocity and  $\beta$  is proportional to the local Reynolds number, thus the local velocity. The results of the LES simulations showed that the mass transfer coefficients lowered with higher grid refinement.

Figure 6-17 illustrates the species transport of H<sub>2</sub>O<sub>2</sub> in the chamber desorbed from the polymer at different time steps. Here, the half of the chamber presents the Outlet. Therefore, the chamber was cut into two halves and ten contours with Y of 0.01, 0.02, 0.03, 0.04, 0.05, 0.06, 0.07, 0.08, 0.09 and 0.1 [kmol m<sup>-3</sup>/kmol m<sup>-3</sup>] were drawn in.

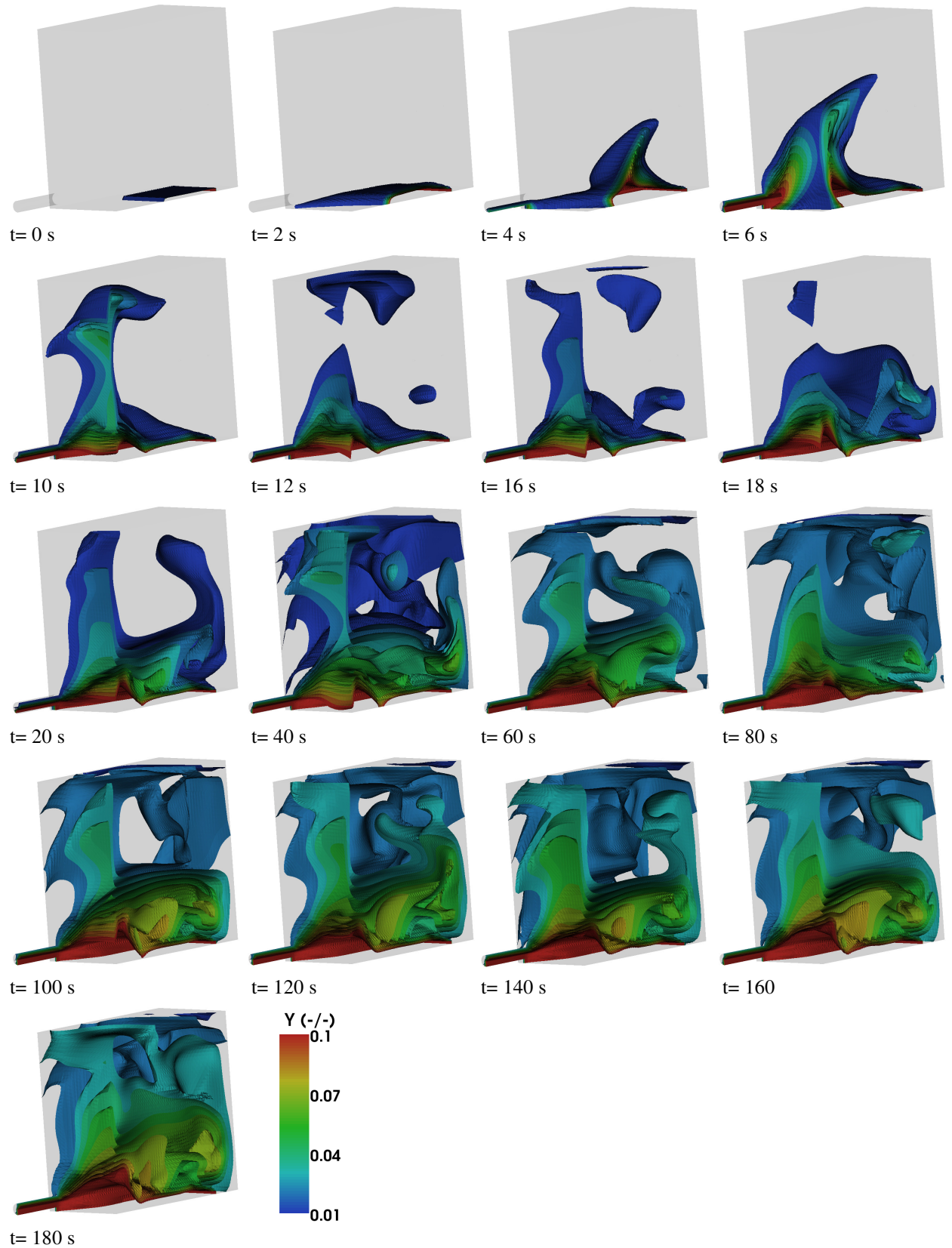
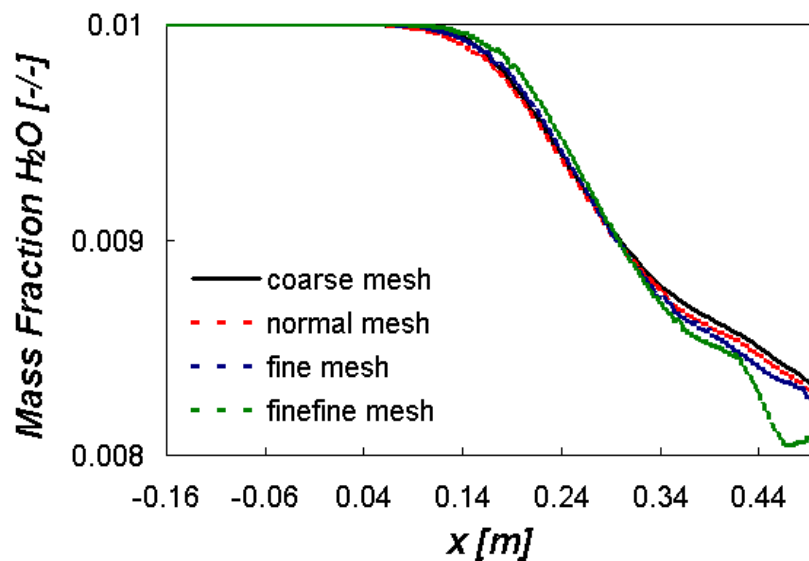


Figure 6-17 - Species Transport ( $Y$  [kmol m<sup>-3</sup>/kmol m<sup>-3</sup>]) in the test chamber (normal mesh, LES, OpenFoam, half side of test chamber with Outlet).

Moreover, the species transport of  $\text{H}_2\text{O}_2$  in the test chamber was examined with all four mesh resolutions using AVL Fire. Therefore, a gas mixture of 0.01 % (w/w)  $\text{H}_2\text{O}$  and 0.99 % (w/w)  $\text{N}_2$ , representing  $\text{H}_2\text{O}_2$  and air, was injected through the Inlet with 5 m/s. For all simulations the mass fraction was calculated until 30 s, i.e. the time for purging the chamber one time, using a frozen velocity field. The results of the mass fraction of  $\text{H}_2\text{O}$  for all four mesh resolutions sampled along a polyline through the Inlet at the time of 30 s are illustrated in Figure 6-18.



**Figure 6-18** - Mass fraction of  $\text{H}_2\text{O}$  [-/-] sampled along the Inlet line of different mesh sizes at 30 s (AVL Fire).

This figure shows that the four mesh resolutions have a similar trend concerning the mass fraction of  $\text{H}_2\text{O}$  after 30 s. For the simple geometry of the test chamber the coarse mesh is sufficient to predict the species transport. This leads to an advantage concerning costs and computation time for the industrial application.

Figure 6-19 presents the results of the distribution of the mass fraction of  $\text{H}_2\text{O}$  at different time steps.

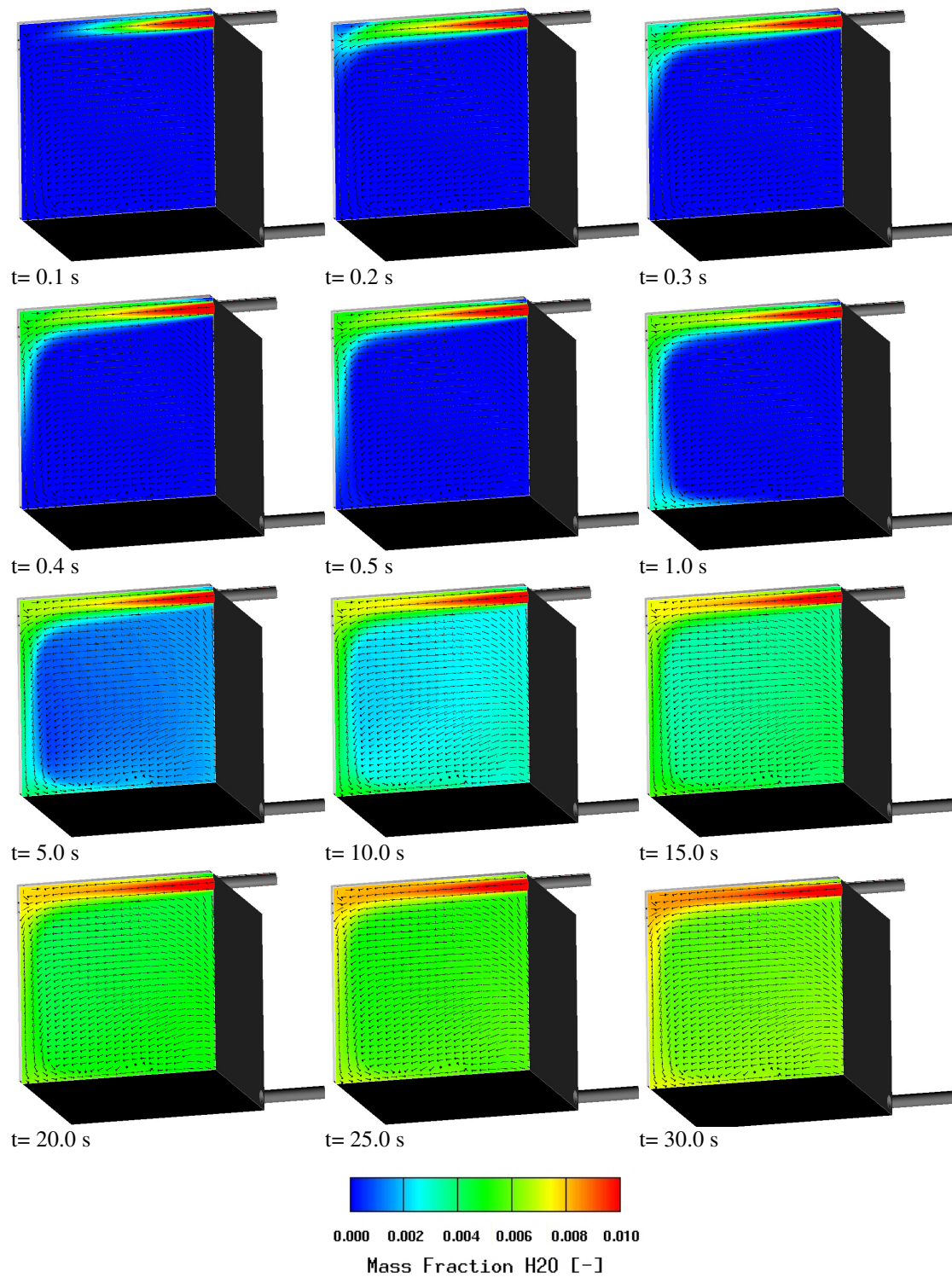


Figure 6-19 - Distribution of the mass fraction of H<sub>2</sub>O at different time steps (cut through the Inlet, normal mesh, AVL Fire).

### 6.2.3. Grid Convergence Study

In order to determine the discretization error caused by numerical uncertainty correlated to the grid resolution, a grid convergence study was carried out following a procedure mentioned by *Slater* and based on the Richardson extrapolation [39].

First of all, the grid refinement ratio  $r$  (see Eqn. (59)), which describes the ratio between the grid length of a coarse mesh  $h_2$  and a fine mesh  $h_1$ , should be equal or greater than 1.1 to exclude errors made by e.g. computer round-off or iterative convergence errors.

To guarantee this condition a grid refinement ratio of 1.3 was used.

$$r = \frac{h_2}{h_1} \quad (59)$$

The order of accuracy  $p$  (see Eqn. (60)) is defined by the order of the leading term of the truncation error. To calculate the order of the grid convergence three grid resolutions with a constant value of  $r$  are essential. In equation (60)  $f_i$  denotes a scalar solution. The subscript  $i$  indicates the refinement level, which means that 3 is the solution of the coarsest grid spacing and 1 is the solution of the finest one.

$$p = \ln\left(\frac{f_3 - f_2}{f_2 - f_1}\right) / \ln(r) \quad (60)$$

The Richardson extrapolation  $f_{h=0}$  describes the solution on a grid spacing  $h=0$  and takes into account the grid refinement ratio  $r$  as well as the order of accuracy.

$$f_{h=0} = f_1 + \frac{f_2 - f_1}{r^p - 1} \quad (61)$$

Here,  $f_1$  and  $f_2$  are the solutions of the two finest grids in the grid convergence study.

To compare the results of the different refined grids, the grid convergence index (GCI), described by Eqn. (62), is calculated. This value is a measurement of percentage, which indicates the error band of the solution from the Richardson extrapolation.

$$GCI_{fine} = \frac{F_s \cdot |\varepsilon|}{r^p - 1} \cdot 100\% \quad (62)$$

Here,  $\varepsilon$  describes the relative error (see Eqn. (63)), while  $F_s$  indicates a factor of safety. For the comparison of two grids the factor of safety is recommended to be 3.0. If three or more grids are used a factor of 1.25 is used.

$$\varepsilon = \frac{f_2 - f_1}{f_1} \quad (63)$$

It is also necessary to check that the solution of each grid is in the asymptotic range of convergence. This is verified, if Eqn. (64) results in 1.

$$\frac{GCI_{23}}{r^p \cdot GCI_{12}} = 1 \quad (64)$$

The grid convergence study was done for all four grids to achieve information about accuracy. Therefore,  $\beta_g$  calculated by LES are examined.

The parameters for the grid convergence study of the meshes finefine, fine and normal as well as fine, normal and coarse are presented in Table 6-5 and Table 6-6. The results of the grid convergence study are illustrated in Figure 6-20.

**Table 6-5 - Parameter for the grid convergence study of finefine, fine and normal mesh.**

<i>Meshes</i>	<i>Normalized Grid Spacing</i>	$\beta_g$ [m s <sup>-1</sup> ]	<i>p</i>	$GCI_{finefine,fine}$ [%]	$GCI_{fine,normal}$ [%]
finefine	1	6.26E-03			
fine	1.3	6.77E-03	0.77	41.79	46.84
normal	1.69	7.38E-03			

For the cases finefine, fine and normal mesh an asymptotic range of 0.9166 was reached. This means that the asymptotic range of convergence, i.e. 1, was not achieved. Also the order of accuracy with a value of 0.77 was low. The mass transfer coefficient was

estimated to be  $f_{h=0} = 5.53E-03$  m/s with an error band of 41.79 % for the finefine and fine grids and 46.84 % for the fine and normal grids.

**Table 6-6 - Parameter for the grid convergence study of fine, normal and coarse mesh.**

<i>Meshes</i>	<i>Normalized Grid Spacing</i>	$\beta_g$ [ $m\ s^{-1}$ ]	<i>p</i>	$GCI_{fine,normal}$ [%]	$GCI_{normal,coarse}$ [%]
fine	1	6.77E-03			
normal	1.3	7.38E-03	4.71	4.28	14.71
coarse	1.69	9.50E-03			

An order of accuracy of approximately 5 was received for the grid convergence study of the fine, normal and coarse meshes. The mass transfer coefficient was estimated to be  $f_{h=0} = 5.87E-03$  m/s with an error band of 4.28 % for the fine and normal grids and 14.71 % for the normal and coarse grids. With 1.0000 the solutions of the mass transfer coefficients were definitely well within the asymptotic range of convergence.

Because of these results it can be assumed that the mass transfer coefficient of the finefine mesh is too low. A reason for this could be the non-reached steady-state. The finefine mesh needed a long computation time and was stopped earlier than the other simulations.

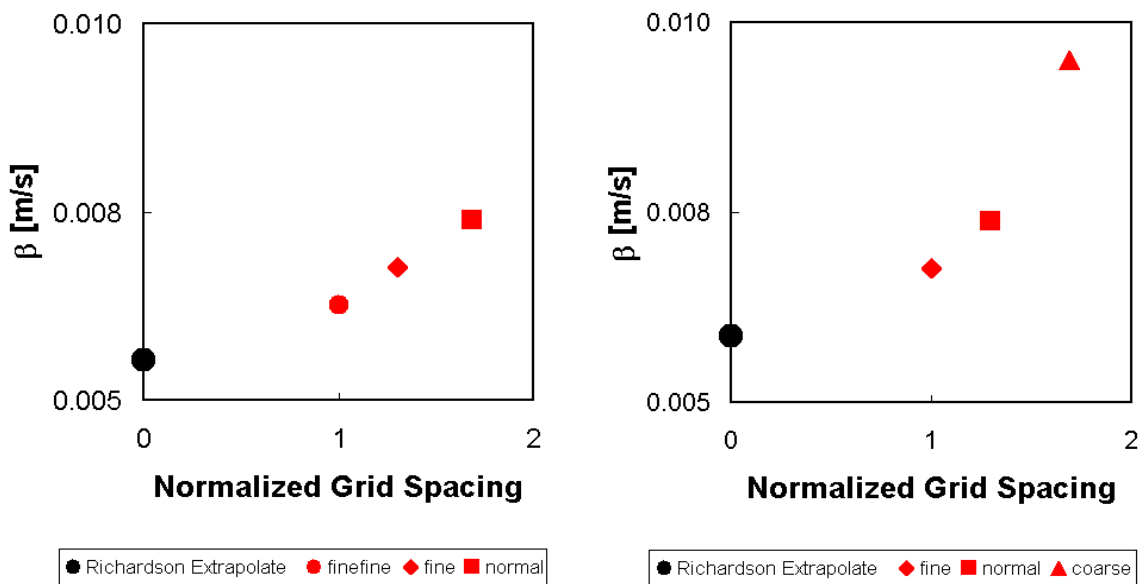


**Figure 6-20 - Results for grid convergence study of finefine, fine and normal meshes (left) as well as fine, normal and coarse meshes (right).**

## 7. Discussion

The mathematical model describing the mass transfer from the polymer into the fluid phase clearly shows that the mass transport inside the polymer is much slower than the mass transfer from the interface to the bulk face. Therefore, the limiting step in the desorption/absorption process is given by the diffusion in the polymer. This fact leads to the assumption that a constant mass transfer rate determined by the diffusion process in the polymer is sufficient to reconstruct the absorption and desorption process. Furthermore, the diffusion coefficient and the saturation concentration are influenced by the temperature.

Concerning the experimental setup, the previous mathematical approaches showed that hydrogen peroxide will fully desorb from thin polymer foils with an area of  $6 \times 10^{-5} \text{ m}^2$  in  $\mu\text{mol}$  range. For this reason a sensitive peroxidase assay kit was used in our work.

The performed experimental investigations were able to quantify the diffusion of  $\text{H}_2\text{O}_2$  in different polymers. The measurement procedure consisted first of an absorption phase, aiming at fully saturate the polymers with  $\text{H}_2\text{O}_2$ . Then, the dissolved  $\text{H}_2\text{O}_2$  was desorbed into an aqueous solution stabilized with EDTA. The desorbed amount was quantified using a sensitive peroxidase assay kit. To determine the diffusion coefficient and the saturation concentration of hydrogen peroxide in different polymers (polyvinylchloride (PVC), polyethylene (PE), low-density polyethylene (LDPE)) and in glass, Fick's second law for a plane sheet was used.

The highest diffusion coefficient for  $\text{H}_2\text{O}_2$  was measured in LDPE ( $4.90 \times 10^{-8} \text{ cm}^2/\text{s}$ , see Figure 7-1), a value namely 2.5 times higher than the one in PP. Instead, the diffusion coefficient in PVC was measured to be 1.8 times lower than the one in PP. This is surprising, since PVC showed the highest saturation concentration. It is currently unclear what caused this slow release of  $\text{H}_2\text{O}_2$  from PVC. It is speculated that this is due to the interaction of plasticizers (i.e., relatively small-size aromatic molecules) present in PVC with hydrogen peroxide. More studies are needed to address this interesting behaviour, i.e. a high saturation concentration but slow diffusion of  $\text{H}_2\text{O}_2$  in PVC. Concerning the diffusion of hydrogen peroxide in glass, no absorption of  $\text{H}_2\text{O}_2$  was measured. The experiments illustrated that the determination of the diffusion coefficient is challenging.

Because of the low diffusion coefficients of  $\text{H}_2\text{O}_2$  in all the considered polymers, minimal differences in the slope of the desorption curve led to large variations of the diffusion coefficients.

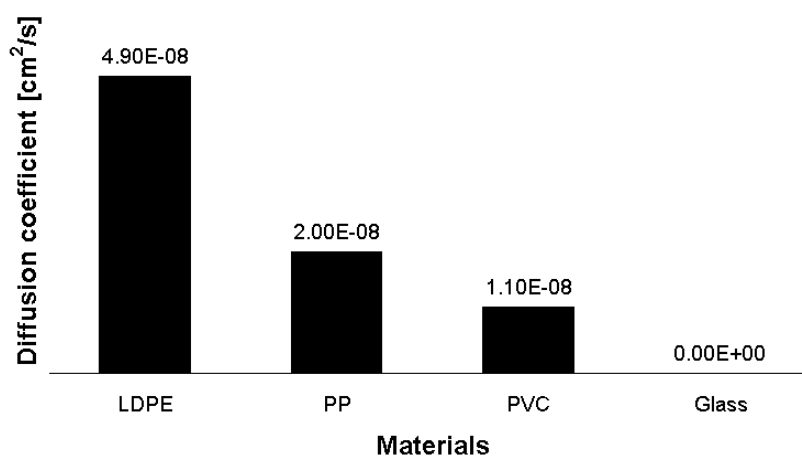


Figure 7-1 - Comparison of the diffusion coefficient of  $\text{H}_2\text{O}_2$  in different materials at 308.15 K.

The results of the comparison of the saturation concentration of  $\text{H}_2\text{O}_2$  in different polymers are illustrated in Figure 7-2. With a saturation concentration of  $8.61\text{E-}02 \text{ kmol/m}^3$ , PVC absorbed the highest amount of  $\text{H}_2\text{O}_2$ , presenting a value even seven times higher than the one measured in PP. The saturation concentration of  $\text{H}_2\text{O}_2$  in PP and in LDPE differed by a factor of 1.6.

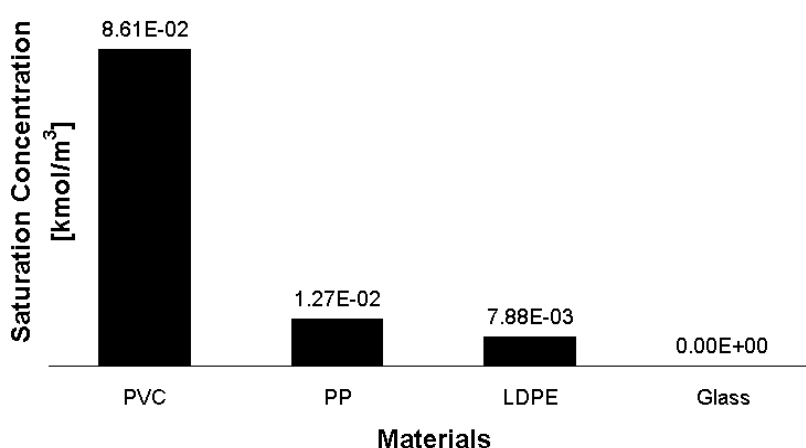


Figure 7-2 - Comparison of the saturation concentration of  $\text{H}_2\text{O}_2$  in different materials at 308.15 K.

The results of all experiments indicated no clear correlation between the diffusion coefficient and the saturation concentration.

With regard to the measurements using NIR imaging, the results did not show clear trends for untreated and H<sub>2</sub>O<sub>2</sub>-saturated polymer samples. An explanation for this behaviour could be the pre-treatment. In fact, the first batch of samples was analyzed directly after the saturation with H<sub>2</sub>O<sub>2</sub>. Precisely, these samples were unwashed and the measurements were done immediately after saturation, where H<sub>2</sub>O<sub>2</sub> was still adsorbed to the surface of the polymer. This might indicate that the NIR method using the HELIOS camera system was able to detect adsorbed H<sub>2</sub>O<sub>2</sub>. Nevertheless, due to the fast measurement system further research should be done to detect H<sub>2</sub>O<sub>2</sub> in polymers using HELIOS camera system. It is however to be expected that only adsorbed H<sub>2</sub>O<sub>2</sub> can be measured with this technique, but not H<sub>2</sub>O<sub>2</sub> absorbed in the polymer.

Decontamination by hydrogen peroxide, despite not completely new, is still in a phase where basic research is required to apply this technology to new areas. An example is filter decontamination, where formaldehyde is still required for the terminal sterilization prior to the disassembly of contaminated filters. H<sub>2</sub>O<sub>2</sub> could do the same job, although not enough is known to convince authorities and inspectors to rely on hydrogen peroxide decontamination technology. In addition to this work, research activities in the area of absorption and condensation phenomena are especially needed to widespread this technique. Other areas could include decontamination strategies for garments, or polymeric compounds and porous materials, even if the absorption process in these materials is more complex. Last but not least, the experimental investigation of condensation and absorption still needs further research to make measurements possible or more precise. Because of the sensitivity of the peroxidase kit, it is also important to investigate a more precise analyzing system for hydrogen peroxide in the  $\mu\text{mol}$  range.

Concerning simulation, the flow profile in the test chamber showed the same trends for all four grid refinements, as well as for both CFD programs, namely OpenFoam and AVL Fire. Generally, the coarse mesh produced the same results as the finer meshes in terms of the flow profiles and species transport inside the chamber. This is an advantage leading to low computational time and therefore low cost in industrial applications.

Moreover, a code for the calculation of the desorption of hydrogen peroxide from the polymer into the chamber was implemented for OpenFoam and tested successfully. The grid convergence studies of the mass transfer coefficient with all four mesh refinements showed an exponential trend leading to low discretization errors.

These results illustrated the importance of computational fluid dynamics in the sector of decontamination technology. CFD is able to provide significant information about local temperatures, fluid velocities and “worst case” airflow locations in the isolator. Also an exact declaration of the mass transfer of hydrogen peroxide from the polymer into the chamber can be made. Hence, computational fluid dynamics methods were demonstrated to be valuable engineering tools for analyzing and modelling isolators, thus to answer experimental unknown questions and design problems. Therefore, a previous simulation of the isolator can minimize the time consumed by operational qualification (OQ) as well as by performance qualification (PQ).

## 8. References

- [1] Mueller H.-J., Sommermeyer K., Cech F.; Permeation of gaseous hydrogen peroxide and peracetic acid into IV bags during their surface sterilisation; *The Pharmaceutical Journal* 10 (2003); p. 84-86.
- [2] EPA; Compilation of available data on Building Decontamination Alternatives; Office of Research and Development; National Homeland Security Research Center; <http://www.epa.gov/nhsrc/pubs/600r05036.pdf>; downloaded October 2010.
- [3] Unger-Bimczok B., Kottke V., Hertel C., Rauschnabel J.; The Influence of Humidity, Hydrogen Peroxide Concentration, and Condensation on the Inactivation of *Geobacillus stearothermophilus* Spores with Hydrogen Peroxide Vapor; *J Pharm Innov* 3 (2008); p. 123-133.
- [4] Sigwarth V., Moirandat C.; Development and quantification of H<sub>2</sub>O<sub>2</sub> decontamination cycles; *Pda Journal of Pharmaceutical Science and Technology* 54 (4) (2000); p. 286-304.
- [5] Radl S., Ortner S., Sungkorn R., Khinast J.G.; The Engineering of Hydrogen Peroxide Decontamination Systems; *J Pharm Innov* 4 (2009); p. 51-62.
- [6] Claassen M.; Neues Einrichtungs- und Sterilisationskonzept für Laborräume; Diploma Thesis; Academy of Bremerhaven; (2010).
- [7] Rohatgi N., Schubert W., Knight J., Quigley M., Forsberg G., Ganapathi G., Yarbrough C., Koukol R.; Development of Vapor Phase Hydrogen Peroxide Sterilization Process for Spacecraft Applications; Jet Propulsion Laboratory; California Institute of Technology; California; Pasadena <http://trs-new.jpl.nasa.gov/dspace/bitstream/2014/12593/1/01-0832.pdf>; downloaded October 2010.
- [8] Gonzalez M.M.; Materials of Construction for Pharmaceutical Equipment; *Encyclopedia of Pharmaceutical Technology*; Third Edition; Informa Healthcare USA Inc. (2007); p. 2237-2242.
- [9] Jenke D.; Evaluation of the Chemical Compatibility of Plastic Contact Materials and Pharmaceutical Products; Safety Considerations Related to Extractables and Leachables; *Journal of Pharmaceutical Science* 96 (10) (2007); p. 2566-2581.
- [10] Smith E.J.; Elastomeric Components for the Pharmaceutical Industry; *Encyclopedia of Pharmaceutical Technology*; Third Edition; Informa Healthcare USA Inc. (2007); p. 1466-1481.
- [11] Jenke D.R.; Evaluation of model solvent systems for assessing the accumulation of container extractables in drug formulations; *International Journal of Pharmaceutics* 224 (2001); p. 51-60.

- [12] Treleano A., Wolz G., Brandsch R., Welle F.; Investigation into the sorption of nitroglycerin and diazepam into PVC tubes and alternative tube materials during application; *International Journal of Pharmaceutics* 369 (2009); p. 30-37.
- [13] Ball D., Blanchard J., Jacobson-Kram D., McClellan R.O., McGovern T., Norwood D.L., Vogel W.M., Wolff R., Nagao L.; Development of Safety Qualification Thresholds and Their Use in Orally Inhaled and Nasal Drug Product Evaluation; *Toxicological Science* 97 (2) (2007); p. 226-236.
- [14] Piringer O.G., Baner A.L.; *Plastic Packaging*; Second Edition; Wiley-VCH Verlag GmbH & Co. KGaA; Weinheim (2008).
- [15] <http://www.fabes-online.de/software.php?lang=de>; downloaded December 2010.
- [16] Gail L., Hortig H.-P.; *Reinraumtechnik*; Second Edition; Springer (2004).
- [17] <http://www.bioquell.com/US/default.asp?&pid=526&id=562>; downloaded November 2010.
- [18] <http://www.sterislifesciences.com/Products/Equipment/VHP/VHP-1000ED-Mobile-Biodecontamination-System.aspx>; downloaded November 2010.
- [19] Fisher J., Caputo R.A.; Comparing and Contrasting Barrier Isolator Decontamination Systems; *Pharmaceutical Technology* (2004); p. 68-82.
- [20] Sigwarth V., Stärk A.; Effect of Carrier Materials on the Resistance of Spores *Bacillus sterothermophilus* to Gaseous Hydrogen Peroxide; *PDA Journal of Pharmaceutical Science and Technology* 57 (1) (2003); p. 3-11.
- [21] Huemer H.; *Chemische Thermodynamik 1*; University of Technology Graz; Graz (2008).
- [22] Manatt S.L., Manatt M.R.R.; On the Analyses of Mixture Vapor Pressure Data: The Hydrogen Peroxide/Water System and Its Excess Thermodynamic Functions; *Chemistry-A European Journal* 10 (2004); p. 6540-6557.
- [23] Roduit B., Borgeat C.H., Cavin S., Fragniere C., Dudler V.; Application of Finite Element Analysis (FEA) for the simulation of release of additives from multilayer polymeric packaging structures; *Food Additives and Contaminants* 22 (10) (2005), p. 645-955.
- [24] [http://www.pci.tubs.de/aggericke/PC2/Kap\\_0/Diffusion\\_2.htm](http://www.pci.tubs.de/aggericke/PC2/Kap_0/Diffusion_2.htm), downloaded March 2010.
- [25] Begley T., Castle L., Feigenbaum A., Franz R., Hinrichs K., Lickly T., Mercea P., Milana M., O'Brien A., Rebre S., Rijk R., Piringer O.; Evaluation of migration models that might be used in support of regulations for food-contact plastics; *Food Additives and Contaminants* 22 (1) (2005); p. 73-90.
- [26] Bird R.B, Stewart W.E., Lightfoot E.N.; *Transport Phenomena*; Second Edition; John Wiley & Sons Inc. (2007).

- [27] Crank J.; *The Mathematics of Diffusion*; 1nd Edition; Oxford University Press (1956).
- [28] Mark J.E.; *Polymer Data Handbook*; Oxford University Press (1999).
- [29] Brenn G., Steiner H.; *Materialien zu den Lehrveranstaltungen Transportprozesse I und II*; University of Technology Graz; Graz (2009).
- [30] Brenn G., *Vorlesungsskriptum Stoffübertragung*; University of Technology Graz; Graz (2007).
- [31] Paschedag A.R.; *CFD in der Verfahrenstechnik*; Wiley-VCH Verlag GmbH & Co. KGaA; Weinheim (2004).
- [32] Ferziger J.H., Peric M.; *Numerische Strömungsmechanik*; 3rd Edition, Springer (2002).
- [33] Bakker A.; *Applied Computational Fluid Dynamics Lecture 6- Boundary Conditions*; <http://www.bakker.org/dartmouth06/engs150/06-bound.pdf>; downloaded March 2010.
- [34] Phibbs M.K., Giguere P.A.; *Hydrogen Peroxide and Its Analogues .3. Absorption Spectrum of Hydrogen and Deuterium Peroxides in the Near Ultraviolet*; *Canadian Journal of Chemistry-Revue Canadienne de Chimie* 29 (6) (1951); p. 490-493.
- [35] Invitrogen (Molecular Probes); *Amplex® Red Hydrogen Peroxide/Peroxidase Assay Kit* Catalog no. A22188.
- [36] Zhou M.J., Diwu Z.J., Panchuk-Voloshina N., Haugland R.P.; *A Stable Nonfluorescent Derivative of Resorufin for the Fluorometric Determination of Trace Hydrogen Peroxide: Applications in Detecting the Activity of Phagocyte NADPH oxidase and other oxidases*; *Analytical Biochemistry* 253 (2) (1997); p. 162-168.
- [37] <http://www.biotek.com/resources/articles/reactive-oxygen-species.html>; downloaded October 2010.
- [38] Moor J.; *Application of NIR Imaging and multivariate data analysis for pharmaceutical products*; Diploma Thesis; University of Applied Sciences Munich (2010).
- [39] Slater J.W.; *Examining Spatial (Grid) Convergence*; <http://www.grc.nasa.gov/WWW/wind/valid/tutorial/spatconv.html>; downloaded September 2010.
- [40] Roache P.J.; *Quantification of uncertainty in computational fluid dynamics*; *Annual Review of Fluid Mechanics* 29 (1997); p. 123-160.

## 9. Appendix

### 9.1. Calculation of the Activity Coefficients of $H_2O_2$ and $H_2O$ for a 30 and 70 % (w/w) Aqueous $H_2O_2$ Solution at 298.15 K

For calculating the four-parametric activity coefficient model (Eqn. (5) and Eqn. (6)) mentioned in Chapter 3.1, the Redlich-Kister Parameters have to be defined.

$B_0$  and  $B_1$  can be estimated solving a Lorentzian curve (see Eqn. (65)), while  $B_2$  and  $B_3$  are calculated using the sigmoid curve (see Eqn. (66)) (Manatt et Manatt [22]).

$$B_n = C_0 + C_1 C_2 / [\pi(C_2^2 + (T - C_3))] \quad (65)$$

$$B_n = C_0 + C_1 / [1 + \exp\{C_2(T - C_3)\}] \quad (66)$$

$C_n$  are constants, which are shown in Table 9-1 and the calculated Redlich- Kister Parameters are shown in Table 9-2.

**Table 9-1 - Constants for the calculation of the Redlich-Kister Parameters at 298.15 K.**

	$B_0$ (Lorentzian)	$B_1$ (Lorentzian)	$B_2$ (Sigmoid)	$B_3$ (Sigmoid)
$C_0$	-666.88	126.74	63.18	59.42
$C_1$	-2499.58	-2558.78	-149.93	-199.26
$C_2$	8.26	12.33	0.47	0.83
$C_3$	327.45	343.11	348.16	346.21

**Table 9-2 – Redlich-Kister Parameters at 298.15 K.**

$B_0$ (Lorentzian)	$B_1$ (Lorentzian)	$B_2$ (Sigmoid)	$B_3$ (Sigmoid)
-673.98	122.12	-86.74	-139.84

The activity coefficient for a 30 and 70 % (w/w) aqueous  $H_2O_2$  solution are shown in Table 9-3 and Table 9-4.

**Table 9-3 - Activity coefficient of H<sub>2</sub>O and H<sub>2</sub>O<sub>2</sub> for a 30 % (w/w) aqueous H<sub>2</sub>O<sub>2</sub> solution at 298.15 K.**

	$w_i$	$x_i$	$\gamma_i$
$H_2O_2$	0.30	0.19	0.45
$H_2O$	0.70	0.81	0.95

**Table 9-4 - Activity coefficient of H<sub>2</sub>O and H<sub>2</sub>O<sub>2</sub> for a 70 % (w/w) aqueous H<sub>2</sub>O<sub>2</sub> solution at 298.15 K.**

	$w_i$	$x_i$	$\gamma_i$
$H_2O_2$	0.70	0.55	0.83
$H_2O$	0.30	0.45	0.68

## 9.2. Calibration Curve for 30 % (w/w) Aqueous H<sub>2</sub>O<sub>2</sub> Solutions

First of all, the mean absorption for each concentration and standard deviation were calculated represented by blue triangles and error bars in Figure 9-1.

The mean standard deviation for the concentration measurement was calculated to be  $\sigma_{\text{total,c,Mean}} = 0.141$ . This value takes into account the standard deviation between different absorption runs, as well as the deviation due to the non-linearity of the mean values.

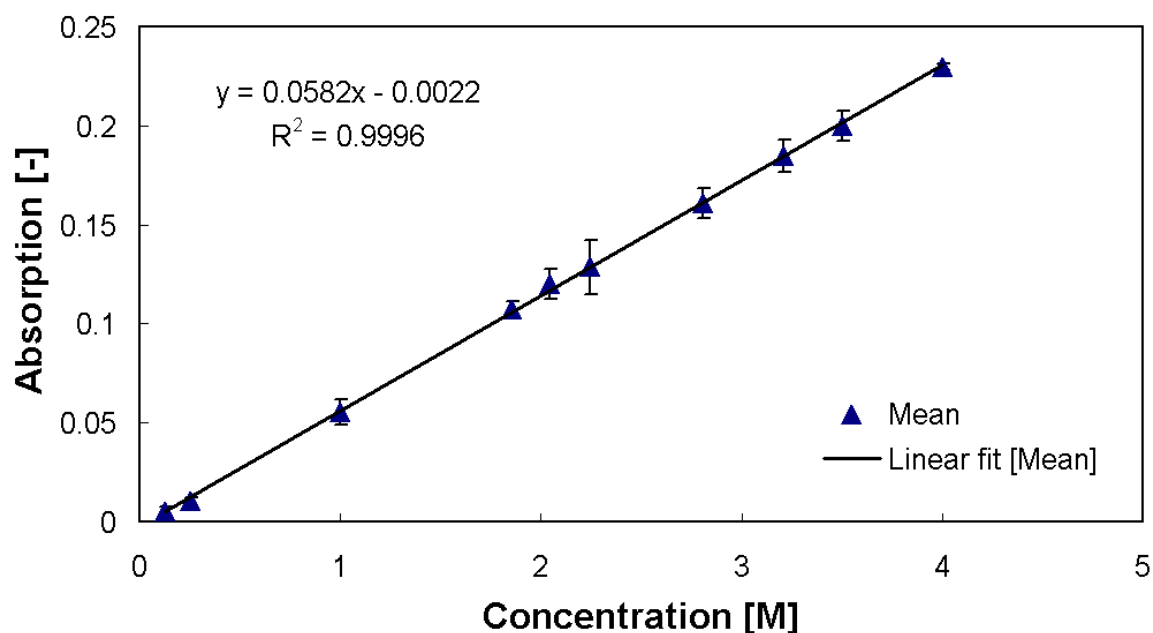


Figure 9-1 - Calibration curve for 30 % (w/w) aqueous H<sub>2</sub>O<sub>2</sub> solution (absorption at 340 nm).

### 9.3. Prediction Model fitting Experimental Data

#### 9.3.1. Stripes

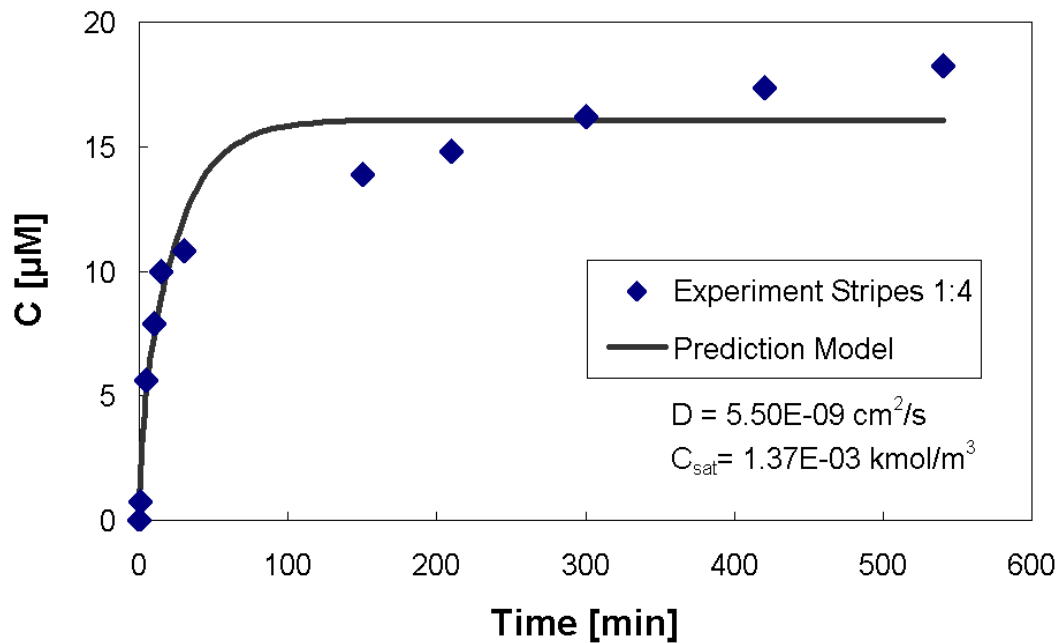


Figure 9-2 - Fit of the desorbed amount of  $\text{H}_2\text{O}_2$  from PP stripes in  $\text{H}_2\text{O}$  with EDTA [50 mg/L] (1:4 dilution, 298.15 K, second run).

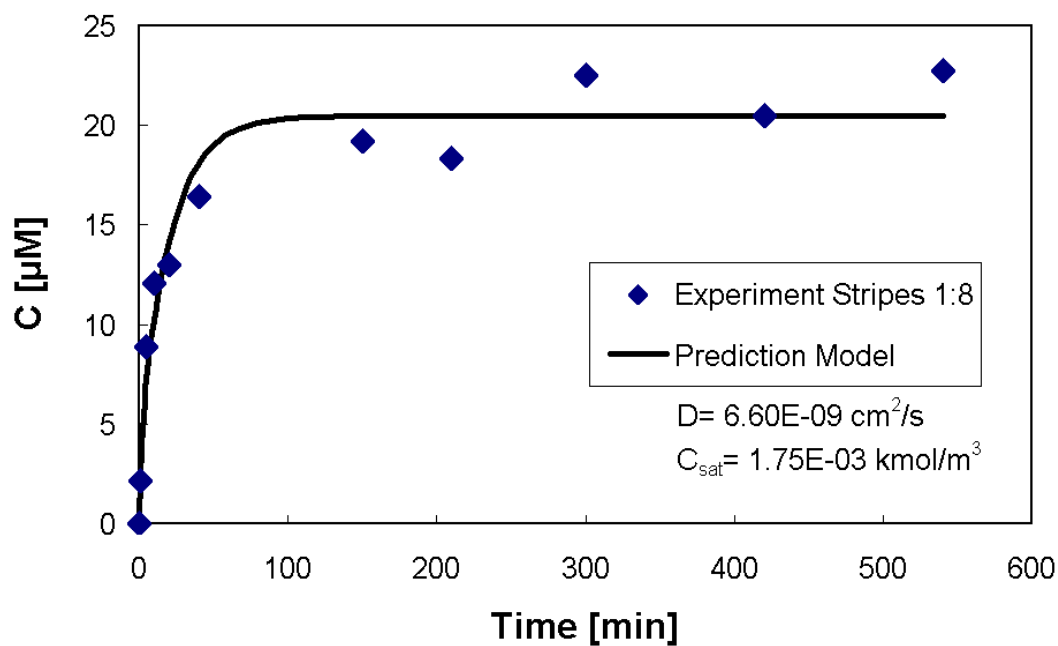


Figure 9-3 - Fit of the desorbed amount of  $\text{H}_2\text{O}_2$  from PP stripes in  $\text{H}_2\text{O}$  with EDTA [50 mg/L] (1:8 dilution, 298.15 K, second run).

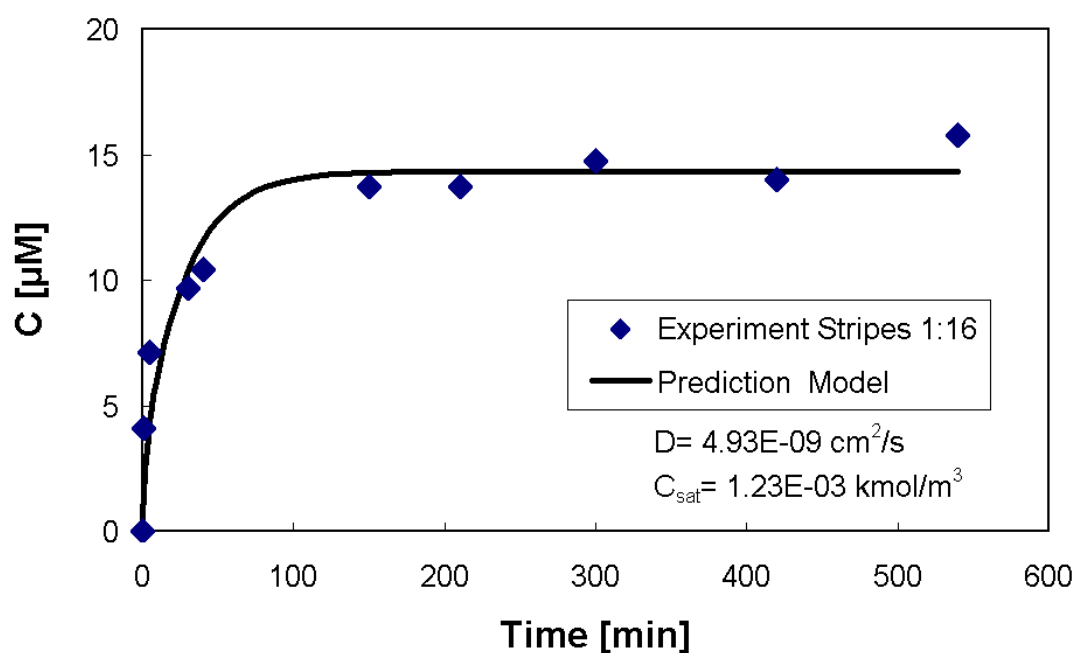


Figure 9-4 - Fit of the desorbed amount of  $\text{H}_2\text{O}_2$  from PP stripes in  $\text{H}_2\text{O}$  with EDTA [50 mg/L] (1:16 dilution, 298.15 K, second run).

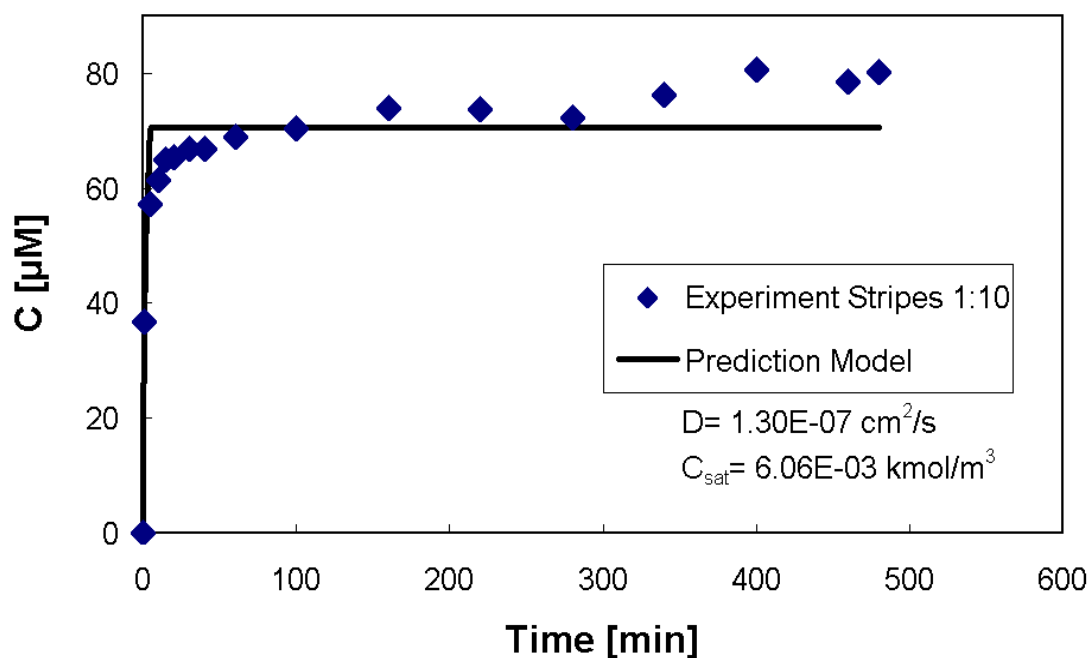


Figure 9-5 - Fit of the desorbed amount of  $\text{H}_2\text{O}_2$  from PP stripes in  $\text{H}_2\text{O}$  with EDTA [50 mg/L] (1:10 dilution, 303.15 K, third run).

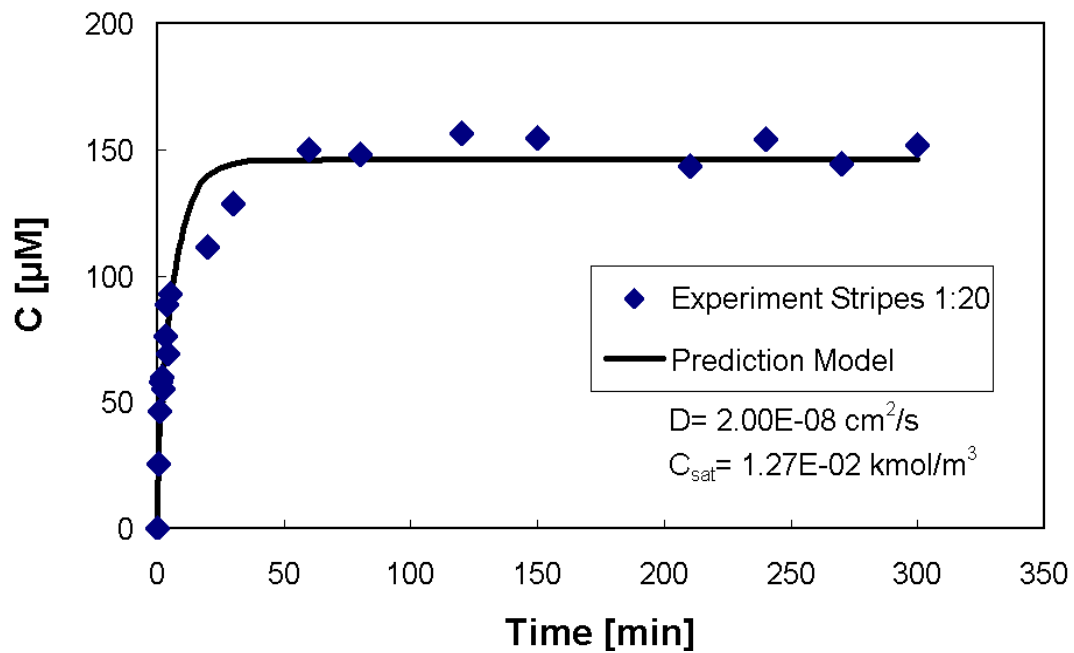


Figure 9-6 - Fit of the desorbed amount of  $\text{H}_2\text{O}_2$  from PP stripes in  $\text{H}_2\text{O}$  with EDTA [50 mg/L] (1:20 dilution, 308.15 K, fourth run).

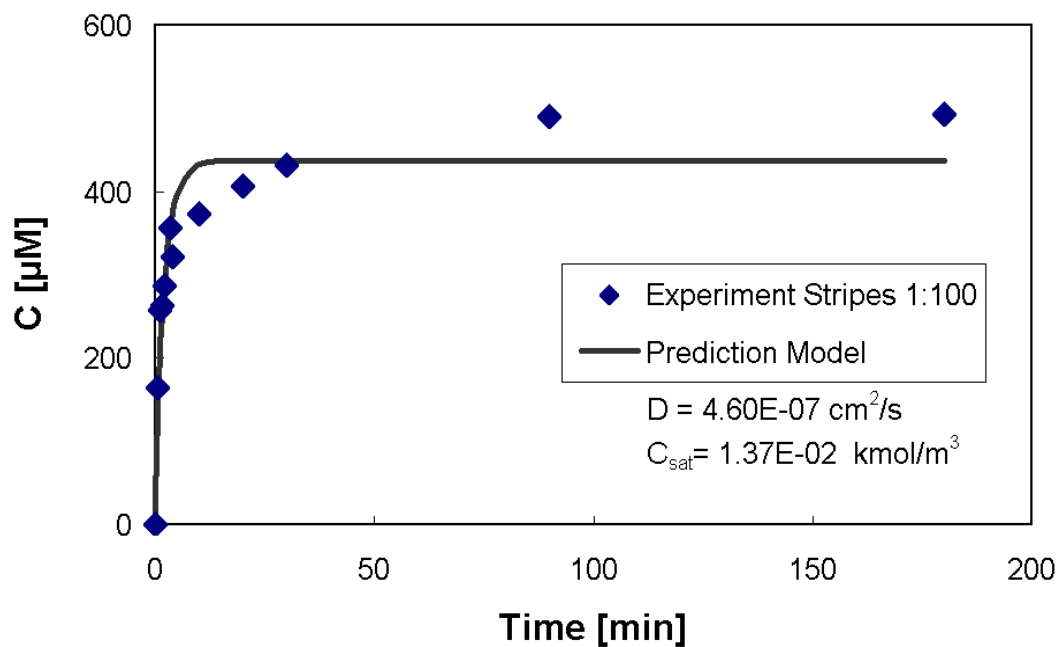


Figure 9-7 - Fit of the desorbed amount of  $\text{H}_2\text{O}_2$  from LDPE stripes in  $\text{H}_2\text{O}$  with EDTA [50 mg/L] (1:100 dilution, 308.15 K, first run).

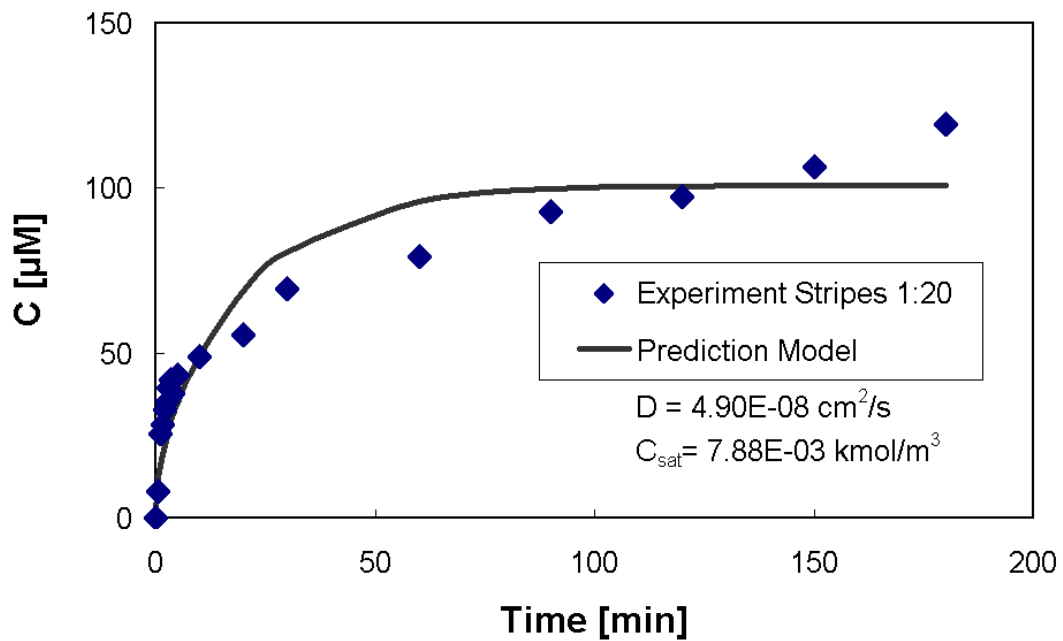


Figure 9-8 - Fit of the desorbed amount of H<sub>2</sub>O<sub>2</sub> from LDPE stripes in H<sub>2</sub>O with EDTA [50 mg/L] (1:20 dilution, 308.15 K, second run).

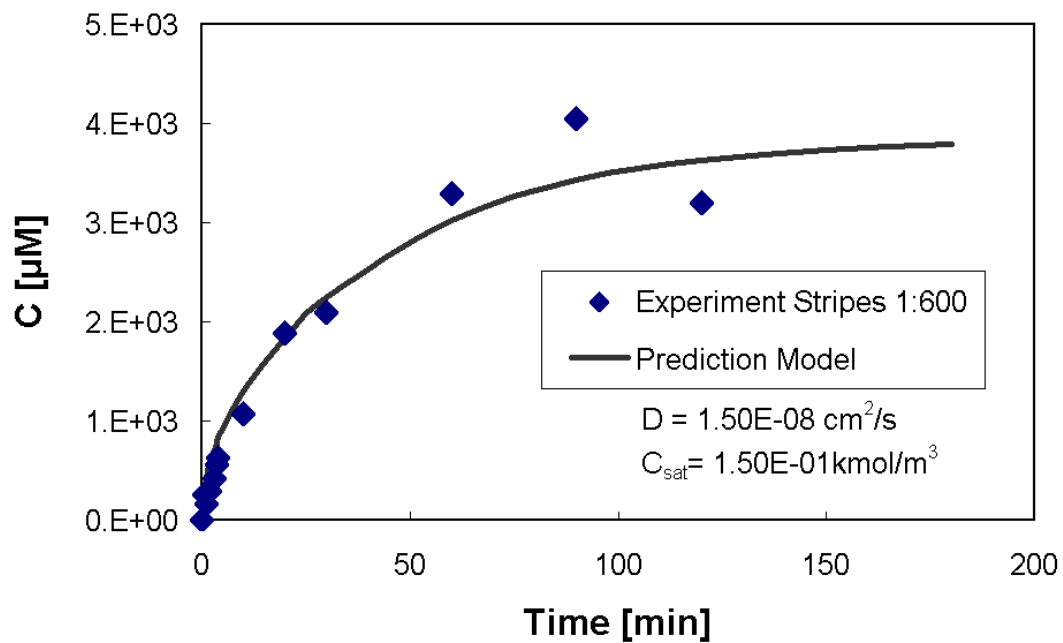


Figure 9-9 - Fit of the desorbed amount of H<sub>2</sub>O<sub>2</sub> from PVC stripes in H<sub>2</sub>O with EDTA [50 mg/L] (1:600 dilution, 308.15 K, first run).

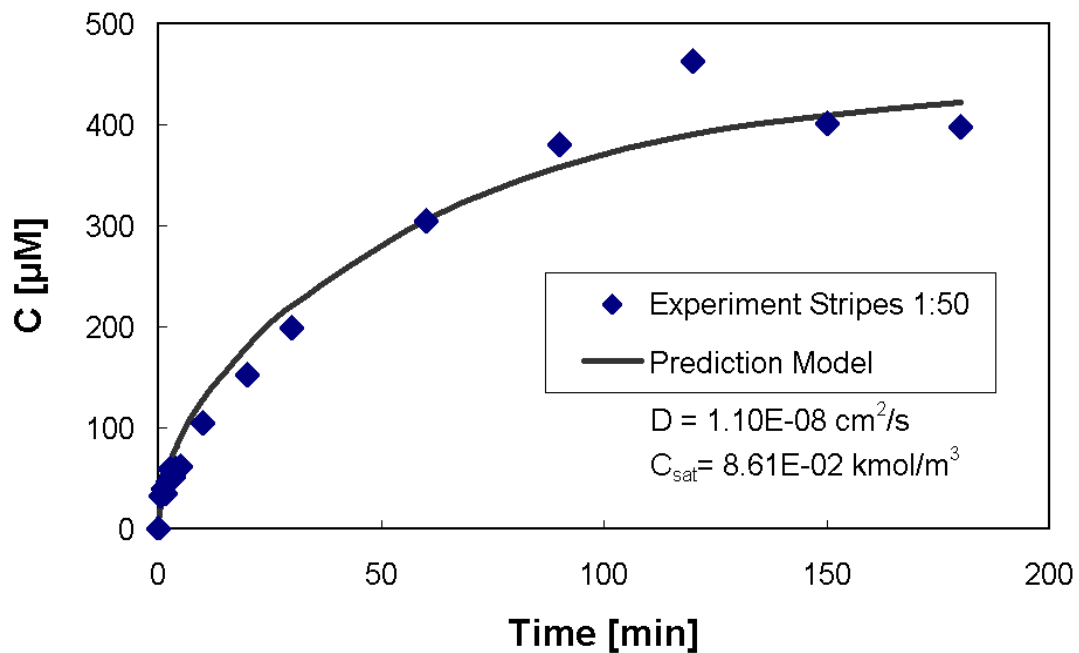


Figure 9-10 - Fit of the desorbed amount of  $\text{H}_2\text{O}_2$  from PVC stripes in  $\text{H}_2\text{O}$  with EDTA [50 mg/L] (1:50 dilution, 308.15 K, second run).

### 9.3.2. Flakes

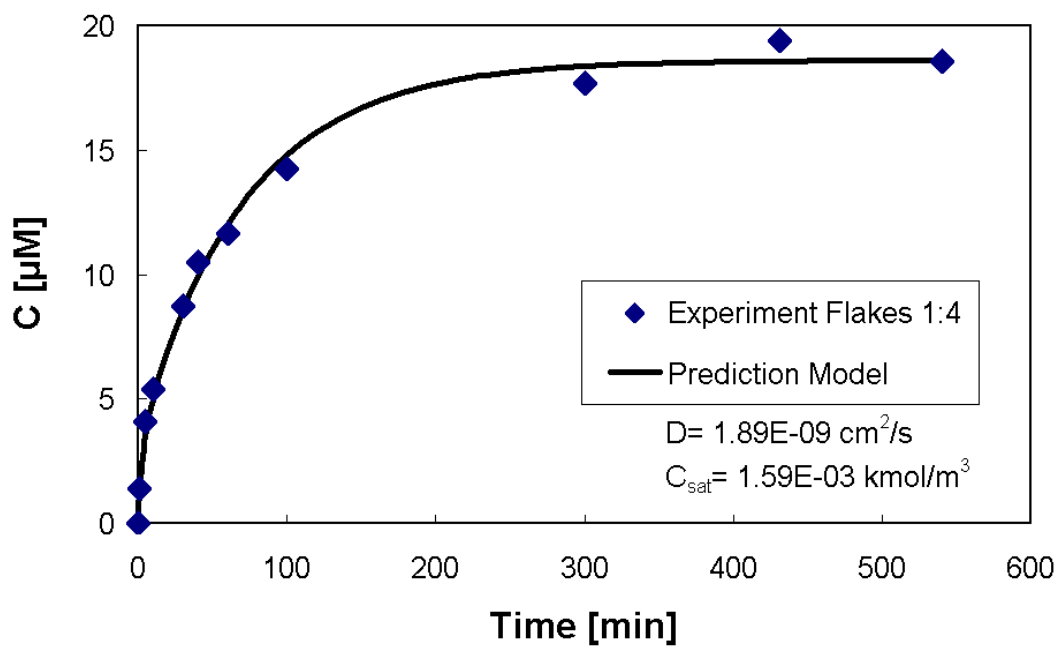


Figure 9-11 - Fit of the desorbed amount of  $\text{H}_2\text{O}_2$  from PP flakes in  $\text{H}_2\text{O}$  with EDTA [50 mg/L] (1:4 dilution, 303.15 K, first run).

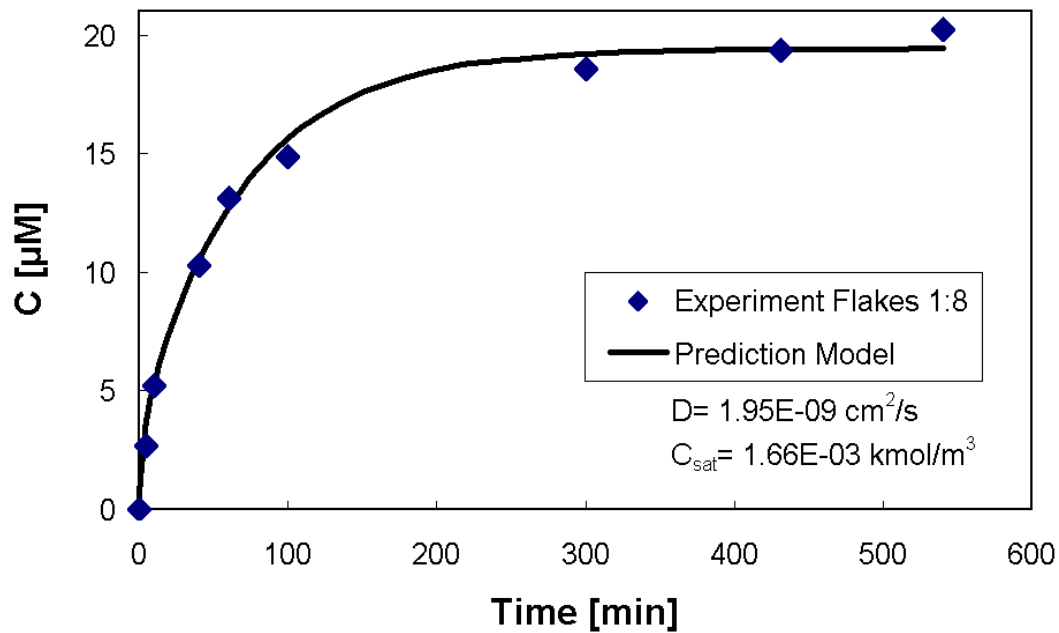


Figure 9-12 - Fit of the desorbed amount of  $\text{H}_2\text{O}_2$  from PP flakes in  $\text{H}_2\text{O}$  with EDTA [50 mg/L] (1:8 dilution, 303.15 K, first run).

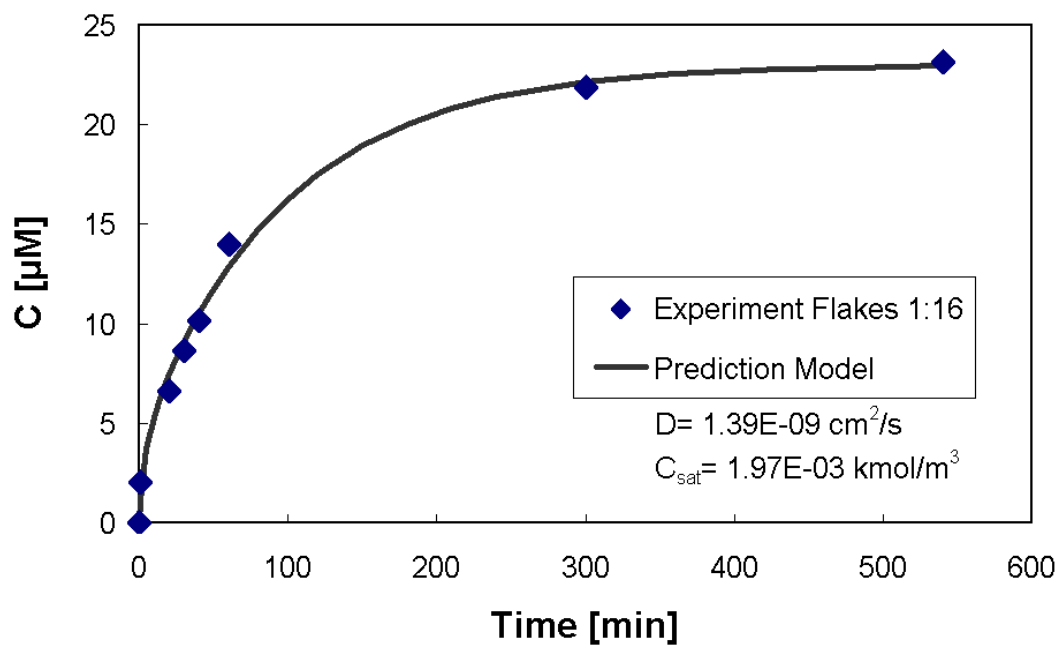


Figure 9-13 - Fit of the desorbed amount of  $\text{H}_2\text{O}_2$  from PP flakes in  $\text{H}_2\text{O}$  with EDTA [50 mg/L] (1:16 dilution, 303.15 K, first run).

## 9.4. Experimental Results

### 9.4.1. Low-Density Polyethylene (LDPE)

Vapour barrier sheet (EN 13984; fire classification E; Type A; SD> 150 m) was used for low-density polyethylene. The experimental settings are mentioned in Table 5-1. The samples were analyzed after 0, 5, 1, 1.5, 2, 2.5, 3, 3.5, 4, 5, 10, 20, 30, 60, 90, 120, 150 and 180 min.

To analyze the amount of desorbed  $H_2O_2$  with the Amplex® Red Hydrogen/ Peroxidase assay kit a dilution factor of 100 was needed for the first run. After reducing the area of the factor of 2.5, a dilution of 1:20 was used for the second run.

The  $H_2O_2$  concentration desorbed from the polymer is shown in Figure 9-14. The diffusion coefficient and the saturation concentration of LDPE are mentioned in Table 9-5 and Table 9-6.

Higher values for the diffusion coefficient and the saturation concentration for the first run were achieved. The diffusion coefficient differentiated by a factor of 9 between first run and second run. The saturation concentration for the first run was 2.5 times higher than the one for the second run. Because of the significantly higher dilution in the first run, it is expected that there were major experimental errors present in this experiment.

**Table 9-5- Results for the diffusion coefficient of  $H_2O_2$  in LDPE at 308.15 K.**

<i>Experiment</i>	<i>D</i> [ $cm^2 s^{-1}$ ]	<i>average D</i> [ $cm^2 s^{-1}$ ]	$\sigma$ [ $cm^2 s^{-1}$ ]
1st run LDPE Stripes	4.60E-07	2.55E-07	2.91E-07
2nd run LDPE Stripes	4.90E-08		

**Table 9-6 - Results for the saturation concentration of  $H_2O_2$  in LDPE at 308.15 K.**

<i>Experiment</i>	$C_{H_2O_2}^{sat}$ [ $kmol m^{-3}$ ]	<i>average <math>C_{H_2O_2}^{sat}</math></i> [ $kmol m^{-3}$ ]	$\sigma$ [ $kmol m^{-3}$ ]
1st run LDPE Stripes	1.37E-02	1.08E-02	4.08E-03
2nd run LDPE Stripes	7.88E-03		

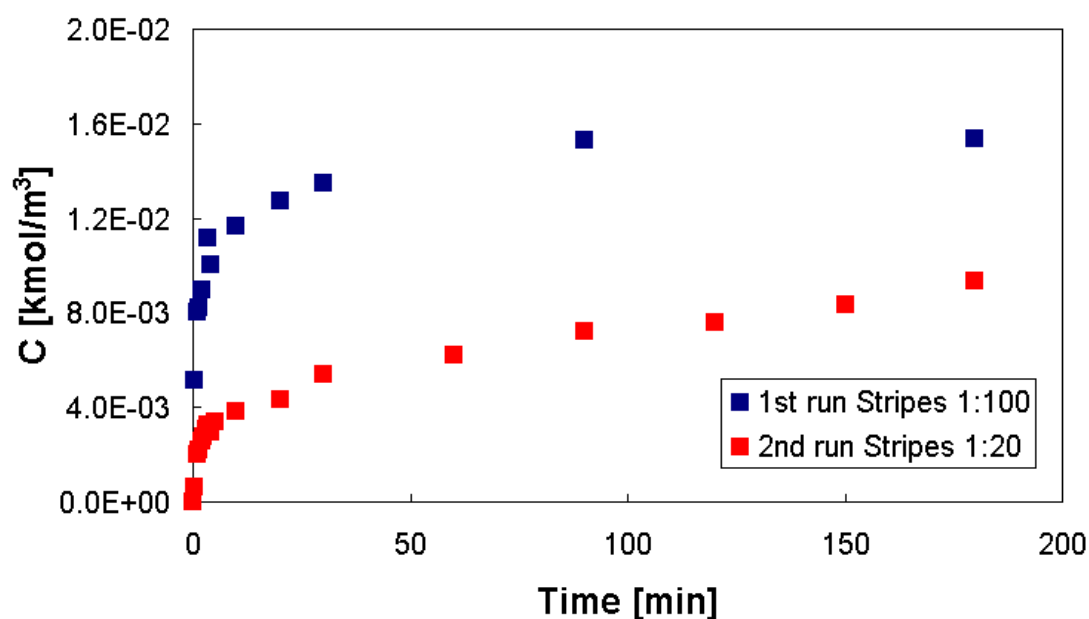


Figure 9-14 - Desorbed amount of  $\text{H}_2\text{O}_2$  from low-density polyethylene at 308.15 K.

#### 9.4.2. Polyvinylchloride (PVC)

As an example for soft PVC a transparent ALCOR<sup>®</sup> sheet was tested. A dilution factor of 600 was needed to measure the desorbed amount of  $\text{H}_2\text{O}_2$  for the first run, while for the second run an area of  $128 \text{ cm}^2$  was used which leads to a dilution factor of 50. The samples were analyzed after 0, 5, 1, 1.5, 2, 2.5, 3, 3.5, 4, 5, 10, 20, 30, 60, 90, 120, 150 and 180 min. Experimental conditions are mentioned in Table 5-1.

The desorption curves of both runs are shown in Figure 9-15. The diffusion coefficient and the saturation concentration of LDPE are mentioned in Table 9-7 and Table 9-8.

Despite the high dilution factor the first run of PVC conformed to the second run. In this case saturation concentration differed only by a factor of 1.7. The ratio of measured diffusion coefficients was 1.5.

Moreover, an obvious change of the material could be observed during the experiments. After the desorption of  $\text{H}_2\text{O}_2$  in deionized water with EDTA [50 mg/L] the clear transparent polymer foil turned to whitish-grey. This leads to the hypothesis, that a modification of the chemical structure of PVC (or the plasticizer in PVC) happened during

the desorption process. After one month of storage protected from light, the PVC foil turned back into its transparent appearance.

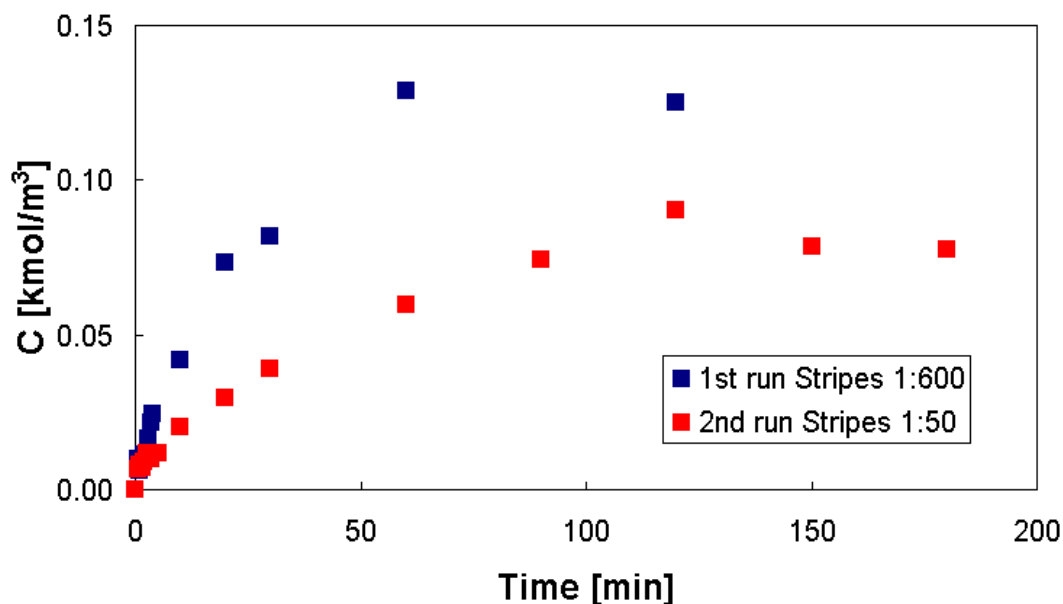


Figure 9-15 - Desorbed amount of H<sub>2</sub>O<sub>2</sub> from polyvinylchloride at 308.15 K.

Table 9-7 - Results for the diffusion coefficient of H<sub>2</sub>O<sub>2</sub> in PVC at 308.15 K.

<i>Experiment</i>	$D$ [cm <sup>2</sup> s <sup>-1</sup> ]	<i>average D</i> [cm <sup>2</sup> s <sup>-1</sup> ]	$\sigma$ [cm <sup>2</sup> s <sup>-1</sup> ]
1st run PVC Stripes	1.50E-08	1.30E-08	2.83E-09
2nd run PVC Stripes	1.10E-08		

Table 9-8 - Results for the saturation concentration of H<sub>2</sub>O<sub>2</sub> in PVC at 308.15 K.

<i>Experiment</i>	$C_{H_2O_2}^{sat}$ [kmol m <sup>-3</sup> ]	<i>average C<sub>H<sub>2</sub>O<sub>2</sub></sub><sup>sat</sup></i> [kmol m <sup>-3</sup> ]	$\sigma$ [kmol m <sup>-3</sup> ]
1st run PVC Stripes	1.50E-01	1.18E-01	4.54E-02
2nd run PVC Stripes	8.61E-02		

#### 9.4.3. Glass (Microscope Slides)

The absorption and desorption of H<sub>2</sub>O<sub>2</sub> in glass was determined. 3 Microscope Slides (brand: ROTH) were placed on a self made shelf over the magnetic stir bar. Experimental settings are mentioned in Table 5-1. The samples were analyzed after 0, 5, 1, 1.5, 2, 2.5, 3, 3.5, 4, 5, 10, 20, 30, 60, 90, 120, 150 and 180 min.

The results of the desorption of  $\text{H}_2\text{O}_2$  from glass are presented in Figure 9-16. No absorption of  $\text{H}_2\text{O}_2$  in glass could be measured.

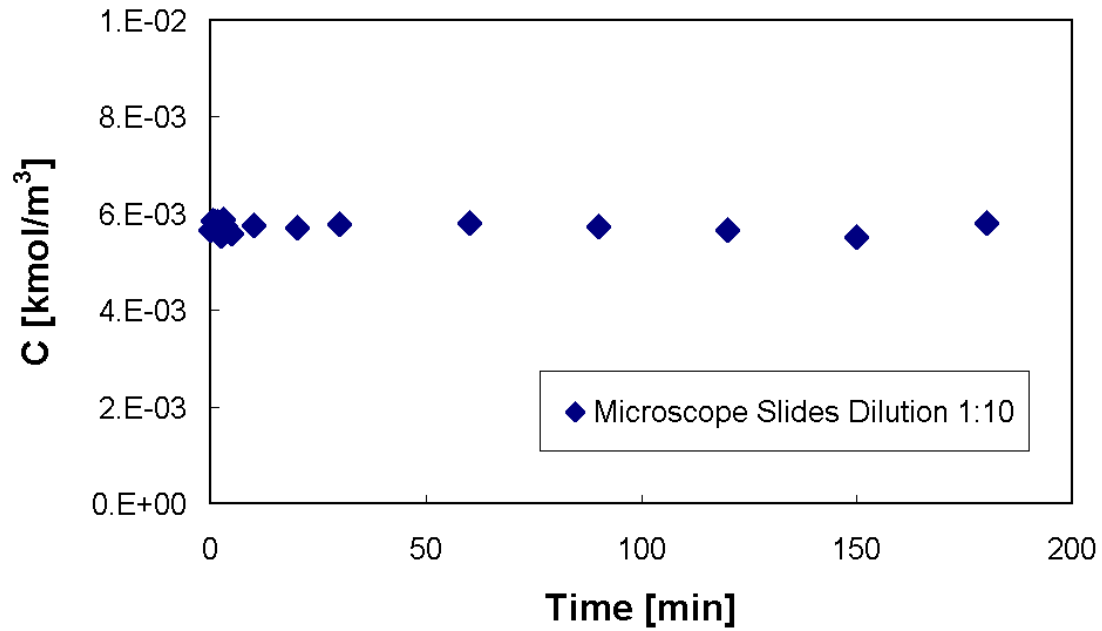


Figure 9-16 - Desorbed amount of  $\text{H}_2\text{O}_2$  from glass at 308.15 K (the first measured  $\text{H}_2\text{O}_2$  concentration was not subtracted, leading to a set off of the concentration curve due to small amounts of adsorbed  $\text{H}_2\text{O}_2$ ).

## 9.5. Code for “adAbFoam” Solver

### 9.5.1. adAbFoam

```

Application
    adAbFoam

Description
    LES + nonreactive scalar transport with absorption to surface model.

\*-----
----*/

#include "fvCFD.H"
#include
"incompressible/singlePhaseTransportModel/singlePhaseTransportModel.H"
#include "incompressible/transportModel/transportModel.H"
#include "incompressible/LESModel/LESModel.H"
#include "IFstream.H"
#include "OFstream.H"
#include "Random.H"

// * * * * *
* * //

int main(int argc, char *argv[])
{
    #include "setRootCase.H"
    #include "createTime.H"
    #include "createMesh.H"
    #include "createFields.H"
    #include "initContinuityErrs.H"
    #include "startFluxLogger.H" //Setup logging file for particle
properties

    Info<< "\nStarting time loop\n" << endl;

    for (runTime++; !runTime.end(); runTime++)
    {
        Info<< "Time = " << runTime.timeName() << nl << endl;

        #include "readPISOControls.H"
        #include "CourantNo.H"
        #include "readTimeControls.H"

        #include "setDeltaT.H"

        if(calculateU) //Perform velocity Calculation only if specified
        {
            sgsModel->correct();

            Info << "calculateU: " << calculateU << endl;
            fvVectorMatrix UEqn
            (
                fvm::ddt(U)
                + fvm::div(phi, U)
                + sgsModel->divDevBeff(U)
            );
        }
    }
}

```

```
);

if (momentumPredictor)
{
    solve(UEqn == -fvc::grad(p));
}

// --- PISO loop
for (int corr=0; corr<nCorr; corr++)
{
    volScalarField rUA = 1.0/UEqn.A();

    U = rUA*UEqn.H();
    phi = (fvc::interpolate(U) & mesh.Sf())
        + fvc::ddtPhiCorr(rUA, U, phi);

    adjustPhi(phi, U, p);

    for (int nonOrth=0; nonOrth<=nNonOrthCorr; nonOrth++)
    {
        fvScalarMatrix pEqn
        (
            fvm::laplacian(rUA, p) == fvc::div(phi)
        );

        pEqn.setReference(pRefCell, pRefValue);

        if (corr == nCorr-1 && nonOrth == nNonOrthCorr)
        {
            pEqn.solve(mesh.solver(p.name() + "Final"));
        }
        else
        {
            pEqn.solve(mesh.solver(p.name()));
        }

        if (nonOrth == nNonOrthCorr)
        {
            phi -= pEqn.flux();
        }
    }

    #include "continuityErrs.H"

    U -= rUA*fvc::grad(p);
    U.correctBoundaryConditions();
}

} // End of IF for U calculation

#include "YEqn.H"
#include "fluxWriter.H"

runTime.write();

Info<< "ExecutionTime = " << runTime.elapsedCpuTime() << " s"
    << "   ClockTime = " << runTime.elapsedClockTime() << " s"
    << nl << endl;
}

Info<< "End\n" << endl;
```

```
    return(0);  
}
```

### 9.5.2. createFields

```
Info<< "Reading transportProperties\n" << endl;  
  
IOdictionary transportProperties  
(  
    IObject  
    (  
        "transportProperties",  
        runTime.constant(),  
        mesh,  
        IObject::MUST_READ,  
        IObject::NO_WRITE  
    )  
);  
  
Info<< "Reading kinematic viscosity nu\n" << endl;  
dimensionedScalar nu  
(  
    transportProperties.lookup("nu")  
);  
  
Info<< "Reading diffusivity D\n" << endl;  
dimensionedScalar D  
(  
    transportProperties.lookup("D")  
);  
  
Info<< "Reading SGS Sc-number\n" << endl;  
dimensionedScalar ScSgs  
(  
    transportProperties.lookup("ScSgs")  
);  
  
word logPatch;  
transportProperties.lookup("logPatch") >> logPatch;  
Info << "Will now log the following patch: " << logPatch << endl;  
  
Info<< "Reading calculateU\n" << endl;  
bool calculateU;  
transportProperties.lookup("calculateU") >> calculateU;  
Info << "calculateU: " << calculateU << endl;  
  
Info<< "Reading field p\n" << endl;  
volScalarField p  
(  
    IObject  
    (  

```

```

        "p",
        runTime.timeName(),
        mesh,
        IOobject::MUST_READ,
        IOobject::AUTO_WRITE
    ),
    mesh
);

Info<< "Reading field U\n" << endl;
volVectorField U
(
    IOobject
    (
        "U",
        runTime.timeName(),
        mesh,
        IOobject::MUST_READ,
        IOobject::AUTO_WRITE
    ),
    mesh
);

Info<< "Reading field Y\n" << endl;
volScalarField Y
(
    IOobject
    (
        "Y",
        runTime.timeName(),
        mesh,
        IOobject::MUST_READ,
        IOobject::AUTO_WRITE
    ),
    mesh
);

# include "createPhi.H"

Info<< "Reading field phiY\n" << endl;
surfaceScalarField phiY
(
    IOobject
    (
        "phiY",
        runTime.timeName(),
        mesh,
        IOobject::READ_IF_PRESENT,
        IOobject::AUTO_WRITE
    ),
    linearInterpolate(Y) * phi
);

label pRefCell = 0;
scalar pRefValue = 0.0;
setRefCell(p, mesh.solutionDict().subDict("PISO"), pRefCell,
pRefValue);

```

```

singlePhaseTransportModel laminarTransport(U, phi);

autoPtr<incompressible::LESModel> sgsModel
(
    incompressible::LESModel::New(U, phi, laminarTransport)
);

// Read turbulent properties if there is no calculation of the flow field
Info<< "ATTENTION: No LES flow simulation - Will calculate nuSGS from
k and epsilon\n" << endl;
Info<< "Reading Cmu\n" << endl;
dimensionedScalar Cmu
(
    transportProperties.lookup("Cmu")
);

Info<< "Reading field kMean to calculate nuTurb\n" << endl;
volScalarField kMean
(
    IOobject
    (
        "kMean",
        runTime.timeName(),
        mesh,
        IOobject::READ_IF_PRESENT,
        IOobject::NO_WRITE
    ),
    mesh
);
Info<< "Reading field epsilonMean to calculate nuTurb\n" << endl;
volScalarField epsilonMean
(
    IOobject
    (
        "epsilonMean",
        runTime.timeName(),
        mesh,
        IOobject::READ_IF_PRESENT,
        IOobject::NO_WRITE
    ),
    mesh
);

```

### 9.5.3. FluxWriter

```

Info<< "Reading transportProperties\n" << endl;

IOdictionary transportProperties
(
    IOobject
    (
        "transportProperties",
        runTime.constant(),
        mesh,
        IOobject::MUST_READ,
        IOobject::NO_WRITE
    )
);

```

```

    )
);

Info<< "Reading kinematic viscosity nu\n" << endl;
dimensionedScalar nu
(
    transportProperties.lookup("nu")
);

Info<< "Reading diffusivity D\n" << endl;
dimensionedScalar D
(
    transportProperties.lookup("D")
);

Info<< "Reading SGS Sc-number\n" << endl;
dimensionedScalar ScSgs
(
    transportProperties.lookup("ScSgs")
);

word logPatch;
transportProperties.lookup("logPatch") >> logPatch;
Info << "Will now log the following patch: " << logPatch << endl;

Info<< "Reading calculateU\n" << endl;
bool calculateU;
transportProperties.lookup("calculateU") >> calculateU;
Info << "calculateU: " << calculateU << endl;

Info<< "Reading field p\n" << endl;
volScalarField p
(
    IOobject
    (
        "p",
        runtime.timeName(),
        mesh,
        IOobject::MUST_READ,
        IOobject::AUTO_WRITE
    ),
    mesh
);

Info<< "Reading field U\n" << endl;
volVectorField U
(
    IOobject
    (
        "U",
        runtime.timeName(),
        mesh,
        IOobject::MUST_READ,
        IOobject::AUTO_WRITE
    ),

```

```

        mesh
    );

    Info<< "Reading field Y\n" << endl;
    volScalarField Y
    (
        IOobject
        (
            "Y",
            runTime.timeName(),
            mesh,
            IOobject::MUST_READ,
            IOobject::AUTO_WRITE
        ),
        mesh
    );

#   include "createPhi.H"

    Info<< "Reading field phiY\n" << endl;
    surfaceScalarField phiY
    (
        IOobject
        (
            "phiY",
            runTime.timeName(),
            mesh,
            IOobject::READ_IF_PRESENT,
            IOobject::AUTO_WRITE
        ),
        linearInterpolate(Y) * phi
    );

    label pRefCell = 0;
    scalar pRefValue = 0.0;
    setRefCell(p, mesh.solutionDict().subDict("PISO"), pRefCell,
    pRefValue);

    singlePhaseTransportModel laminarTransport(U, phi);

    autoPtr<incompressible::LESModel> sgsModel
    (
        incompressible::LESModel::New(U, phi, laminarTransport)
    );

// Read turbulent properties if there is no calculation of the flow field
    Info<< "ATTENTION: No LES flow simulation - Will calculate nuSGS from
k and epsilon\n" << endl;
    Info<< "Reading Cmu\n" << endl;
    dimensionedScalar Cmu
    (
        transportProperties.lookup("Cmu")
    );

    Info<< "Reading field kMean to calculate nuTurb\n" << endl;
    volScalarField kMean
    (
        IOobject

```

```

(
    "kMean",
    runTime.timeName(),
    mesh,
    IOobject::READ_IF_PRESENT,
    IOobject::NO_WRITE
),
mesh
);
Info<< "Reading field epsilonMean to calculate nuTurb\n" << endl;
volScalarField epsilonMean
(
    IOobject
    (
        "epsilonMean",
        runTime.timeName(),
        mesh,
        IOobject::READ_IF_PRESENT,
        IOobject::NO_WRITE
    ),
    mesh
);

```

### 9.5.4. startFluxLogger

```

Info << "Opening logFluxLogger to save instantaneous mean Sh-number and
mean concentration" << endl;

OFstream logFluxLogger
(
    runTime.path()/("logFluxLogger_" + runTime.timeName() + ".dat")
);

logFluxLogger << "Patch: " << logPatch << endl;
logFluxLogger << "time" << tab << "diffusionFlux" << tab << "totalFlux"
<< tab << tab << "C_PatchMean" << tab << "C_mean" << endl;

```

### 9.5.5. YEqn.

```

// Solve the Species Transport Equations
{
    //for(label i=0; i<Y.size(); i++)
    //{
        Info << "Solving Transport Eqn. for 1 Component " << endl;

//
        volScalarField Deff;
        volScalarField Deff = D + sgsModel->nuSgs()/ScSgs;

        if(!calculateU)
        {
            Info << "ATTENTION: No flow calculation" << endl;
            Deff = D + Cmu * kMean * kMean / epsilonMean / ScSgs; //Calculate
            sgs viscosity from k and epsilon if flow is not calculated

```

## Appendix

---

```
    }
//      Info << "Deff.max(): " << max(Deff) << tab << "Deff.min(): " <<
min(Deff) << endl;

    solve
    (
        fvm::ddt(Y)           //Time derivative
        + fvm::div(phi, Y)    //Convection Term

        ==

        fvm::laplacian(Deff, Y), //Diffusion term

        mesh.solver("Y")
    );
    Y.max(0.0); //Bound the concentration
    phiY = linearInterpolate(Y) * phi; //correct the molar fluxes in
each face
    Deff.clear();
    //}
}
```